Inelastic electron transport in nanosystems

Thomas Frederiksen
M.Sc. Thesis
February 2004

Department of Micro and Nanotechnology
Technical University of Denmark

Inelastic Electron Transport in Nanosystems
M.Sc. Thesis, Technical University of Denmark

Thomas Frederiksen
MIC – Department of Micro and Nanotechnology
Ørsteds Plads
DTU – Building 345 east
DK-2800 Kgs. Lyngby
Denmark
E-mail: `thf@mic.dtu.dk`
Web: `http://www.mic.dtu.dk`

Document typeset in $\LaTeX\,2_\varepsilon$

Abstract

The emerging field of molecular electronics, in which individual molecules play the role of active devices, is receiving much attention due to its possible technological impact. Recent advances in nanoscale fabrication and engineering techniques have made it possible to study the transport properties of devices on the atomic scale. At this level one inherently probes the quantum mechanical nature of matter which manifests a number of effects not well understood yet. One such effect is the mutual interaction between electrical current and atomic vibrations.

In this thesis we describe a method for calculating dc current-voltage characteristics of nanostructures connected between metallic leads taking into account electron-vibration scattering inside the device. The method is based on nonequilibrium Green's functions (NEGF) and a Meir-Wingreen type formula for the current through an interacting region of space. Within the Born-Oppenheimer approximation we calculate the electronic Green's functions for this region treating the electron-phonon interaction perturbatively in the self-consistent Born approximation. The numerical implementation of the present method is discussed in detail, and we compare it with results in the literature as well as with our own calculations based on an exact diagonalization technique.

In particular we look at transport through metallic wires of single atoms. With a simple single-orbital tight-binding model and parameters fitted for Au chains we show how to determine the normal modes of vibration, the electron-vibration couplings, and the influence of the different modes on the conductance. Finally, we discuss the potential of combining our method with *ab initio* calculations of electronic structure, vibrational modes, and couplings, and present some preliminary results in this direction.

Preface

The present thesis is submitted in candidacy for the Master of Science degree within the Applied Physics program at the Technical University of Denmark. The report describes parts of my work carried out from March 2003 to February 2004 under the supervision of Mads Brandbyge and Antti-Pekka Jauho from MIC, Department of Micro and Nanotechnology, Technical University of Denmark.

I am grateful to my supervisors for their enthusiastic commitments to this project and for both continuously support and constructive criticism. It has been inspiring to be a part of the Theoretical Nanotechnology Group at MIC and I have benefitted from many interactions here. In particular I thank Tomáš Novotný for tips on computing Hilbert transforms and Dan Bohr for inspiration on matrix representation of second quantization operators.

During my thesis work I had the opportunity to follow Mads Brandbyge on a 5-week visit to Laboratoire Collisions, Agrégats, Réactivité, IRSAMC, at Université Paul Sabatier, Toulouse, France. Our stay was kindly hosted by Nicolas Lorente and sponsored by the French Embassy in Denmark. This intensive period brought many advances due to innumerable stimulating discussions between the three of us. It is my pleasure to thank Nicolas Lorente for taking an extraordinary interest in this project.

The intended level of the text is aimed at fellow students with background knowledge of quantum mechanics and – in particular – equilibrium Green's function theory. Since the essential technique for this work is the slightly different nonequilibrium Green's functions I have attempted to include a rather thorough introduction. The challenge of doing so also reflects my effort to get to understand the theory.

Let me point out that I have consciously decided *not* to adopt the usual convention of taking the reduced Planck's constant $\hbar = 1$. This is because I find it instructive always to consider the units of the quantities introduced in a theory. Of course, when one really is acquainted with these it may be more convenient to adopt the atomic units.

Finally, I would like to thank all the persons close to me for understanding and patience especially during the final stage.

Thomas Frederiksen, Lyngby, February 15, 2004

Table of Contents

Chapter 1

Introduction

1.1 Towards molecular electronics

The conventional lithography based semiconductor electronics has over the last decades rapidly evolved towards increasingly smaller and faster devices. This development is characterized in Moore's Law which states that semiconductor performance doubles roughly every two years while the cost to manufacture semiconductors increases at an even greater rate. Today's microelectronic devices have a minimum feature size of about 180nm but this is in fact not very far away from fundamental limits of optical lithography, i.e. such as related to the wavelength of the light. Although the semiconductor industry sees a way for at least the next decade for making ever-smaller solid-state silicon devices by introducing new short wavelength lithography techniques, the cost of the manufacturing systems needed to make the chips is enormous and will grow worse with each new generation [1].

The continuous demand for increasingly better performing chips challenge the existing paradigm. Just as the transistor replaced the vacuum tube during the 1950s, and as integrated circuits superseded individual transistors during the 1960s, one promising candidate to take the place of the semiconductor technology is the so-called *molecular electronics* in which individual molecules play the role of the active devices. The obvious advantage is the possibility of ultradense electronics since individual molecules are hundreds of times smaller than the smallest features conceivably attainable by semiconductor technology. Where optical lithography based circuits are fundamentally limited to designs on the submicron level, single molecules may take us even as far as to the nanometer scale. Such chips could be extremely more powerful than today's state-of-the-art. Moreover, individual molecules are easily made exactly the same in incomprehensibly huge numbers $\sim 10^{23}$ in the chemist's laboratory. The dramatic reduction in size and the enormity of numbers in manufacture are the fundamental potentials of molecular electronics.

Molecular electronics was effectively founded by Aviram and Ratner [2] in 1974 when they suggested a molecular structure that could act as a diode, and further described the theory that explained why this was reasonable.

But at that time with the given experimental techniques available it was not possible to realize – those still had to reach the atomic scale.

It was not until the 1990s where the first measurements on single molecules were performed, that the field of molecular electronics received much attention. In 1997 Reed *et al.* [3] succeeded to measure the conductance of a molecular junction of gold-sulphur-aryl-sulphur-gold at room temperature using a mechanically controllable break junction (MCBJ), and they argued that the number of active molecules in the junction might have been as few as one. This demonstration towards single molecule measurements was for sure an important achievement, but without knowledge of the actual microscopic configuration the level of interpretation was rather limited.

Today a number of novel nanoscale devices and circuits based on the intricate effects of quantum mechanics have been proposed, including resonant tunneling diodes and transistors, quantum dot and single electron devices, devices displaying negative differential resistance (NDR), atomic switches, logic and memory circuits [4]. Some of these have also been experimentally demonstrated, e.g. [5, 6, 7]. But still many issues have to be resolved if real applications are to be built, for instance the organization and interconnection of individual molecules, room temperature functionality, and long-term stability.

The challenges associated with building electronics using molecules will not be overcome without a detailed understanding of the individual components. At the present moment this bottom-up approach is therefore focus for a broad range of scientists around the world. Besides the perspectives of the field it is also stimulating in itself because the discoveries on the molecular level raise many fundamental physical questions as well.

The interest and reported results within the field are too vast and comprehensive to give a complete account of here. For instance, the electrical properties of carbon nanotubes – which could be considered as extremely long molecules – have been extensively studied during the last decade. Below I will limit myself to mention a number of experiments related to *inelastic effects* on the molecular level which is the topic of this thesis, i.e. to the situation where the interplay between electrical current and the vibrational excitations of the atomic nuclei has been found to be essential part of the understanding of the observations.

The construction and operation of molecular devices will certainly rely upon control of inelastic effects. As the current flows through such devices energy of the charge carriers may be transferred into the atoms that form the microscopic structures, or vice versa. This effect is of course always present when a current flows but it is of particular relevance for such minute systems as molecular devices. The consequences of inelastic effects are many: Most important of all is probably that they affect the stability of devices since the energy transfer results in mechanical motion of the atoms which ultimately leads to malfunction or breakdown. On the other hand one can also think of exploiting the influence in a controlled manner to provide certain device properties. Inelastic effects may also be utilized in the formation and build-

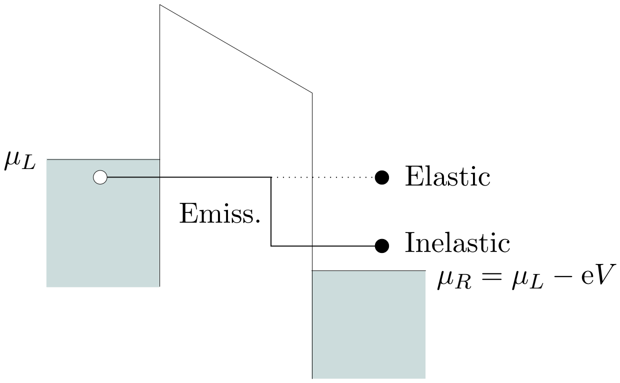

Figure 1.1: *Simple picture of elastic and inelastic tunneling processes.*

ing of circuits by moving around molecules by yielding controlled amounts of energy to them [8, 9]. One of the main objectives of the present thesis is the study of inelastic effects in electron transport through nanosystems, e.g. single molecules and atoms.

A simple picture of elastic and inelastic transport is shown in Fig. 1.1 where scattering of electrons is considered to take place inside a tunneling barrier across which a voltage V is applied. As indicated, the elastic electron tunneling involves transfer of an electron from filled states on one side of the barrier to adjacent empty states on the other. The incoming electron is accelerated in the electric field and potential energy is thus turned into kinetic energy of the particle. The energy between initial and final states balances, even though the electron may have scattered elastically against static defects and impurities or against other electrons in between. This is in contrast to inelastic tunneling where electrons lose (gain) energy by emission (absorption) of vibrational quanta – i.e. phonons – during the transfer by scattering against lattice vibrations. The inelastic tunneling process is shown on the figure as well where the finite energy drop between initial and final state of the electron indicate that energy has been transferred *to* the lattice [10].

The picture given is valid as long as it is reasonable to think in terms of noninteracting (quasi-)particles. But in fact the electron-phonon interaction indirectly causes a particle-particle interaction, for example because one electron can absorb phonons previously emitted by another electron. This is sometimes denoted the Frölich interaction [11]. For sufficiently strong electron-phonon interaction the problem is a true many-particle one in which one cannot conceptually separate elastic and inelastic processes.

1.2 Conductance of single molecules

The main experimental difficulty of measuring the transport properties of single molecules is to establish the situation where one for sure has only one molecule bridging the contacts in a two-terminal configuration. Since the late 1990s a number of different techniques have been demonstrated.

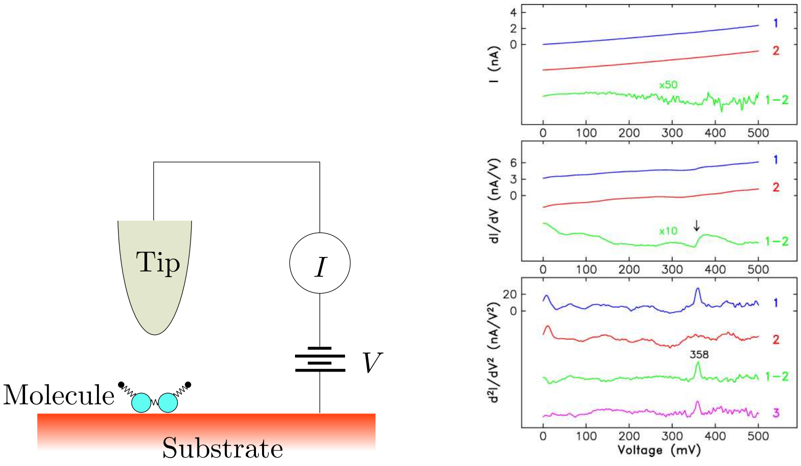

Figure 1.2: *Conductance measurement with STM. The current and its higher derivatives are recorded while sweeping the bias voltage for (1) tip over molecule and (2) tip over bare substrate. The relevant signal is the background subtracted difference (1-2). Data are shown for an acetylene molecule C_2H_2 (adapted from [12]). The minute conductance increase around 358mV indicates the opening of an inelastic channel.*

1.2.1 Scanning tunneling microscope

One way to probe the conducting properties is to use a scanning tunneling microscope (STM) which can create images of surfaces with atomic resolution utilizing tunneling currents. By positioning the STM tip over an adsorbed molecule on a conducting surface one can directly measure various properties of the molecule by sweeping the bias voltage, e.g. the local density of states. The standard setup is illustrated in Fig. 1.2. Measuring detailed conductance spectra with the STM requires extreme mechanical stability because even the slightest variations of the tunneling gap change the current exponentially. For example, a stability of 0.01Å is required to keep the conductance stable to within 2% [12].

The first theory of the STM was presented in 1983 by Tersoff and Hamann [13] only a few years after the invention was made and applies to the purely elastic tunneling processes. But it was soon realized that the STM in principle could be combined with vibrational spectroscopy methods to extract detailed information about the molecule by revealing its active vibrational modes and corresponding energies in the conductance spectrum [10].

A theory of inelastic electron tunneling spectroscopy with the STM (IETS-STM) was given in 1987 by Persson and Baratoff [14] where the elastic and inelastic tunneling rates were estimated by second order perturbation theory and Fermi's Golden rule. They predicted that under suitable conditions resonant tunneling via molecular vibration interaction can give a relative decrease of 10% in conductance. They further argued that the resonant process is dominant and that the modulation of the tunneling amplitude caused by the vibration is typically negligible.

It was not before 1998 that IETS-STM was successfully demonstrated for the first time. The achievement as due to Stripe, Rezaei, and Ho [12]. With their STM they studied an isolated acetylene C_2H_2 molecule adsorbed on a copper (100) surface. They found the signature of a single vibrational excitation by the tunneling electrons, and measured a conductance increase of the order of several percent at the threshold voltage corresponding to the C–H stretch mode. Their measurements are shown in Fig. 1.2. Today a number of different molecules have been studied by IETS-STM and both increases and decreases in conductance have been observed [8, 15].

Lorente and Persson [16] modelled the original experiment of acetylene on copper using density functional theory and a many-body generalization of the Tersoff-Hamann theory. They calculated the configuration of the molecule on the surface and the different molecular vibrational modes and corresponding contributions to the conductance. It was found that only the C–H stretch mode had important threshold signal in accordance with the experiment. Their analysis further suggested that the contribution was dominated by a vibration enhanced tunneling amplitude, i.e. nonresonant, a contrary conclusion to that of Persson and Baratoff.

Even though conductance experiments on single molecules through tunneling gaps yield valuable information as in the IETS-STM, it is also desirable to study the situation in which a molecule is directly connected to two terminals. It could in principle be done with the STM simply by moving the tip down to make contact. This should also allow for studying effects of exerting forces on the molecule during measurement. Except for the use of STM to form atomic wires (see Sec. 1.3) relatively few researchers have reported on such direct contact [17].

1.2.2 Break junctions

Single molecules may also be contacted with the use of mechanically controllable break junctions (MCBJ) or break junctions formed by electromigration (BJE). In the first method an adjustable tunneling gab is formed by breaking a conducting layer on a flexible substrate in two [18, 19]. In the latter method the gab is formed by applying a large voltage over the terminals – thereby initiating a burn off – until only a tunneling current is monitored [20].

In 2000 Park *et al.* [21] measured the transport via a single C_{60}-molecule by a BJE technique at cryogenic temperatures. A current-voltage (I–V) curve from their paper is shown in Fig. 1.3. The general pattern observed here is understood within a Coulomb blockade model for quantum dot transport, where the conductance gab is a consequence of the finite energy associated with either adding or removing one electron on C_{60}. The fine structures reveal information about a quantized excitation with an energy of approximately 5meV, which in turn provide evidence for a coupling between the

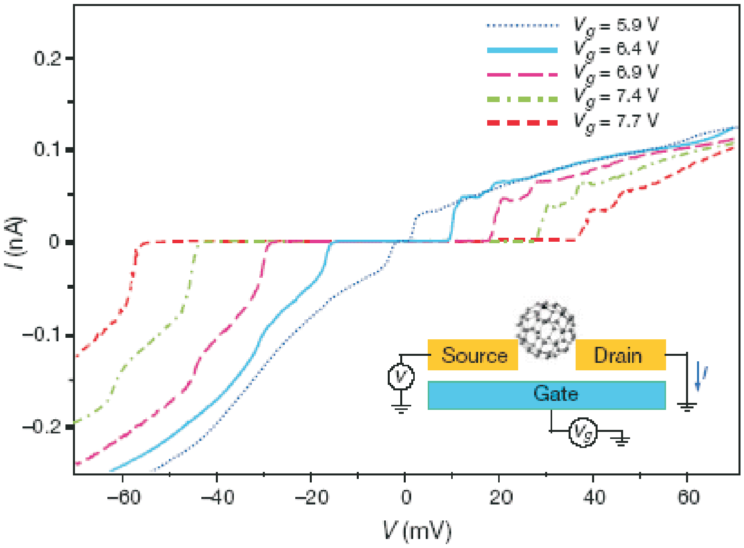

Figure 1.3: *I–V characteristic of the C_{60}-molecule (adapted from [21]). The device is clearly acting as a transistor where the gate voltage controls the current between source and drain. The series of steps in the current are known as Frank-Condon steps caused by vibrational excitations.*

center-of-mass motion of the fullerene and the transfer of single electrons.

Braig and Flensberg [22] have proposed a detailed theory applicable to this experiment. Their model consists of a single molecular orbital weakly coupled to the electrodes and strongly coupled to a dissipative vibrational mode. Using a rate equation approach in the strict Coulomb blockade regime to calculate the tunneling current, they studied how the Frank-Condon steps in the I–V curves are affected by various models for frictional damping of the oscillator. In particular they found rough qualitative agreement with the experiment using a model for dissipative coupling to the substrate.

The strong correlation between electron transfer and oscillator motion in Park *et al.*'s experiment has also been considered a possible realization of shuttling transport in which an integer number of electrons are transferred per center-of-mass oscillation. However, it seems to be an unresolved issue whether or not a true shuttling regime exists for the C_{60} in this setup, see e.g. [23].

In 2002 Smit *et al.* [24, 25] measured the conductance of a hydrogen molecule using a MCBJ with Pt contacts at cryogenic temperatures. Only with a small quantity of hydrogen gas in the vacuum chamber they found a frequently occurring stable configuration with a conductance very close to the quantum unit $G_0 = 2e^2/h \approx 1/12.9\text{k}\Omega$. The differential conductance observed for this configuration is shown in Fig. 1.4 and exhibits a single dominant resonance around 63.5mV that was interpreted as an excitation of the center-of-mass motion of the H_2-molecule.

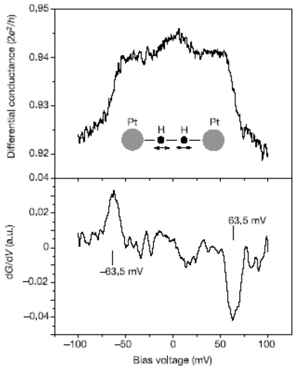

Figure 1.4: *Conductance measurement of the hydrogen molecule between platinum contacts adapted from [24]. The symmetric decrease seen around* $63.5mV$ *was interpreted as related to excitation of the center-of-mass motion of the* H_2*-molecule shown in the inset.*

1.3 Atomic wires

Electronic transport on the nanoscale does not only concern single molecules. The experimental success of fabricating metallic atomic chains with several atoms using STMs makes these systems another category of importance [26, 27, 28, 29]. The zero-bias conductance of an ideal single-mode ballistic wire is the conductance quantum G_0 as explained within the Landauer-Büttiker framework [30, 31, 32]. Because there is no intrinsic resistance in such an ideal wire the transport of electrons is ballistic and the current is solely determined by contact resistance in the leads. When only elastic scattering processes are present the Landauer-Büttiker theory provides an adequate description of the problem and the conductance is related to single-particle transmission and reflection probabilities.

In 2002 Agraït *et al.* [28] published transport measurements of atomic gold chains – freely suspended between an Au substrate and an Au STM tip – of up to seven atoms at low temperatures and finite voltages. Their measurements on a short and a long wire are shown in Fig. 1.5. The zero-bias conductance was found to be close to the quantum unit which indicate that gold wires have a single almost completely open quantum channel. This is in accordance with theoretical predictions [33, 34]. For a finite but small bias of $\sim$ 10mV a significant conductance drop of around 1% was observed and interpreted as electronic backscattering by phonon emission.

In 2003 Montgomery *et al.* [36] developed a tight-binding model of atomic wires. By investigating a chain consisting of nine atoms they found two dominant modes which lead to conductance drops, in contrast to the single drop observed in the experiment. While the one mode reproduced the experimental features it was not resolved whether the calculated influence of the second mode really is physical.

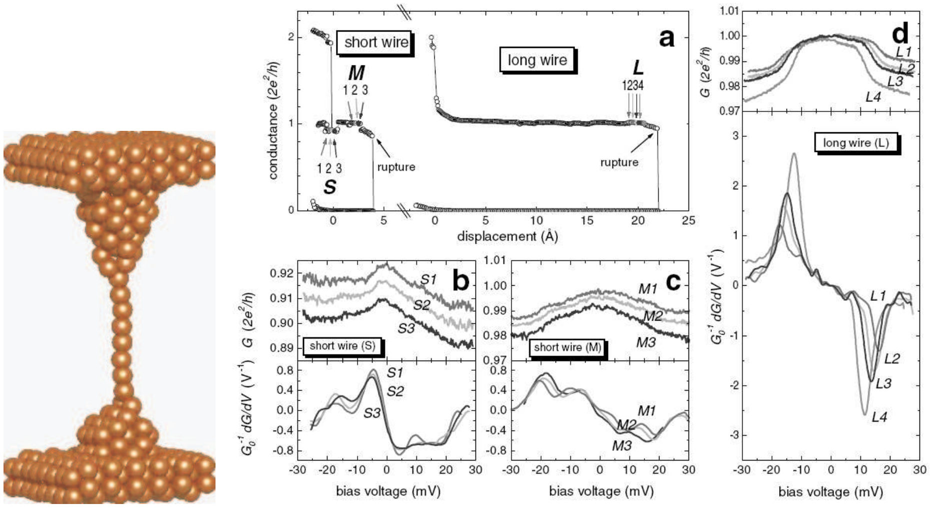

Figure 1.5: *Molecular dynamics simulation of an atomic wire adapted from [35] (left) and conductance measurements on atomic gold wires from [28] (right). In (**d**) the conductance is shown for a wire of presumably seven atoms under different strains. It is close to the conductance quantum for zero bias, but drops by 1-2% around 100-150mV. This decrease was interpreted as inelastic backscattering of electrons.*

1.4 Inelastic transport

The previous sections discussed a number of recent transport experiments on various nanoscale systems. It was found that electron-vibration interaction played an essential part for understanding the properties of the systems scrutinized.

In order to build a transport theory that include these effects it is necessary to go beyond the Landauer-Büttiker formalism where one thinks in terms of single-particle transmission probabilities. One possible approach is to describe the electron dynamics by Boltzmann kinetics via a classical distribution function $f(\mathbf{r},\mathbf{p},t)$ of the particles and express how the dynamics of a single particle is influenced by the others via collisions in the degenerate quantum gas [37]. But within such a scheme one is limited to a semiclassical description which is not sufficient for atomic-sized systems.

Another approach for a true quantum mechanical description is the Kubo formalism – also known as linear response theory – in which one extracts information about electron transport by solving the equilibrium problem by standard many-particle theory [11, 38, 39, 40]. Since the method is limited to the linear regime it cannot be used to model the highly nonlinear device characteristics usually observed.

Instead a complete quantum kinetic description of electron transport under any bias condition can be constructed by the use of *nonequilibrium Green's functions* (NEGF) [37, 41]. This method has proven to be very successful for a wide range of systems and the generality makes it a strong formal technique. For these reasons it has also been chosen as the framework for the present work.

Historically various transport equations for electrons interacting with phonons were derived by use of nonequilibrium theory in the early 1960s. Two different (but equivalent) general formulations emerged due to Keldysh [42] and Kadanoff-Baym [43] and found use within studies of normal metals. The first application of NEGF to inelastic tunneling goes back to the seminal papers in 1971 by Caroli *et al.* [44, 45, 46] on tunneling metal-insulator-metal (MIM) junctions. In the late 1980s and early 1990s double barrier resonant-tunneling structures with electron-phonon interaction were intensively studied by similar techniques by a group around Wilkins [47, 48, 49, 50, 51, 52]. And recently there has been quite a few studies of phonon effects in single electron transistors also (partly) relying on NEGF techniques, e.g. [53, 54, 55, 56].

1.5 Motivation and outline of the thesis

In context of molecular electronics it is a general theoretical challenge to predict the detailed properties of a particular device. Numerous questions arise: What is the nature of the conduction, e.g. which electronic channels contribute and which does not? How is the device influenced by the current flow and what kind of phenomena may be triggered? How to design specific operational features of a molecular device? These and many other questions are still wide open and challenging. Here the focus is on the inelastic effects on electronic conduction.

Most theoretical work based on NEGF have focused on transport via a *single* or a *few* molecular levels in presence of electron-vibration interaction. One of the challenges in the present project has been to construct a general method that can be combined with existing *ab initio* electronic structure calculations where such a limitation is not appropriate. Today various transport codes based on density functional theory exist. For instance the computational package named TRANSIESTA has successfully been applied to a range of systems including single atom carbon wires connected to aluminum electrodes, single atom gold wires connected to gold electrodes, and large carbon nanotube systems with point defects [33]. This code is limited to purely elastic transport partly because the problem is much simpler to treat within the single-particle approximation. It is of course a long sought goal to extend these kind of tools to include inelastic effects.

A scope for the present project has been to develop a numerical routine with the following features

- implementation of NEGF for modelling of electron-vibration interaction effects in nanosystems,
- describe electrons in a self-consistent manner,
- handle energy-dependent coupling to "real" leads,

- allow for finite temperatures,
- allow many electronic levels in the device,
- methods not restricted to one-dimensional models,
- compatible with *ab initio* calculations of electronic structure, vibrational modes, and electron-vibration couplings,

but subject to the following limitations

- vibrations modelled within the harmonic approximation,
- electron-phonon interaction treated to lowest order in the self-energy functional,
- devices not dominated by effects such as Coulomb blockade or Kondo resonance.

The present thesis is organized as follows. This chapter provided an introduction to the field of molecular electronics and we discussed a number of recent experiments on transport through single molecules in which inelastic effects were observed. In Chap. 2 the reader is introduced to the NEGF theory and to the development of a diagrammatic perturbation theory for the electron-vibration interaction. Chap. 3 concerns the application of NEGF to electron transport in nanosystems. In particular we derive an expression for the current originally obtained by Meir and Wingreen [57].

The theoretical framework presented in Chap. 2 and 3 has been implemented in a numerical routine described in Chap. 4. In Chap. 5 this is compared with some results in the literature on resonant tunneling through a single electronic state. One of the key features of our method is its capability of handling electron-phonon interaction in a region described by many electronic states. In order to test it in situations with more than a single state we compare with an exact diagonalization method for a 3-level system in Chap. 6.

In Chap. 7 we develop a theory for inelastic transport in atomic wires based on a single-orbital tight-binding model. The chapter expounds on the various steps involved for a complete I–V calculation in terms of simple models. At the same time it illustrates the potential of the developed method when combined with detailed *ab initio* calculations. Some preliminary results in this direction are discussed in Chap. 8. Finally, we provide a summary of the thesis and an outlook for future work.

Chapter 2

Nonequilibrium Green's function theory

2.1 Introduction

In condensed matter physics one is typically concerned about calculating physical observables from a microscopic description of the system under consideration. Such microscopic models are usually defined by writing the system Hamiltonian operator $\mathscr{H}$. Together with an appropriate number of boundary conditions the basic problem is the solution of the many-particle Schödinger's equation

$$i\hbar\frac{\partial}{\partial t}\Psi(\mathbf{r}_1,\mathbf{r}_2,\ldots,\mathbf{r}_N,t)=\mathscr{H}\Psi(\mathbf{r}_1,\mathbf{r}_2,\ldots,\mathbf{r}_N,t), \tag{2.1}$$

where $\Psi(\mathbf{r}_1,\mathbf{r}_2,\ldots,\mathbf{r}_N,t)$ is the many-particle wave function that in principle contains all relevant information about the system. Of course solving this wave equation may be difficult, if possible at all. In many-particle problems the systems are usually described by Hamiltonians which can not be solved exactly, and one has to rely on perturbative methods. In these situations the introduction of second quantization operators and Green's functions prove to be very important techniques.

Various formulations of many-particle Green's function theory exist. For instance, in equilibrium theory there is both a zero-temperature as well as a finite-temperature (Matsubara) formalism [38, 39, 40, 58]. Here I will focus on the formulation of the more general nonequilibrium finite-temperature theory which also applies to equilibrium as a special case. The chapter is intended as an introduction to the nonequilibrium Green's function (NEGF) formalism assuming that the reader is familiar with the concepts of equilibrium theory. The exposition is primarily based upon the work by Haug and Jauho [37], Jauho [59, 60], Rammer and Smith [41], and Rammer [61].

2.2 Ensemble averages in nonequilibrium

In order to formulate the nonequilibrium problem let us consider a physical system represented by a time-independent Hamiltonian

$$H = H_0 + H^i, \tag{2.2}$$

where H_0 is the non-interacting (quadratic) Hamiltonian – which acting alone is a soluble problem – and H^i the Hamiltonian describing the complicated interactions among the particles.

We will in general consider the system to be open, i.e. that it is in contact with a heat bath of temperature T and a particle reservoir characterized by the chemical potential μ. We thus work in the grand canonical ensemble. In thermodynamic equilibrium the state of system is described by the equilibrium density matrix

$$\rho(H) \;=\; \frac{e^{-\beta H}}{\mathrm{Tr}[e^{-\beta H}]} = \mathscr{Z}^{-1} e^{-\beta H}, \qquad \beta \equiv (k_B T)^{-1}, \tag{2.3}$$

where we thus have chosen to measure particle energies with respect to $\mu = 0$. Otherwise one would need to work with the number operator explicitly in the density matrix.

The nonequilibrium problem will now be defined as the following: We assume that the system is in thermodynamic equilibrium until a time t_0 where the system is instantaneously disconnected from the reservoirs and at the same time exposed to a disturbance represented by a contribution to the Hamiltonian $H'(t)$. The total time-dependent Hamiltonian $\mathscr{H}$ is now given by

$$\mathscr{H}(t) \;=\; H + H'(t), \tag{2.4a}$$

$$H'(t) \;=\; 0, \quad t < t_0. \tag{2.4b}$$

The disturbance could for instance be a time varying electric field, a light excitation pulse, or a coupling between subsystems with different chemical potential.

Having defined the nonequilibrium state, a typical task is now to calculate nonequilibrium statistical averages of operators corresponding to physical observables. In the Heisenberg picture – which describes the situation where all time dependence is transferred to the operators leaving the state vectors time-independent – this average is defined with respect to a distribution according to $\rho(H)$ as of Eq. (2.3)

$$\langle O_{\mathscr{H}}(t)\rangle \;\equiv\; \mathrm{Tr}[\rho(H) O_{\mathscr{H}}(t)], \tag{2.5}$$

where $O_{\mathscr{H}}(t)$ is the observable in the Heisenberg picture. It is a subtle point that it is not the total Hamiltonian $\mathscr{H}(t)$ that should be included in the density matrix at this point. But, as discussed by Mahan [40] p. 214-216, a straight forward inclusion of $H'(t)$ in ρ leads to incorrect results.

In the description of the nonequilibrium problem it is useful to work with various quantum mechanical pictures. By suitable transformations between these one can then find more practical expressions for the averaging. This is discussed the present section. We set out by establishing the relation between operators in the Heisenberg and Schrödinger pictures by considering Schrödinger's equation,

$$i\hbar\partial_t|\Psi_S(t)\rangle = \mathscr{H}(t)|\Psi_S(t)\rangle, \tag{2.6}$$

where the ket $|\Psi_S(t)\rangle$ is the abstract state vector. Eq. (2.6) can formally be integrated to

$$|\Psi_S(t)\rangle - |\Psi_S(t_0)\rangle = -i\hbar^{-1}\int_{t_0}^{t}\mathrm{d}t_1\mathscr{H}(t_1)|\Psi_S(t_1)\rangle, \tag{2.7}$$

which iterates to

$$\begin{aligned}|\Psi_S(t)\rangle &= \sum_{n=0}^{\infty}\frac{(-i\hbar^{-1})^n}{n!}\int_{t_0}^{t}\mathrm{d}t_1\int_{t_0}^{t_1}\mathrm{d}t_2\cdots\int_{t_0}^{t_{n-1}}\mathrm{d}t_n \\ &\qquad\qquad\times\mathscr{H}(t_1)\mathscr{H}(t_2)\cdots\mathscr{H}(t_n)|\Psi_S(t_0)\rangle \qquad (2.8)\\ &= \sum_{n=0}^{\infty}\frac{(-i\hbar^{-1})^n}{n!}\int_{t_0}^{t}\mathrm{d}t_1\cdots\int_{t_0}^{t}\mathrm{d}t_n T_t\{\mathscr{H}(t_1)\cdots\mathscr{H}(t_n)\}|\Psi_S(t_0)\rangle.\end{aligned}$$

Here T_t is the usual time-ordering operator that organizes a product of operators according to their time arguments ("later to the left"),

$$\begin{gathered}T_t\{A_1(t_1)A_2(t_2)\cdots A_n(t_n)\} = (-1)^P A_{i_1}(t_{i_1})A_{i_2}(t_{i_2})\cdots A_{i_n}(t_{i_n}), \qquad (2.9)\\ t_{i_1} > t_{i_2} > \cdots > t_{i_n},\end{gathered}$$

where P is the number of interchanges of fermion operators from the original given order [39, 61]. For a Hamiltonian containing an even number of fermion fields this sign is always positive.

From Eq. (2.8) we identify the evolution operator with respect to $\mathscr{H}$

$$\begin{aligned}u_{\mathscr{H}}(t,t_0) &= \sum_{n=0}^{\infty}\frac{(-i\hbar^{-1})^n}{n!}\int_{t_0}^{t}\mathrm{d}t_1\cdots\int_{t_0}^{t}\mathrm{d}t_n T_t\{\mathscr{H}(t_1)\cdots\mathscr{H}(t_n)\},\\ &\equiv T_t\{e^{-i\hbar^{-1}\int_{t_0}^{t}\mathrm{d}t'\mathscr{H}(t')}\}. \qquad (2.10)\end{aligned}$$

The quantum mechanical average must be the same evaluated in either the Schrödinger or in the Heisenberg picture, i.e.

$$\langle\Psi_S(t)|O_S|\Psi_S(t)\rangle = \langle\Psi_{\mathscr{H}}|O_{\mathscr{H}}(t)|\Psi_{\mathscr{H}}\rangle, \tag{2.11}$$

If we choose the pictures to coincide at time t_0 we have $|\Psi_{\mathscr{H}}\rangle = |\Psi_S(t_0)\rangle$ and $O_{\mathscr{H}}(t_0) = O_S$. This in turn leads to the following relation

$$O_{\mathscr{H}}(t) \equiv u^{\dagger}_{\mathscr{H}}(t,t_0)O_S u_{\mathscr{H}}(t,t_0). \tag{2.12}$$

This expression will be used a number of times below.

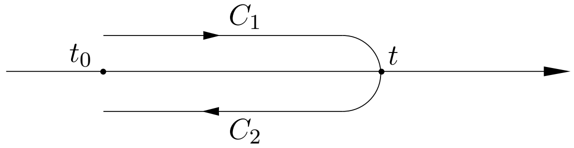

Figure 2.1: *The contour $C \equiv C_1 \cup C_2$ used in the transformation into a time evolution governed by H. The contour runs on the real axis but for clarity its two branches C_1 and C_2 are shown slightly away from it.*

2.2.1 Transformation one: Evolution with respect to H

Having expressed the operator $O_{\mathscr{H}}(t)$ in the Heisenberg picture the next question is what it looks like when the time evolution of the operators are governed by the time-independent part H. The time evolution is defined as

$$\widehat{O}_H(t) \;\equiv\; u_H^\dagger(t,t_0) O_S u_H(t,t_0), \tag{2.13}$$

where the evolution operator with respect to H is given as

$$u_H(t,t_0) \;=\; e^{-iH(t-t_0)/\hbar}. \tag{2.14}$$

Combining Eq. (2.12) and (2.13) we get

$$\begin{aligned} O_{\mathscr{H}}(t) &= u_{\mathscr{H}}^\dagger(t,t_0) u_H(t,t_0) \widehat{O}_H(t) u_H^\dagger(t,t_0) u_{\mathscr{H}}(t,t_0) \\ &= v_H^\dagger(t,t_0) \widehat{O}_H(t) v_H(t,t_0), \end{aligned} \tag{2.15}$$

where

$$v_H(t,t_0) \;\equiv\; u_H^\dagger(t,t_0) u_{\mathscr{H}}(t,t_0). \tag{2.16}$$

Differentiating $v_H(t,t_0)$ with respect to the time argument t yields

$$\begin{aligned} i\hbar\partial_t v_H(t,t_0) &= [i\hbar\partial_t u_H^\dagger(t,t_0)] u_{\mathscr{H}}(t,t_0) + u_H^\dagger(t,t_0)[i\hbar\partial_t u_{\mathscr{H}}(t,t_0)] \\ &= [-H u_H^\dagger(t,t_0)] u_{\mathscr{H}}(t,t_0) + u_H^\dagger(t,t_0)[\mathscr{H}(t) u_{\mathscr{H}}(t,t_0)] \\ &= -H v_H(t,t_0) + u_H^\dagger(t,t_0)\mathscr{H}(t) u_H(t,t_0) u_H^\dagger(t,t_0) u_{\mathscr{H}}(t,t_0) \\ &= -\widehat{H}_H(t) v_H(t,t_0) + \widehat{\mathscr{H}}_H(t) v_H(t,t_0) \\ &= \widehat{H}'_H(t) v_H(t,t_0). \end{aligned} \tag{2.17}$$

Similar to the derivation of Eq. (2.10) one finds by integration of Eq. (2.17) with the boundary condition $v_H(t_0,t_0) = 1$ and subsequent iteration that

$$v_H(t,t_0) \;=\; T_t\{e^{-i\hbar^{-1}\int_{t_0}^{t} \mathrm{d}t' \widehat{H}'_H(t')}\}. \tag{2.18}$$

We notice that the ordinary time-ordering also can be written as ordering along contour branches C_1 and C_2 of the contour C as depicted in Fig. 2.1, i.e.

$$v_H(t,t_0) \;=\; T_{C_1}\{e^{-i\hbar^{-1}\int_{C_1} \mathrm{d}\tau \widehat{H}'_H(\tau)}\} \tag{2.19a}$$

$$v_H^\dagger(t,t_0) \;=\; T_{C_2}\{e^{-i\hbar^{-1}\int_{C_2} \mathrm{d}\tau \widehat{H}'_H(\tau)}\}, \tag{2.19b}$$

where T_C is the contour-ordering operator that organizes a product of operators according to their time arguments on the contour C such that

$$\begin{aligned} T_C\{A_1(t_1)A_2(t_2)\cdots A_n(t_n)\} &= (-1)^P A_{i_1}(t_{i_1})A_{i_2}(t_{i_2})\cdots A_{i_n}(t_{i_n}),\\ &\quad t_{i_1} >_C t_{i_2} >_C \cdots >_C t_{i_n}. \end{aligned} \tag{2.20}$$

The operator combination in Eq. (2.15) thus takes the form

$$O_{\mathscr{H}}(t) \;=\; T_{C_2}\{\cdots\}\widehat{O}_H(t)T_{C_1}\{\cdots\}, \tag{2.21}$$

which is nothing but a contour-ordered product on the *combined* contour C. One can therefore write[1]

$$O_{\mathscr{H}}(t) \;=\; T_C\{e^{-i\int_C \mathrm{d}\tau \widehat{H}'_H(\tau)}\widehat{O}_H(t)\}. \tag{2.22}$$

With Eq. (2.22) at hand we have thus transformed into a situation where the nonequilibrium part $H'(t)$ appears explicitly and where the time-evolution of the operators are governed by H only.

2.2.2 Transformation two: The interaction picture

Having treated the problem when the time evolution is governed by H we now turn to the interaction picture in which the time evolution is governed by the simple part H_0. The interaction picture is defined by

$$\widehat{O}_{H_0}(t) \;=\; u^\dagger_{H_0}(t,t_0)O_S u_{H_0}(t,t_0), \tag{2.23}$$

where the evolution operator in the interaction picture is given as

$$u_{H_0}(t,t_0) \;=\; e^{-iH_0(t-t_0)/\hbar}. \tag{2.24}$$

Combining Eq. (2.12) and (2.23) we get

$$\begin{aligned} O_{\mathscr{H}}(t) &= u^\dagger_{\mathscr{H}}(t,t_0)u_{H_0}(t,t_0)\widehat{O}_{H_0}(t)u^\dagger_{H_0}(t,t_0)u_{\mathscr{H}}(t,t_0)\\ &= v^\dagger_{H_0}(t,t_0)\widehat{O}_{H_0}v_{H_0}(t,t_0), \end{aligned} \tag{2.25}$$

where

$$v_{H_0}(t,t_0) \;\equiv\; u^\dagger_{H_0}(t,t_0)u_{\mathscr{H}}(t,t_0). \tag{2.26}$$

Differentiating $v_{H_0}(t,t_0)$ with respect to the time argument t yields

$$\begin{aligned} i\hbar\partial_t v_{H_0}(t,t_0) &= [i\hbar\partial_t u^\dagger_{H_0}(t,t_0)]u_{\mathscr{H}}(t,t_0) + u^\dagger_{H_0}(t,t_0)[i\hbar\partial_t u_{\mathscr{H}}(t,t_0)]\\ &= [-H_0 u^\dagger_{H_0}(t,t_0)]u_{\mathscr{H}}(t,t_0) + u^\dagger_{H_0}(t,t_0)[\mathscr{H}(t)u_{\mathscr{H}}(t,t_0)]\\ &= -H_0 v_{H_0}(t,t_0)\\ &\qquad + u^\dagger_{H_0}(t,t_0)\mathscr{H}(t)u_{H_0}(t,t_0)u^\dagger_{H_0}(t,t_0)u_{\mathscr{H}}(t,t_0)\\ &= -H_0 v_H(t,t_0) + \widehat{\mathscr{H}}_{H_0}(t)v_{H_0}(t,t_0)\\ &= [\widehat{H}^i_{H_0}(t) + \widehat{H}'_{H_0}(t)]v_{H_0}(t,t_0). \end{aligned} \tag{2.27}$$

---

[1] A proof of the equivalence of Eq. (2.15) and (2.22) is found in [37] p. 61-62.

Similar to the derivations of Eq. (2.10) and (2.18) one finds by integration of Eq. (2.27) with the boundary condition $v_{H_0}(t_0, t_0) = 1$ and subsequent iteration that

$$\begin{aligned} v_{H_0}(t, t_0) &= T_t\{e^{-i\hbar^{-1}\int_{t_0}^{t} \mathrm{d}t' [\widehat{H}^i_{H_0}(t)+\widehat{H}'_{H_0}(t)]}\} \\ &= T_t\{e^{-i\hbar^{-1}\int_{t_0}^{t} \mathrm{d}t' \widehat{H}'_{H_0}(t)} e^{-i\hbar^{-1}\int_{t_0}^{t} \mathrm{d}t' \widehat{H}^i_{H_0}(t)}\}. \end{aligned} \tag{2.28}$$

Again, we use the contour-ordering operator T_C to write Eq. (2.25) as

$$\begin{aligned} O_{\mathscr{H}}(t) &= T_C\{e^{-i\hbar^{-1}\int_C \mathrm{d}\tau \widehat{H}'_{H_0}(\tau)} e^{-i\hbar^{-1}\int_C \mathrm{d}\tau \widehat{H}^i_{H_0}(\tau)} \widehat{O}_{H_0}(t)\} \\ &= T_C\{S'_C S^i_C \widehat{O}_{H_0}(t)\}, \end{aligned} \tag{2.29}$$

where

$$S'_C \equiv e^{-i\hbar^{-1}\int_C \mathrm{d}\tau \widehat{H}'_{H_0}(\tau)}, \tag{2.30a}$$

$$S^i_C \equiv e^{-i\hbar^{-1}\int_C \mathrm{d}\tau \widehat{H}^i_{H_0}(\tau)}. \tag{2.30b}$$

Before we can write the quantum mechanical average in the interaction picture we need to replace the ensemble average with respect to $\rho(H)$ by that of $\rho(H_0)$. One way is to consider the operator $w(t, t_0)$ defined as [61]

$$w(t, t_0) \equiv T_t\{v^\dagger_{H_0}(t, t_0) v_H(t, t_0)\}. \tag{2.31}$$

Differentiating with respect to t yields

$$\begin{aligned} i\hbar\partial_t w(t, t_0) &= -[\widehat{H}^i_{H_0}(t) + \widehat{H}'_{H_0}(t)] w_H(t, t_0) + T_t\{v^\dagger_{H_0}(t, t_0) \widehat{H}'_H(t) v_H(t, t_0)\} \\ &= -[\widehat{H}^i_{H_0}(t) + \widehat{H}'_{H_0}(t)] w_H(t, t_0) \\ &\quad + T_t\{v^\dagger_{H_0}(t, t_0) u^\dagger_H(t, t_0) u_{H_0}(t, t_0) \widehat{H}'_{H_0}(t) \\ &\qquad \times u^\dagger_{H_0}(t, t_0) u_H(t, t_0) v_H(t, t_0)\} \\ &= -\widehat{H}^i_{H_0}(t) w_{H_0}(t, t_0). \end{aligned} \tag{2.32}$$

With $w(t_0, t_0) = 1$, integration and subsequent iteration lead us to

$$w(t, t_0) = T_t\{e^{-i\int_{t_0}^{t} \mathrm{d}t' \widehat{H}^i_{H_0}(t')}\}. \tag{2.33}$$

Combining Eq. (2.16), (2.26) and (2.31) we find

$$u_H(t, t_0) = u_{H_0}(t, t_0) w(t, t_0). \tag{2.34}$$

Recalling that $u_H(t, t_0) = e^{-iH(t-t_0)/\hbar}$ and $u_{H_0}(t, t_0) = e^{-iH_0(t-t_0)/\hbar}$ we see that for $t = t_0 - i\beta$ Eq. (2.34) becomes

$$e^{\beta H} = e^{\beta H_0} w(t_0 - i\beta, t_0). \tag{2.35}$$

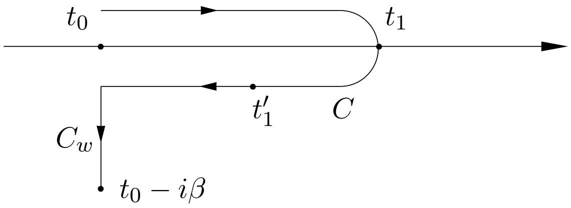

Figure 2.2: *The contour* $\widetilde{C} \equiv C \cup C_w$ *used in the transformation into the interaction picture of* H_0*.*

This relation allow us to rewrite the ensemble average Eq. (2.5) as

$$\begin{aligned} \langle O_{\mathscr{H}}(t)\rangle &= \frac{\mathrm{Tr}[e^{-\beta H} O_{\mathscr{H}}(t)]}{\mathrm{Tr}[e^{-\beta H}]} \\ &= \frac{\mathrm{Tr}[e^{-\beta H_0} w(t_0 - i\beta, t_0) O_{\mathscr{H}}(t)]}{\mathrm{Tr}[e^{-\beta H_0} w(t_0 - i\beta, t_0)]} \\ &= \frac{\langle w(t_0 - i\beta, t_0) O_{\mathscr{H}}(t)\rangle_0}{\langle w(t_0 - i\beta, t_0)\rangle_0}, \end{aligned} \tag{2.36}$$

where the average $\langle \cdots \rangle_0$ indicates the ensemble average is with respect to $\rho(H_0)$. The operator $w(t_0 - i\beta, t_0)$ is defined on a contour strip C_w from t_0 to $t_0 - i\beta$ as shown in Fig. 2.2. Using that

$$T_C\{e^{-i\hbar^{-1}\int_C \mathrm{d}\tau \widehat{H}^i_{H_0}(\tau)} e^{-i\hbar^{-1}\int_C \mathrm{d}\tau \widehat{H}'_{H_0}(\tau)}\} = 1, \tag{2.37}$$

because the contour C is closed we can write $w(t_0 - i\beta, t_0)$ as an integration along a contour $\widetilde{C}$, cf. Fig. 2.2,

$$\begin{aligned} w(t_0 - i\beta, t_0) &= T_{\widetilde{C}}\{e^{-i\hbar^{-1}\int_C \mathrm{d}\tau \widehat{H}'_{H_0}(\tau)} e^{-i\hbar^{-1}\int_{\widetilde{C}} \mathrm{d}\tau \widehat{H}^i_{H_0}(\tau)}\} \\ &= T_{\widetilde{C}}\{S'_C S^i_{\widetilde{C}}\}, \end{aligned} \tag{2.38}$$

where S'_C was introduced earlier and

$$S^i_{\widetilde{C}} = e^{-i\hbar^{-1}\int_{\widetilde{C}} \mathrm{d}\tau \widehat{H}^i_{H_0}(\tau)}. \tag{2.39}$$

Finally we write the ensemble average as

$$\langle O_{\mathscr{H}}(t)\rangle = \frac{\langle T_{\widetilde{C}}\{S'_C S^i_{\widetilde{C}} \widehat{O}_{H_0}(t)\}\rangle_0}{\langle T_{\widetilde{C}}\{S'_C S^i_{\widetilde{C}}\}\rangle_0}. \tag{2.40}$$

This form has isolated the “difficult” parts H^i and $H'(t)$ into separate factors $S^i_{\widetilde{C}}$ and S'_C, it has all time-dependence determined by the simple part H_0, and the ensemble average is to be evaluated with respect to the noninteracting density matrix $\rho(H_0)$. These features are – just as in equilibrium theory – favorable for further theoretical treatments.

One simplification occurs if we restrict ourselves to steady state problems. This means that we only study the system after the disturbance has been turned on for sufficiently long time, i.e. $t \gg t_0$. Equivalently we can take the limit $t_0 \to -\infty$. If the interactions among the particles are turned on adiabatically it is evident from Eq. (2.33) that

$$\lim_{t_0 \to -\infty} w(t_0 - i\beta, t_0) \;=\; \lim_{t_0 \to -\infty} T_{C_w}\{e^{-i\int_{t_0}^{t_0 - i\beta} \mathrm{d}t' \widehat{H}^i_{H_0}(t')}\} = 1. \qquad (2.41)$$

We thus see that in this steady state limit the contours C and $\widetilde{C}$ coincide.

2.3 Green's functions and perturbation theory

In the previous sections we restricted the discussion to the evaluation of nonequilibrium statistical averages of operators O corresponding to physical observables. Instead of calculating such operator averages directly from Eq. (2.40) one usually studies Green's functions in many-particle physics. This method is convenient because much information about the system can be extracted from the knowledge of Green's functions. In nonequilibrium theory we will in particular be working with the *contour-ordered* single-particle Green's function defined as

$$G(1,1') \;\equiv\; -i\hbar^{-1}\langle T_C\{\Psi_{\mathscr{H}}(1)\Psi^\dagger_{\mathscr{H}}(1')\}\rangle, \qquad (2.42)$$

where $\Psi_H(1)$ is the field operator in the Heisenberg picture and where the short-hand notation

$$1 \equiv (\mathbf{r}_1, \sigma_1, t_1) \qquad (2.43)$$

has been introduced. The field operators are suitable linear combinations of the creation and annihilation operators

$$\Psi(\mathbf{r},\sigma) \;\equiv\; \sum_k \psi_k(\mathbf{r}) c_{k\sigma}, \qquad (2.44a)$$

$$\Psi^\dagger(\mathbf{r},\sigma) \;\equiv\; \sum_k \psi^*_k(\mathbf{r}) c^\dagger_{k\sigma}, \qquad (2.44b)$$

where the coefficients $\psi_k(\mathbf{r})$ and $\psi^*_k(\mathbf{r})$ are the single-particle wave functions and $c_{k\sigma}$ ($c^\dagger_{k\sigma}$) the annihilation (creation) operator that raises (lowers) the occupation of particles in state $|k\sigma\rangle$. The sum is over a complete set of quantum numbers.

The nonequilibrium steady-state Green's function can now be written in the interaction picture adapting the result Eq. (2.40)

$$G(1,1') \;=\; -i\hbar^{-1}\frac{\langle T_C\{S'_C S^i_C \widehat{\Psi}_{H_0}(1)\widehat{\Psi}^\dagger_{H_0}(1')\}\rangle_0}{\langle T_C\{S'_C S^i_C\}\rangle_0}. \qquad (2.45)$$

This expression constitutes a suitable starting point for the construction of a perturbation theory since one can expand numerator and denominator and apply Wick's theorem as in equilibrium theory. A careful derivation of the theorem for ordinary time-ordering is found in the textbook by Fetter and

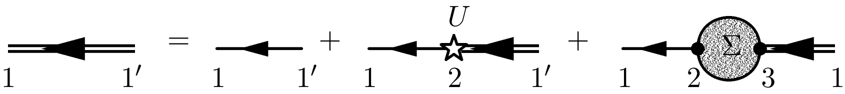

Figure 2.3: *Diagrammatic representation of Dyson's equation (2.46). The single (double) line is the unperturbed (full) electron Green's function.*

Walecka [39] p. 83-92. Since the proof holds equally well for contour-ordered operator products, we shall also rely on the theorem in nonequilibrium and establish Feynman rules and diagram representations. As in equilibrium theory the denominator exactly cancels the disconnected diagrams.

The contour-ordered single-particle Green's function $G(1,1')$ thus possesses a systematic perturbation expansion similar to the time-ordered single-particle Green's function of equilibrium theory. The only difference is that time integrations over the real axis are replaced by contour integrations along C. The contour-ordered single-particle Green's function obeys *Dyson's equation*

$$\begin{aligned} G(1,1') &= G_0(1,1') + \int_C \mathrm{d}2\; G_0(1,2)U(2)G(2,1') \\ &\quad + \int_C \mathrm{d}2 \int_C \mathrm{d}3\; G_0(1,2)\Sigma(2,3)G(3,1'), \end{aligned} \tag{2.46}$$

where G_0 is the unperturbed Green's function, U is a single-particle external potential, and $\Sigma[G]$ the (irreducible) self-energy functional. A diagrammatic representation of Dyson's equation is shown in Fig. 2.3. Again, a short-hand notation has been introduced

$$\int_C \mathrm{d}1 \equiv \sum_{\sigma_1} \int \mathrm{d}\mathbf{r}_1 \int_C \mathrm{d}\tau_1. \tag{2.47}$$

The contour integrations are mostly a formal tool since in practical calculations one replaces them by real-time integrations. The procedures for such replacements are known as the Langreth's rules.

2.3.1 Analytic continuation

It is convenient to work with the following real-time single-particle Green's functions

$$\begin{aligned} G^<(1,1') &\equiv \pm i\hbar^{-1}\langle \Psi^\dagger_{\mathscr{H}}(1')\Psi_{\mathscr{H}}(1)\rangle, && \text{(2.48a)} \\ G^>(1,1') &\equiv -i\hbar^{-1}\langle \Psi_{\mathscr{H}}(1)\Psi^\dagger_{\mathscr{H}}(1')\rangle, && \text{(2.48b)} \\ G^r(1,1') &\equiv -i\hbar^{-1}\theta(t-t')\langle [\Psi_{\mathscr{H}}(1),\Psi^\dagger_{\mathscr{H}}(1')]_\pm\rangle && \text{(2.48c)} \\ &= \theta(t-t')[G^>(1,1') - G^<(1,1')], && \\ G^a(1,1') &\equiv i\hbar^{-1}\theta(t'-t)\langle [\Psi_{\mathscr{H}}(1),\Psi^\dagger_{\mathscr{H}}(1')]_\pm\rangle && \text{(2.48d)} \\ &= -\theta(t'-t)[G^>(1,1') - G^<(1,1')], && \end{aligned}$$

known as the *retarded*, the *advanced*, the *lesser*, and the *greater* Green's functions. The upper (lower) sign applies to fermions (bosons), and the brackets $[\cdots]_\pm$ are to be interpreted as the anti-commutator (commutator) defined as

$$\begin{aligned} [A,B]_+ &= \{A,B\} \equiv AB+BA \qquad \text{(fermions)}, && (2.49a)\\ [A,B]_- &= [A,B] \equiv AB-BA \qquad \text{(bosons)}. && (2.49b) \end{aligned}$$

We notice that for particular positions of the time arguments on the contour C we can write, cf. Fig. 2.1

$$G(1,1') = \begin{cases} G^t(1,1'), & t,t' \in C_1 \\ G^<(1,1'), & t \in C_1, t' \in C_2 \\ G^>(1,1'), & t \in C_2, t' \in C_1 \\ G^{at}(1,1'), & t,t' \in C_2 \end{cases} \qquad (2.50)$$

where G^t (G^{at}) is the time-ordered (antitime-ordered) Green's function,

$$\begin{aligned} G^t(1,1') &= \theta(t-t')G^>(1,1') + \theta(t'-t)G^<(1,1') \\ &= G^<(1,1') + G^r(1,1') \\ &= G^>(1,1') + G^a(1,1'), && (2.51a)\\ G^{at}(1,1') &= \theta(t'-t)G^>(1,1') + \theta(t-t')G^<(1,1') \\ &= G^<(1,1') - G^a(1,1') \\ &= G^>(1,1') - G^r(1,1'), && (2.51b) \end{aligned}$$

From these equations we see that there are only three linearly independent Green's functions (the set is redundant) since

$$G^r(1,1') - G^a(1,1') = G^>(1,1') - G^<(1,1'). \qquad (2.52)$$

A similar relation holds for other two-time quantities on the contour, e.g. the self-energy $\Sigma(1,1')$,

$$\Sigma^r(1,1') - \Sigma^a(1,1') = \Sigma^>(1,1') - \Sigma^<(1,1'). \qquad (2.53)$$

2.3.2 Langreth's theorem

Often we encounter quantities such as

$$\int_C d\tau_1 \cdots \int_C d\tau_n A(\tau,\tau_1)B(\tau_1,\tau_2)\cdots N(\tau_n,\tau'), \qquad (2.54)$$

and want to extract the real-time parts, e.g. in a series expansion of the Green's function Eq. (2.45) or in Dyson's equation Eq. (2.46). This can be derived by successive application of Langreth's theorem for a "contour convolution." The theorem may be stated as follows: The quantity

$$C(\tau,\tau') = \int_C d\tau_1 A(\tau,\tau_1)B(\tau_1,\tau'), \qquad (2.55)$$

has the real-time components

$$\begin{aligned} C^{\lessgtr}(t,t') &= \int_{-\infty}^{\infty} \mathrm{d}t_1 [A^r(t,t_1)B^{\lessgtr}(t_1,t') + A^{\lessgtr}(t,t_1)B^a(t_1,t')], \quad (2.56\mathrm{a}) \\ C^{r(a)}(t,t') &= \int_{-\infty}^{\infty} \mathrm{d}t_1 A^{r(a)}(t,t_1)B^{r(a)}(t_1,t'). \quad (2.56\mathrm{b}) \end{aligned}$$

The proof for the lesser and greater parts Eq. (2.56a) is carried out by suitable contour deformations that separate t and t' onto the two branches of a "two-loop" contour. This is carefully shown by Haug and Jauho [37]. With Eq. (2.56a) at hand the retarded and advanced parts Eq. (2.56b) follows directly from Eq. (2.48c)-(2.48d).

Langreth's theorem is readily generalized: The quantity

$$D(\tau,\tau') = \int_C \mathrm{d}\tau_1 \int_C \mathrm{d}\tau_2 A(\tau,\tau_1)B(\tau_1,\tau_2)C(\tau_2,\tau') \quad (2.57)$$

has real-time parts

$$\begin{aligned} D^{\lessgtr}(t,t') &= \int_{-\infty}^{\infty} \mathrm{d}t_1 \left[A^r(t,t_1) \left\{ \int_C \mathrm{d}\tau_2 B(t_1,\tau_2)C(\tau_2,t') \right\}^{\lessgtr} \right. \\ &\qquad \left. + A^{\lessgtr}(t,t_1) \left\{ \int_C \mathrm{d}\tau_2 B(t_1,\tau_2)C(\tau_2,t') \right\}^{a} \right] \\ &= \int_{-\infty}^{\infty} \mathrm{d}t_1 \int_{-\infty}^{\infty} \mathrm{d}t_2 \left[A^r(t,t_1)B^r(t_1,t_2)C^{\lessgtr}(t_2,t') \right. \\ &\qquad \left. + A^r(t,t_1)B^{\lessgtr}(t_1,t_2)C^a(t_2,t') + A^{\lessgtr}(t,t_1)B^a(t_1,t_2)C^a(t_2,t') \right], \\ &\qquad (2.58\mathrm{a}) \\ D^{r(a)}(t,t') &= \int_{-\infty}^{\infty} \mathrm{d}t_1 \int_{-\infty}^{\infty} \mathrm{d}t_2 A^{r(a)}(t,t_1)B^{r(a)}(t_1,t_2)C^{r(a)}(t_2,t'). \quad (2.58\mathrm{b}) \end{aligned}$$

2.3.3 Dyson's and Keldysh's equations

Applying Langreth's theorem to the Dyson equation Eq. (2.46) we extract[2]

$$\begin{aligned} G^{r(a)}(1,1') &= G_0^{r(a)}(1,1') + \int_t \mathrm{d}2 \int_t \mathrm{d}3 \; G_0^{r(a)}(1,2)\Sigma^{r(a)}(2,3)G^{r(a)}(3,1'), \\ &\qquad (2.59\mathrm{a}) \\ G^{\lessgtr}(1,1') &= G_0^{\lessgtr}(1,1') \\ &\quad + \int_t \mathrm{d}2 \int_t \mathrm{d}3 \left[G_0^r(1,2)\Sigma^r(2,3)G^{\lessgtr}(3,1') \right. \\ &\quad \left. + G_0^r(1,2)\Sigma^{\lessgtr}(2,3)G^a(3,1') + G_0^{\lessgtr}(1,2)\Sigma^a(2,3)G^a(3,1') \right], \\ &\qquad (2.59\mathrm{b}) \end{aligned}$$

---

[2] Ignoring the one-body potential U which can be absorbed in G_0 by a suitable redefinition according to $G_0^{-1} - U \longrightarrow G_0^{-1}$, cf. Eq. (2.63)-(2.64) or Haug and Jauho [37] Chap. 5.

where

$$\int_t \mathrm{d}1 \equiv \sum_{\sigma_1} \int \mathrm{d}\mathbf{r}_1 \int_{-\infty}^{\infty} \mathrm{d}t_1. \tag{2.60}$$

Iterating Eq. (2.59b) one arrives at the integral Keldysh equation [37]

$$\begin{aligned} G^{\lessgtr}(1,1') &= \int_t \mathrm{d}2 \cdots \int_t \mathrm{d}5 \, [\delta(1-2)\delta(2-3) + G^r(1,2)\Sigma^r(2,3)] \\ &\quad \times G_0^{\lessgtr}(3,4) \left[\delta(4-5)\delta(5-1') + \Sigma^a(4,5)G^a(5,1')\right] \\ &\quad + \int_t \mathrm{d}2 \int_t \mathrm{d}3 \; G^r(1,2)\Sigma^{\lessgtr}(2,3)G^a(3,1'), \end{aligned} \tag{2.61}$$

where

$$\delta(1-2) \equiv \delta(\mathbf{r}_1 - \mathbf{r}_2)\delta(t_1 - t_2)\delta_{\sigma_1,\sigma_2}. \tag{2.62}$$

Introducing the inverse operator $\overrightarrow{G}^{-1}(1,2)$ defined as

$$\int_C \mathrm{d}2 \; \overrightarrow{G}^{-1}(1,2)G(2,1') = \delta(1-1'), \tag{2.63}$$

where the arrow indicate which way the operator acts, and using the noninteracting properties [61]

$$\overrightarrow{G}_0^{-1}(1,1') = \overrightarrow{G}_0^{-1}(1)\delta(1-1'), \tag{2.64}$$

$$\overrightarrow{G}_0^{-1}(1) = i\hbar\partial_{t_1} - H_0, \tag{2.65}$$

we write Eq. (2.61) as

$$\begin{aligned} G^{\lessgtr}(1,1') &= \int_t \mathrm{d}2 \int_t \mathrm{d}3 \; G^r(1,2)[\overleftarrow{G}_0^{-1}(2)G_0^{\lessgtr}(2,3)\overrightarrow{G}_0^{-1}(3) \\ &\qquad + \Sigma^{\lessgtr}(2,3)]G^a(3,1'), \end{aligned} \tag{2.66}$$

By reversing the first operator we see that $\overrightarrow{G}_0^{-1}(2)G_0^{\lessgtr}(2,3) = 0$ because the field operator $\Psi_{H_0}(2)$ (in the interaction picture) entering the unperturbed Green's functions obeys the equation of motion $i\hbar\partial_{t_2}\Psi_{H_0}(2) = H_0\Psi_{H_0}(2)$. The first term in Eq. (2.66) therefore vanishes except for any boundary terms introduced by the reversal of the operator. As pointed out by Davies *et al.* [51] the boundary term in time contains the memory of the initial state, before the interactions and nonequilibrium dynamics were turned on. Usually it is assumed that these initial effects are damped when one looks at the steady state. In this thesis we thus often work with the steady state Keldysh equations

$$G^{\lessgtr}(1,1') = \int_t \mathrm{d}2 \int_t \mathrm{d}3 \; G^r(1,2)\Sigma^{\lessgtr}(2,3)G^a(3,1'), \tag{2.67}$$

which will be used many times in actual calculations. The equation for $G^<$ ($G^>$) is a kinetic equation because it contains the particle (hole) distribution as a limiting case. This will be discussed below in Sec. 2.3.5.

2.3.4 More rules for analytic continuation

Beside rules for analytic continuation of "convolutions" on the contour often one also needs to evaluate products parallel or antiparallel in the time arguments, (for instance when one calculates diagrams where several "lines" run between the same vertices)

$$\begin{aligned} C_{\leftleftarrows}(\tau,\tau') &= A(\tau,\tau')B(\tau,\tau'), && (2.68\text{a})\\ C_{\leftrightarrows}(\tau,\tau') &= A(\tau,\tau')B(\tau',\tau). && (2.68\text{b}) \end{aligned}$$

The lesser (greater) part corresponds to the particular ordering of the time arguments on the contour, $\tau \in C_1(C_2)$ and $\tau' \in C_2(C_1)$. From Eq. (2.50)

$$\begin{aligned} C^{\lessgtr}_{\leftleftarrows}(t,t') &= A^{\lessgtr}(t,t')B^{\lessgtr}(t,t'), && (2.69\text{a})\\ C^{\lessgtr}_{\leftrightarrows}(t,t') &= A^{\lessgtr}(t,t')B^{\gtrless}(t',t). && (2.69\text{b}) \end{aligned}$$

In order to find the retarded and advanced parts we insert the above in Eq. (2.48e), e.g.

$$\begin{aligned} C^{r}_{\leftleftarrows}(t,t') &= \theta(t-t')\left[C^{>}(t,t') - C^{<}(t,t')\right]\\ &= \theta(t-t')\left[A^{>}(t,t')B^{>}(t,t') - A^{<}(t,t')B^{<}(t,t')\right]\\ &= \theta(t-t')\left[\{A^{<}(t,t') + A^{r}(t,t') - A^{a}(t,t')\}\right.\\ &\quad \left.\times\{B^{<}(t,t') + B^{r}(t,t') - B^{a}(t,t')\} - A^{<}(t,t')B^{<}(t,t')\right]\\ &= A^{<}(t,t')B^{r}(t,t') + A^{r}(t,t')B^{r}(t,t') + A^{r}(t,t')B^{<}(t,t'). \end{aligned} \tag{2.70}$$

The relevant rules for analytic continuation from the contour to the real time axis are collected in a compact form in Tab. 2.1.

2.3.5 Information contained in the Green's functions

For a novice in nonequilibrium many-particle physics the real-time single-particle Green's functions introduced in Eq. (2.48) may seem to be not that much different. They are all defined in equilibrium theory as well but most studies within this framework require invocation of one Green's function only, usually the retarded one. We stated above that there are in general three linearly independent Green's functions but under certain circumstances relations among them do exist.

One such relation is granted by time-reversal symmetry under steady state conditions. Formally it may be expressed as

$$G^{r}(1,1') = [G^{a}(1',1)]^{*}. \tag{2.71}$$

In steady state situations the Green's functions depend on time differences $t-t'$ only. This allow us to introduce the Fourier transform defined as

$$G^{x}(\mathbf{r}\sigma,\mathbf{r}'\sigma',\omega) \equiv \int_{-\infty}^{\infty} \mathrm{d}t e^{i\omega t/\hbar} G^{x}(\mathbf{r}\sigma,\mathbf{r}'\sigma',t-t'), \quad x \in \{r,a,<,>\}. \tag{2.72}$$

Contour	Real axis
$C = \int_C AB$	$C^{\lessgtr} = \int_{t_1} [A^r B^{\lessgtr} + A^{\lessgtr} B^a]$ $C^{r(a)} = \int_{t_1} A^{r(a)} B^{r(a)}$
$D = \int_C \int_C ABC$	$D^{\lessgtr} = \int_{t_1} \int_{t_2} [A^r B^r C^{\lessgtr} + A^r B^{\lessgtr} C^a + A^{\lessgtr} B^a C^a]$ $D^{r(a)} = \int_{t_1} \int_{t_2} A^{r(a)} B^{r(a)} C^{r(a)}$
$C_{\leftleftarrows}(\tau, \tau') = A(\tau, \tau')B(\tau, \tau')$	$C^{\lessgtr}(t,t') = A^{\lessgtr}(t,t')B^{\lessgtr}(t,t')$ $C^r(t,t') = A^r(t,t')B^<(t,t') + A^<(t,t')B^r(t,t')$ $\quad +A^r(t,t')B^r(t,t')$ $C^a(t,t') = A^a(t,t')B^<(t,t') + A^<(t,t')B^a(t,t')$ $\quad -A^a(t,t')B^a(t,t')$
$C_{\leftrightarrows}(\tau, \tau') = A(\tau, \tau')B(\tau', \tau)$	$C^{\lessgtr}(t,t') = A^{\lessgtr}(t,t')B^{\gtrless}(t',t)$ $C^r(t,t') = A^r(t,t')B^<(t',t) + A^<(t,t')B^a(t',t)$ $C^a(t,t') = A^a(t,t')B^<(t',t) + A^<(t,t')B^r(t',t)$

Table 2.1: *Compact representation of Langreth's theorem and related rules for analytic continuation.*

In steady state the problem is thus reduced to working with two independent Green's functions. This is what we do in the nonequilibrium situations considered in the present work. But, in equilibrium some further relations hold [43]

$$G^<(\mathbf{r}\sigma, \mathbf{r}'\sigma', \omega) = \pm i f(\omega) A(\mathbf{r}\sigma, \mathbf{r}'\sigma', \omega), \tag{2.73a}$$

$$G^>(\mathbf{r}\sigma, \mathbf{r}'\sigma', \omega) = i[\pm f(\omega) - 1] A(\mathbf{r}\sigma, \mathbf{r}'\sigma', \omega), \tag{2.73b}$$

where we introduced the *spectral function* $A(\mathbf{r}\sigma, \mathbf{r}'\sigma', \omega)$

$$A(\mathbf{r}\sigma, \mathbf{r}'\sigma', \omega) \equiv i[G^r(\mathbf{r}\sigma, \mathbf{r}'\sigma', \omega) - G^a(\mathbf{r}\sigma, \mathbf{r}'\sigma', \omega)] \tag{2.74}$$

$$= i[G^>(\mathbf{r}\sigma, \mathbf{r}'\sigma', \omega) - G^<(\mathbf{r}\sigma, \mathbf{r}'\sigma', \omega)], \tag{2.75}$$

and where $f(\omega)$ is the statistical distribution function, either the Fermi-Dirac $n_F(\omega-\mu) = (e^{\beta(\omega-\mu)}+1)^{-1}$ for fermions or the Bose-Einstein $n_B(\omega) = (e^{\beta\omega} - 1)^{-1}$ for bosons. The upper (lower) sign in front of $f(\omega)$ applies to fermions (bosons). Notice that the spectral function is defined in energy space.

We now want to discuss the physical interpretation of the real-time Green's functions, in particular the fermion Green's functions (slightly different interpretations apply to the bosonic case). From their definitions Eq. (2.48) we notice that the retarded Green's function $G^r(1, 1')$ basically answers the following question: If one adds an extra particle with spin σ to the system at space-time $(\mathbf{r}, t)$ what is then the quantum mechanical probability amplitude that one can remove a particle with spin σ' at a later time from space-time $(\mathbf{r}', t')$? The step function $\theta(t - t')$ contained in $G^r(1, 1')$ clearly makes it causal, i.e. the retarded Green's function is a response function for single-particle excitations. The Fourier transform $G^r(\mathbf{r}\sigma, \mathbf{r}'\sigma', \omega)$

correspondingly expresses the probability of adding one particle with spin σ and energy ω at one point in space $\mathbf{r}$ and removing another particle with spin σ' and energy ω at another place $\mathbf{r}'$.

The advanced Green's function $G^a(1,1')$ has a similar interpretation, just with the difference that it expresses how a hole excitation propagates. The combined information about both particle and hole excitations are contained in the spectral function $A(\mathbf{r}\sigma,\mathbf{r}'\sigma',\omega)$ defined in Eq. (2.74). Since particles and holes are treated on equal footing it thus represents the energy resolved density of states.

From Eq. (2.73a) we now see that in equilibrium the lesser Green's function $G^<(\mathbf{r}\sigma,\mathbf{r}'\sigma',\omega)$ is the energy resolved density of particles since it is the density of states $A(\mathbf{r}\sigma,\mathbf{r}'\sigma',\omega)$ multiplied by the statistical probability that these are occupied $n_F(\omega-\mu)$. This interpretation is also valid in nonequilibrium but here there is no simple relation between the density of states and their occupation. Similarly, the fermion greater Green's function $G^>(\mathbf{r}\sigma,\mathbf{r}'\sigma',\omega)$ is the energy resolved density of holes.

Even though that the above mentioned particle and hole excitations are very abstract processes – they do not mimic typical processes in Nature – it turns out that the Green's functions actually contain most of the information one can wish to know about the systems under consideration. In fact, they are directly related to physical observables. In principle the ensemble averages of *any* one-body operator $\mathscr{O}$ can be related to the Green's function by

$$\begin{aligned}
\langle\mathscr{O}(\mathbf{r},t)\rangle &= \mathrm{Tr}[\rho\mathscr{O}(\mathbf{r},t)] \\
&= \mathrm{Tr}[\rho\Psi^\dagger_{\mathscr{H}}(\mathbf{r},t)O(\mathbf{r},t)\Psi_{\mathscr{H}}(\mathbf{r},t)] \\
&= \lim_{\mathbf{r}'\to\mathbf{r}}\lim_{t'\to t+} O(\mathbf{r},t)\mathrm{Tr}[\rho\Psi^\dagger_{\mathscr{H}}(\mathbf{r}',t')\Psi_{\mathscr{H}}(\mathbf{r},t)] \\
&= \lim_{\mathbf{r}'\to\mathbf{r}}\lim_{t'\to t+} O(\mathbf{r},t)\langle\Psi^\dagger_{\mathscr{H}}(\mathbf{r}',t')\Psi_{\mathscr{H}}(\mathbf{r},t)\rangle \\
&= \mp i\hbar\lim_{\mathbf{r}'\to\mathbf{r}}\lim_{t'\to t+} O(\mathbf{r},t)G^<(1,1'),
\end{aligned} \tag{2.76}$$

where $O(\mathbf{r},t)$ is the operator in first quantization [39]. Again the upper (lower) sign applies to fermions (bosons). Consider for example the average of the fermion particle density $n(\mathbf{r},t)\equiv\Psi^\dagger_{\mathscr{H}}(\mathbf{r},t)\Psi_{\mathscr{H}}(\mathbf{r},t)$,

$$\langle n(\mathbf{r},t)\rangle = -i\hbar\lim_{\mathbf{r}'\to\mathbf{r}}\lim_{t'\to t+} G^<(1,1'). \tag{2.77}$$

From this it is evident that the lesser Green's function $G^<(1,1')$ contains the distribution as a limiting case.

2.4 Electron-phonon interaction

We now have the formal tools ready to address the electron-phonon interaction. Besides that we below derive the self-energy expressions used again and again in this thesis, the following also serves as an illustration of the use of Langreth's rules. The approach below was motivated by a study of the work by Hyldgaard *et al.* [52] who – in context of resonant tunneling – considered interaction between a single localized electronic state and a single optical phonon mode. Here we generalize the description to interactions among an arbitrary number of electron states and phonon modes.

Let us consider a coupled electron-phonon system described by the Hamiltonian

$$\begin{aligned}
\mathscr{H} &= \mathscr{H}_{\mathrm{e}} + \mathscr{H}_{\mathrm{ph}} + \mathscr{H}_{\mathrm{e\text{-}ph}}, && (2.78\mathrm{a})\\
\mathscr{H}_{\mathrm{e}} &= \mathscr{H}_{\mathrm{e}}(\{c^\dagger_{k\sigma}\};\{c_{k\sigma}\}), && (2.78\mathrm{b})\\
\mathscr{H}_{\mathrm{ph}} &= \sum_\lambda \Omega_\lambda\Big(b^\dagger_\lambda b_\lambda + \frac{1}{2}\Big), && (2.78\mathrm{c})\\
\mathscr{H}_{\mathrm{e\text{-}ph}} &= \sum_{k,k',\sigma}\sum_\lambda M^\lambda_{k,k'} c^\dagger_{k\sigma} c_{k'\sigma}(b^\dagger_\lambda + b_\lambda). && (2.78\mathrm{d})
\end{aligned}$$

Here the term $\mathscr{H}_{\mathrm{e}}$ describes the electrons in the basis spanned by single-electron states $\{|k\sigma\rangle\}$. The set $(\{c^\dagger_{k\sigma}\};\{c_{k\sigma}\})$ forms a complete, orthonormal set of single-electron creation and annihilation operators. $\mathscr{H}_{\mathrm{ph}}$ is the phonon system Hamiltonian for uncoupled harmonic oscillators with b_λ $(b^\dagger_\lambda)$ being the annihilation (creation) operator in the basis $\{|n_\lambda\rangle\}$. Finally, $\mathscr{H}_{\mathrm{e\text{-}ph}}$ is a general representation of the electron-phonon interaction where $M^\lambda_{k,k'}$ is the (hermitian) interaction matrix element. Basically it expresses the process of an electron being scattered from a state $|k'\rangle$ to $|k\rangle$ accompanied by phonon emission or absorbtion in mode λ. The form of $\mathscr{H}_{\mathrm{e\text{-}ph}}$ written here does not imply momentum conservation since we will consider systems which are not translationally invariant. A graphical representation of the basic electron-phonon vertex is illustrated in Fig. 2.4.

The Hamiltonian put forward in Eq. (2.78) corresponds to the so-called harmonic approximation in which one considers only oscillator displacements to linear order. If the displacements are sufficiently small this is reasonable and one can safely neglect effects related to anharmonicity of the oscillator potential. The Hamiltonian also ignores multi-phonon processes, e.g. when an electron scatters simultaneously with more than one phonon, and direct phonon-phonon interaction. On the other hand we do not consider any particular form of the electronic part $\mathscr{H}_{\mathrm{e}}$ which in principle could contain Coulomb interactions in its full many particle nature or in a mean field approximation.

For this system, in the basis chosen, we define the contour-ordered single-

$M^{\lambda}_{k,k'} =$ 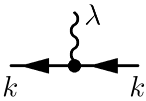

Figure 2.4: *Basic electron-phonon vertex. The full (wiggly) line is the unperturbed electron (phonon) Green's function.*

particle Green's functions

$$\begin{aligned} i\hbar G_{k,k'}(\sigma,\tau,\tau') &\equiv \langle T_C\{c_{k\sigma}(\tau)c^{\dagger}_{k'\sigma}(\tau')\}\rangle, & (2.79a)\\ i\hbar D(\lambda,\tau,\tau') &\equiv \langle T_C\{[b^{\dagger}_{\lambda}(\tau)+b_{\lambda}(\tau)][b^{\dagger}_{\lambda}(\tau')+b_{\lambda}(\tau')]\}\rangle. & (2.79b)\end{aligned}$$

It is convenient to introduce the following matrix notation,

$$\begin{aligned} \mathbf{G}(\sigma,\tau,\tau') &\equiv G_{k,k'}(\sigma,\tau,\tau'), & (2.80a)\\ \mathbf{M}^{\lambda} &\equiv M^{\lambda}_{k,k'}. & (2.80b)\end{aligned}$$

For weak electron-phonon interactions we can treat the problem perturbatively. In the absence of interaction $M^{\lambda}_{k,k'} = 0$ the calculation of electron and the phonon Green's functions Eq. (2.79) are assumed to be soluble problems. Let us denote these unperturbed ones with subscript zero, i.e. $\mathbf{G}_0(\sigma,\tau,\tau')$ and $D_0(\lambda,\tau,\tau')$. They could for instance be the simple free ones described in Appendix A. But often we will describe the electrons in a localized orbital basis in which a finite lifetime is associated with the electronic states. The free electron Green's functions are thus usually not used, even in descriptions where the electron Hamiltonian is bilinear and diagonalization hence possible.

The phonons will though in this thesis be described by the free ones, i.e. we assume that the phonon system Hamiltonian is bilinear as written in Eq. (2.78d). We further assume an equilibrium phonon distribution and thus use Eq. (A.23),

$$\begin{aligned} D^r_0(\lambda,\omega) &= \frac{1}{\omega-\Omega_\lambda+i\eta}-\frac{1}{\omega+\Omega_\lambda+i\eta}, & (2.81a)\\ D^<_0(\lambda,\omega) &= -2\pi i[(N_\lambda+1)\delta(\omega+\Omega_\lambda)+N_\lambda\delta(\omega-\Omega_\lambda)], & (2.81b)\end{aligned}$$

where $N_\lambda \equiv n_B(\Omega_\lambda)$ is the equilibrium occupation number of phonon mode λ.

When electrons and phonons interact via $\mathscr{H}_{\text{e-ph}}$ we can treat the problem perturbatively using the Feynman diagram technique to calculate the interacting Green's functions. In the interaction picture Wick's theorem allows for such a diagrammatic decomposition of the contour-ordered single-particle Green's functions and only connected diagrams need to be considered.

Let us concentrate on the perturbation expansion of the electron Green's function Eq. (2.79a) which generates the types of diagrams shown in Fig. 2.5. The Feynman rules for evaluation of a particular diagram are [37, 38, 39, 40]

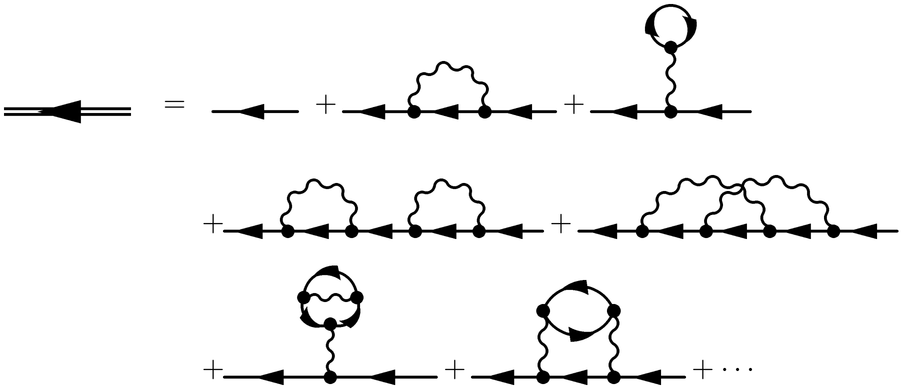

Figure 2.5: *Perturbation expansion for the electron Green's function in a coupled electron-phonon system. The full (wiggly) line is the unperturbed electron (phonon) Green's function.*

1. Interpret each single (double) fermion line as $i\hbar\mathbf{G}_0$ ($i\hbar\mathbf{G}$),
2. interpret each single (double) phonon line as $i\hbar D_0$ ($i\hbar D$),
3. assign a factor $-i\hbar^{-1}M^{\lambda}_{k,k'}$ for each vertex and match indices,
4. take same spin index along connected fermion lines,
5. multiply with $(-1)^l$ where l is the number of Fermion loops,
6. sum over all internal variables,
7. equal time variables must be interpreted as $G(1,1^+)$, i.e. with the second time argument infinitesimally larger than the first.

The proper self-energy is the sum of irreducible diagrams without external lines. Because there are infinitely many one has to approximate it for an actual calculation. This can be done in various ways.

2.4.1 First Born approximation

From the expansion of the electronic Green's function shown in Fig. 2.5 one identifies the lowest order self-energy diagrams in the interaction vertex to be those of Fig. 2.6, referred to as the Hartree- and the Fock-diagrams by analogy to the treatment of the electron-electron interaction. With the Feynman rules one evaluates them to be

$$\mathbf{\Sigma}^{H}_{(1)}(\sigma) = -i\hbar\sum_{\lambda}\sum_{\sigma'}\mathbf{M}^{\lambda}\, D_0(\lambda,\omega=0)\mathrm{Tr}[\mathbf{G}^{<}_0(\sigma',0,0)\mathbf{M}^{\lambda}], \tag{2.82}$$

$$\mathbf{\Sigma}^{F}_{(1)}(\sigma,\tau,\tau') = i\hbar\sum_{\lambda}\mathbf{M}^{\lambda}D_0(\lambda,\tau,\tau')\mathbf{G}_0(\sigma,\tau,\tau')\mathbf{M}^{\lambda}, \tag{2.83}$$

$\mathbf{\Sigma}^{H}_{(1)}(\sigma) =$ 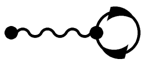 , $\mathbf{\Sigma}^{F}_{(1)}(\sigma,\tau,\tau') =$ 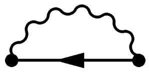

Figure 2.6: *Lowest order self-energy diagrams (Hartree- and Fock-like) for the electron Green's function due to the electron-phonon interaction. The full (wiggly) line is the unperturbed electron (phonon) Green's function.*

With the Langreth's rules for analytic continuation we find for the Hartree diagram

$$\begin{aligned}
\mathbf{\Sigma}^{H,r}_{(1)}(\sigma) &= -i\hbar\sum_{\lambda}\sum_{\sigma'}\mathbf{M}^{\lambda}\; D_0^r(\lambda,\omega=0)\mathrm{Tr}[\mathbf{G}_0^<(\sigma',0,0)\mathbf{M}^{\lambda}] \\
&= i\hbar\sum_{\lambda}\sum_{\sigma'}\frac{2}{\Omega_\lambda}\int_{-\infty}^{\infty}\frac{\mathrm{d}\omega'}{2\pi}\mathbf{M}^{\lambda}\mathrm{Tr}[\mathbf{G}_0^<(\sigma',\omega')\mathbf{M}^{\lambda}], \qquad (2.84\text{a}) \\
\mathbf{\Sigma}^{H,\lessgtr}_{(1)}(\sigma) &= -i\hbar\sum_{\lambda}\sum_{\sigma'}\mathbf{M}^{\lambda}D_0^{\lessgtr}(\lambda,\omega=0)\mathrm{Tr}[\mathbf{G}_0^<(\sigma',0,0)\mathbf{M}^{\lambda}] \\
&= 0, \qquad (2.84\text{b})
\end{aligned}$$

where the phonon Green's functions in energy space were evaluated. The Hartree-diagram is seen to be frequency independent, i.e. it gives a constant contribution. One can show that for translationally invariant systems this diagram vanishes due to momentum conservation. But in general this diagram is important for problems lacking translational invariance [52].

For the Fock diagram one finds

$$\begin{aligned}
\mathbf{\Sigma}^{F,r}_{(1)}(\sigma,t,t') &= i\hbar\sum_{\lambda}\mathbf{M}^{\lambda}[D_0^r(\lambda,t,t')\mathbf{G}_0^<(\sigma,t,t') + D_0^r(\lambda,t,t')\mathbf{G}_0^r(\sigma,t,t') \\
&\qquad + D_0^<(\lambda,t,t')\mathbf{G}_0^r(\sigma,t,t')]\mathbf{M}^{\lambda}, \qquad (2.85\text{a}) \\
\mathbf{\Sigma}^{F,\lessgtr}_{(1)}(\sigma,t,t') &= i\hbar\sum_{\lambda}\mathbf{M}^{\lambda}D_0^{\lessgtr}(\lambda,t,t')\mathbf{G}_0^{\lessgtr}(\sigma,t,t')\mathbf{M}^{\lambda}, \qquad (2.85\text{b})
\end{aligned}$$

which – for steady state were we only consider time differences – has the Fourier transform

$$\begin{aligned}
\mathbf{\Sigma}^{F,r}_{(1)}(\sigma,\omega) &= i\hbar\sum_{\lambda}\int_{-\infty}^{\infty}\frac{\mathrm{d}\omega'}{2\pi}\mathbf{M}^{\lambda}[D_0^r(\lambda,\omega-\omega')\mathbf{G}_0^<(\sigma,\omega') \qquad (2.86\text{a}) \\
&\quad + D_0^r(\lambda,\omega-\omega')\mathbf{G}_0^r(\sigma,\omega') + D_0^<(\lambda,\omega-\omega')\mathbf{G}_0^r(\sigma,\omega')]\mathbf{M}^{\lambda}, \\
\mathbf{\Sigma}^{F,\lessgtr}_{(1)}(\sigma,\omega) &= i\hbar\sum_{\lambda}\int_{-\infty}^{\infty}\frac{\mathrm{d}\omega'}{2\pi}\mathbf{M}^{\lambda}D_0^{\lessgtr}(\lambda,\omega-\omega')\mathbf{G}_0^{\lessgtr}(\sigma,\omega')\mathbf{M}^{\lambda}. \qquad (2.86\text{b})
\end{aligned}$$

Based on the analytic expressions for the phonon Green's functions Eq. (2.81) we see that the Fock diagram contains terms which essentially is Hilbert transforms of the electronic Green's functions and terms in which the energy argument ω is shifted due to δ-function integrations.

The self-energy approximated by the Hartree- and Fock-diagrams – evaluated with unperturbed Green's functions $\mathbf{G}_0(\sigma,\tau,\tau')$ and $D_0(\lambda,\tau,\tau')$ – is conventionally called the first Born approximation (1BA). The real-time Green's function can now be written as

$$\mathbf{G}^{r(a)}_{(1)}(\sigma,\omega) = \Big[[\mathbf{G}^{r(a)}_0(\sigma,\omega)]^{-1} - \mathbf{\Sigma}^{r(a)}_{(1)}(\sigma,\omega)\Big]^{-1}, \tag{2.87a}$$

$$\mathbf{G}^{\lessgtr}_{(1)}(\sigma,\omega) = \mathbf{G}^{r}_{(1)}(\sigma,\omega)\mathbf{\Sigma}^{\lessgtr}_{(1)}(\sigma,\omega)\mathbf{G}^{a}_{(1)}(\sigma,\omega). \tag{2.87b}$$

2.4.2 The Born-Oppenheimer approximation

When electronic and phononic systems interact via a term such as $\mathscr{H}_{\text{e-ph}}$ the question arises whether to study the influence of the interaction on the electrons or on the phonons first [38, 40]. If the interaction is strong enough none of these approaches may work at all. The kind of problems we want to attack here are those of localized vibrations of heavy atoms or whole molecules in some nanoscale system. The large difference in mass between electrons and ions leads to a simplification known as the Born-Oppenheimer approximation, in which the interacting system may be treated in two steps [39]. First, one calculates the behavior of the electrons taking the ions to be fixed at their equilibrium positions. This leads for instance to the derivation of Bloch states in case of a periodic ion potential. This first step thus determines the parameters in the electronic Hamiltonian $\mathscr{H}_{\text{e}}$. Second, the low-frequency ionic motion is computed from the energy changes accompanied by adiabatic displacements of the ions. One thus takes an instantaneous response of the fast electrons into account instead of no response. This second step determines the actual normal modes λ, the energies Ω_λ, and the interaction matrix $\mathbf{M}^\lambda$.

In terms of Green's functions one should therefore study the influence of the bare electron states on the phonons first, and next calculate the effects on the electrons of the renormalized phonon states [40]. In spite of that we will in this thesis assume that the phonon renormalization can be neglected – or rather – simply take the parameters Ω_λ and $\mathbf{M}^\lambda$ to be the renormalized ones. By doing so we miss to capture an eventual reduction of the phonon lifetime.

The above considerations also appeal to Migdal's theorem which states that the phonon-induced renormalization of the electron-phonon vertex scales with the ratio of electron mass to the ion mass [38, 39]. Thus when conditions for Migdal's theorem are fulfilled and the mass ratio is sufficiently small the electron-phonon problem is exactly solved by the above self-energies.

2.4.3 Self-consistent Born approximation

In the perturbative approach a wider subclass of diagrams are included by substituting the bare Green's functions with the full ones in the lowest order self-energy diagrams. This is illustrated for the self-energy to the

Figure 2.7: *Self-energy diagrams in the self-consistent Born approximation (SCBA).*

electron Green's function in Fig. 2.7. This approximation is therefore self-consistent because the Green's function both determines and is determined by the proper self-energy; we denote it the self-consistent Born approximation (SCBA).

Self-consistency here means that the electronic Green's functions in both Dyson's equation and in the self-energy are the same. We thus restrict self-consistency to the electronic system only and leave the phonon Green's functions to be the bare ones,

$$\begin{aligned}
\mathbf{\Sigma}^{H,r}_{\mathrm{SCBA}}(\sigma) &= i\hbar\sum_{\lambda}\sum_{\sigma'}\frac{2}{\Omega_\lambda}\int_{-\infty}^{\infty}\frac{\mathrm{d}\omega'}{2\pi}\mathbf{M}^{\lambda}\mathrm{Tr}[\mathbf{G}^{<}(\sigma',\omega')\mathbf{M}^{\lambda}], && (2.88a)\\
\mathbf{\Sigma}^{H,\lessgtr}_{\mathrm{SCBA}}(\sigma) &= 0, && (2.88b)\\
\mathbf{\Sigma}^{F,r}_{\mathrm{SCBA}}(\sigma,\omega) &= i\hbar\sum_{\lambda}\int_{-\infty}^{\infty}\frac{\mathrm{d}\omega'}{2\pi}\mathbf{M}^{\lambda}[D_0^{r}(\lambda,\omega-\omega')\mathbf{G}^{<}(\sigma,\omega') && (2.88c)\\
&\quad +D_0^{r}(\lambda,\omega-\omega')\mathbf{G}^{r}(\sigma,\omega')+D_0^{<}(\lambda,\omega-\omega')\mathbf{G}^{r}(\sigma,\omega')]\mathbf{M}^{\lambda},\\
\mathbf{\Sigma}^{F,\lessgtr}_{\mathrm{SCBA}}(\sigma,\omega) &= i\hbar\sum_{\lambda}\int_{-\infty}^{\infty}\frac{\mathrm{d}\omega'}{2\pi}\mathbf{M}^{\lambda}D_0^{\lessgtr}(\lambda,\omega-\omega')\mathbf{G}^{\gtrless}(\sigma,\omega')\mathbf{M}^{\lambda}. && (2.88d)
\end{aligned}$$

The self-consistent solution satisfy

$$\begin{aligned}
\mathbf{G}^{r(a)}_{\mathrm{SCBA}}(\sigma,\omega) &= \Big[[\mathbf{G}_0^{r(a)}(\sigma,\omega)]^{-1}-\mathbf{\Sigma}^{r(a)}_{\mathrm{SCBA}}(\sigma,\omega)\Big]^{-1}, && (2.89a)\\
\mathbf{G}^{\lessgtr}_{\mathrm{SCBA}}(\sigma,\omega) &= \mathbf{G}^{r}_{\mathrm{SCBA}}(\sigma,\omega)\mathbf{\Sigma}^{\lessgtr}_{\mathrm{SCBA}}(\sigma,\omega)\mathbf{G}^{a}_{\mathrm{SCBA}}(\sigma,\omega). && (2.89b)
\end{aligned}$$

In this thesis we shall employ this particular self-energy because – as will be shown in the next chapter – it provides a current-conserving approximation, which of course is an essential feature for modelling of electron transport.

Chapter 3

Transport with electron-phonon interaction

3.1 Introduction

In this chapter we derive an expression for the tunneling current through a region of interacting electrons. As is customary we consider both the interactions as well as the hopping to and from electrodes to be turned on adiabatically. If the coupled subsystems have different chemical potentials a net tunneling current of electrons will start to flow.

Since this is a nonequilibrium problem we apply the nonequilibrium Green's function (NEGF) theory as developed in the previous chapter and formulate Dyson's equations for the Green's functions relevant for the model. Instead of solving the full situation with both interactions and hopping one can also treat them in two steps, including one of the effects at the time. Here we will assume the problem of particle interactions in the interacting region has already been solved and accounted for by a suitable self-energy.

The current expression to be derived resembles that of Meir and Wingreen [57] which essentially relates the current to the Green's functions and self-energies for the interacting region only. Their formulation is in principle exact but rely on a somewhat artificial assumption about partitioning of space. Also, often the Green's functions and self-energies entering it can only be obtained approximately. We will especially consider transport through a quantum system inside which electron-phonon interactions are present. As pointed out in Chap. 1 this also leads to a Frölich particle-particle interaction.

In this chapter we further derive a condition for current conservation and show that this is fulfilled by the self-consistent Born approximation (SCBA) for the phonon induced self-energy to the electronic Green's functions. Based upon the ideas for describing the current we end by deriving expressions for the energy flux as well as for energy conservation.

Figure 3.1: *Sketch of a two-terminal setup. The electrodes are assumed to be in local equilibrium characterized by chemical potentials* $\mu_{L/R}$ *also after the hopping terms* $\mathscr{H}_T^{L/R}$ *have been turned on.*

3.2 General expression for the current through an interacting region

We consider a region of interacting electrons coupled to M leads via tunneling terms. The Hamiltonian reads [37, 57]

$$\mathscr{H} = \mathscr{H}_{\text{int}}(\{d_n^\dagger\};\{d_n\}) + \sum_{\alpha=1}^{M} \mathscr{H}_{\text{lead}}^{\alpha} + \sum_{\alpha=1}^{M} \mathscr{H}_{\text{t}}^{\alpha}, \tag{3.1a}$$

$$\mathscr{H}_{\text{lead}}^{\alpha} = \sum_k \xi_{k\alpha} c_{k\alpha}^\dagger c_{k\alpha}, \tag{3.1b}$$

$$\mathscr{H}_{\text{t}}^{\alpha} = \sum_{k,n} \left(V_{k\alpha,n} c_{k\alpha}^\dagger d_n + \text{h.c.} \right), \tag{3.1c}$$

where $c_{k\alpha}^\dagger(c_{k\alpha})$ creates (annihilates) electrons in lead α, and $(\{d_n^\dagger\};\{d_n\})$ form a complete, orthonormal set of single-electron creation and annihilation operators in the interacting region. Similarly $(\{c_{k\alpha}^\dagger\};\{c_{k\alpha}\})$ forms a set for the lead α. There are no direct connections between the leads.

The orthonormality of the basis set as implied by Eq. (3.1) represents a problem: We need to be able to partition space into regions with physical meaning that are correctly described by disjoint Hilbert subspaces and at the same time are connected by a one-body potential $V_{k\alpha,n}$. This is simply not possible. Therefore we need to keep in mind that the outset for the present analysis is based on an *assumption* which is questionable.

3.2.1 The current from lead α

The particle current J^α (per spin) *into* the interacting region from lead α is related to the expectation value of the time derivative of the number operator $\mathscr{N}^\alpha \equiv \sum_k c_{k\alpha}^\dagger c_{k\alpha}$ as

$$J^\alpha = -\langle \dot{\mathscr{N}}^\alpha \rangle = -\frac{i}{\hbar}\langle [\mathscr{H}, \mathscr{N}^\alpha] \rangle = \frac{i}{\hbar} \sum_{k,n} \left(V_{k\alpha,n} \langle c_{k\alpha}^\dagger d_n \rangle - V_{k\alpha,n}^* \langle d_n^\dagger c_{k\alpha} \rangle \right). \tag{3.2}$$

Defining the (hybrid) real-time single-particle Green's functions

$$G^{<}_{k\alpha,n}(t,t') \equiv i\hbar^{-1}\langle d^{\dagger}_{n}(t)c_{k\alpha}(t')\rangle, \tag{3.3a}$$

$$G^{<}_{n,k\alpha}(t,t') \equiv i\hbar^{-1}\langle c^{\dagger}_{k\alpha}(t)d_{n}(t')\rangle, \tag{3.3b}$$

the current may be written in terms of these

$$\begin{aligned} J^{\alpha} &= \sum_{k,n}\Big(V_{k\alpha,n}G^{<}_{n,k\alpha}(t,t) - V^{*}_{k\alpha,n}G^{<}_{k\alpha,n}(t,t)\Big) \\ &= \frac{1}{\hbar}\int_{-\infty}^{\infty}\frac{\mathrm{d}\omega}{2\pi}\sum_{k,n}\Big(V_{k\alpha,n}G^{<}_{n,k\alpha}(\omega) - V^{*}_{k\alpha,n}G^{<}_{k\alpha,n}(\omega)\Big). \end{aligned} \tag{3.4}$$

In order to proceed we need expressions for $G^{<}_{n,k\alpha}(\omega)$ and $G^{<}_{k\alpha,n}(\omega)$. Considering the contour-ordered Green's functions

$$G_{n,k\alpha}(\tau,\tau') \equiv -i\hbar^{-1}\langle T_C[d_n(\tau)c^{\dagger}_{k\alpha}(\tau')]\rangle, \tag{3.5a}$$

$$G_{k\alpha,n}(\tau,\tau') \equiv -i\hbar^{-1}\langle T_C[c_{k\alpha}(\tau)d^{\dagger}_{n}(\tau')]\rangle, \tag{3.5b}$$

$$G_{n,m}(\tau,\tau') \equiv -i\hbar^{-1}\langle T_C[d_n(\tau)d^{\dagger}_{m}(\tau')]\rangle, \tag{3.5c}$$

$$G_{k\alpha,k\alpha}(\tau,\tau') \equiv -i\hbar^{-1}\langle T_C[c_{k\alpha}(\tau)c^{\dagger}_{k\alpha}(\tau')]\rangle, \tag{3.5d}$$

the Dyson equations for $G_{n,k\alpha}$ and $G_{k\alpha,n}$ read

$$G_{n,k\alpha}(\tau,\tau') = \sum_{m}\int_{C}\mathrm{d}\tau_1 G_{n,m}(\tau,\tau_1)V^{*}_{k\alpha,m}G_{k\alpha,k\alpha}(\tau_1,\tau'), \tag{3.6a}$$

$$G_{k\alpha,n}(\tau,\tau') = \sum_{m}\int_{C}\mathrm{d}\tau_1 G_{k\alpha,k\alpha}(\tau,\tau_1)V_{k\alpha,m}G_{m,n}(\tau_1,\tau'). \tag{3.6b}$$

Analytic continuation rules lead to

$$\begin{aligned} G^{<}_{n,k\alpha}(t,t') &= \sum_{m}V^{*}_{k\alpha,m}\int_{-\infty}^{\infty}\mathrm{d}t_1 \qquad (3.7a) \\ &\quad\times\Big[G^{r}_{n,m}(t,t_1)G^{<}_{k\alpha,k\alpha}(t_1,t') + G^{<}_{n,m}(t,t_1)G^{a}_{k\alpha,k\alpha}(t_1,t')\Big], \\ G^{<}_{k\alpha,n}(t,t') &= \sum_{m}V_{k\alpha,m}\int_{-\infty}^{\infty}\mathrm{d}t_1 \qquad (3.7b) \\ &\quad\times\Big[G^{r}_{k\alpha,k\alpha}(t,t_1)G^{<}_{m,n}(t_1,t') + G^{<}_{k\alpha,k\alpha}(t,t_1)G^{a}_{m,n}(t_1,t')\Big]. \end{aligned}$$

Now, in steady state the Green's functions depend on time difference $t-t'$ only, and the above are convolutions that become ordinary products in Fourier space

$$G^{<}_{n,k\alpha}(\omega) = \sum_{m}V^{*}_{k\alpha,m}\Big[G^{r}_{n,m}(\omega)G^{<}_{k\alpha,k\alpha}(\omega) + G^{<}_{n,m}(\omega)G^{a}_{k\alpha,k\alpha}(\omega)\Big], \tag{3.8a}$$

$$G^{<}_{k\alpha,n}(\omega) = \sum_{m}V_{k\alpha,m}\Big[G^{r}_{k\alpha,k\alpha}(\omega)G^{<}_{m,n}(\omega) + G^{<}_{k\alpha,k\alpha}(\omega)G^{a}_{m,n}(\omega)\Big]. \tag{3.8b}$$

Inserting this in Eq. (3.4) using the fundamental relation

$$\mathbf{G}^r - \mathbf{G}^a \equiv \mathbf{G}^> - \mathbf{G}^<, \tag{3.9}$$

(boldface quantities are matrices in the interacting region indices n, m as introduced in Chap. 2) one finds[1]

$$\begin{aligned} J^\alpha &= \frac{1}{\hbar}\int_{-\infty}^{\infty}\frac{\mathrm{d}\omega}{2\pi}\sum_{k,n,m} V^*_{k\alpha,m}V_{k\alpha,n}\left[G^<_{k\alpha,k\alpha}(\omega)G^>_{n,m}(\omega) - G^>_{k\alpha,k\alpha}(\omega)G^<_{n,m}(\omega)\right] \\ &= \frac{1}{\hbar}\int_{-\infty}^{\infty}\frac{\mathrm{d}\omega}{2\pi}\sum_{n,m}\left[\Sigma^{\alpha,<}_{m,n}(\omega)G^>_{n,m}(\omega) - \Sigma^{\alpha,>}_{m,n}(\omega)G^<_{n,m}(\omega)\right] \\ &= \frac{1}{\hbar}\int_{-\infty}^{\infty}\frac{\mathrm{d}\omega}{2\pi}\mathrm{Tr}\left[\mathbf{\Sigma}^{\alpha,<}(\omega)\mathbf{G}^>(\omega) - \mathbf{\Sigma}^{\alpha,>}(\omega)\mathbf{G}^<(\omega)\right], \end{aligned} \tag{3.10}$$

where self-energy $\Sigma^\alpha_{m,n}$ (on the contour) in the interacting region from lead α has been identified,

$$\Sigma^\alpha_{m,n}(\tau,\tau') = \sum_k V^*_{k\alpha,m}G_{k\alpha,k\alpha}(\tau,\tau')V_{k\alpha,n}, \tag{3.11}$$

with lesser and greater parts given by

$$\Sigma^{\alpha,\lessgtr}_{m,n}(\omega) = \sum_k V^*_{k\alpha,m}G^{\lessgtr}_{k\alpha,k\alpha}(\omega)V_{k\alpha,n}. \tag{3.12}$$

The result Eq. (3.10) is a general expression for the particle current (per spin). The integrand has a nice interpretation as the energy resolved *net scattering-in* rate: The part $\hbar^{-1}\mathbf{\Sigma}^{\alpha,<}(\omega)$ $\left(\hbar^{-1}\mathbf{\Sigma}^{\alpha,>}(\omega)\right)$ represents the rate at which particles with energy ω may leave (enter) lead α, cf. Eq. (3.12). Further, $\mathbf{G}^>(\omega)$ $\left(\mathbf{G}^<(\omega)\right)$ expresses the energy resolved probability that the system can accept (donate) a particle of energy ω. In conclusion we thus interpret $\hbar^{-1}\mathbf{\Sigma}^{\alpha,<}(\omega)\mathbf{G}^>(\omega)$ as the total energy resolved *scattering-in* rate and $\hbar^{-1}\mathbf{\Sigma}^{\alpha,>}(\omega)\mathbf{G}^<(\omega)$ correspondingly as the total energy resolved *scattering-out* rate.

3.2.2 Lead α in equilibrium

If we assume the lead electrons are in local equilibrium with chemical potential μ_α – also after the coupling between the leads and the central region has been turned on – we can express $G^{\lessgtr}_{k\alpha,k\alpha}$ using the equilibrium relations Eq. (2.73),

$$\begin{aligned} G^{\lessgtr}_{k\alpha,k\alpha}(\omega) &= \begin{cases} in_F(\omega-\mu_\alpha)A_0(k,\omega) \\ i\{n_F(\omega-\mu_\alpha)-1\}A_0(k,\omega) \end{cases} \\ &= \begin{cases} 2\pi in_F(\omega-\mu_\alpha)\delta(\omega-\varepsilon_k) \\ 2\pi i\{n_F(\omega-\mu_\alpha)-1\}\delta(\omega-\varepsilon_k) \end{cases}, \end{aligned} \tag{3.13}$$

---

[1] The gauge invariance, i.e. the invariance under a global shift of the external electric potentials, will not be discussed here. For a such the reader is referred to e.g. Stafford [62].

where $n_F(\omega) = (e^{\beta\omega}+1)^{-1}$ is the Fermi distribution and where $A_0(k,\omega)= 2\pi\delta(\omega-\varepsilon_k)$ the spectral function for free fermions, cf. Appendix A.

In order to find expressions for the self-energies $\Sigma^{\alpha,\lessgtr}_{m,n}(\omega)$ in Eq. (3.12), we replace the sum over k with an energy integration,

$$\sum_k \longrightarrow \int_{-\infty}^{\infty} \mathrm{d}\varepsilon_k \rho_\alpha(\varepsilon_k), \tag{3.14}$$

where $\rho_\alpha(\varepsilon_k)$ is the density of states in lead α, and find

$$\begin{aligned} \Sigma^{\alpha,\lessgtr}_{m,n}(\omega) &= \int_{-\infty}^{\infty} \mathrm{d}\varepsilon_k \, \underbrace{\rho_\alpha(\varepsilon_k)V^*_{\alpha,m}(\varepsilon_k)V_{\alpha,n}(\varepsilon_k)}_{\Gamma^\alpha_{m,n}(\varepsilon_k)/2\pi} G^{\lessgtr}_{k\alpha,k\alpha}(\omega) \\ &= \left\{ \begin{array}{l} in_F(\omega-\mu_\alpha)\Gamma^\alpha_{m,n}(\omega) \\ i\{n_F(\omega-\mu_\alpha)-1\}\Gamma^\alpha_{m,n}(\omega) \end{array} \right. , \end{aligned} \tag{3.15}$$

written in terms of the level-width function $\Gamma^\alpha_{m,n}(\omega)$ which of course depends on the potentials in both the lead and the interacting region.

With these self-energies the particle current expression Eq. (3.10) takes the form of Meir and Wingreen [57]

$$J^\alpha = \frac{1}{\hbar}\int_{-\infty}^{\infty} \frac{\mathrm{d}\omega}{2\pi} \mathrm{Tr}\left[\mathbf{\Gamma}^\alpha(\omega) i\mathbf{G}^<(\omega) + n_F(\omega-\mu_\alpha)\mathbf{\Gamma}^\alpha(\omega)\mathbf{A}(\omega)\right]. \tag{3.16}$$

3.2.3 Noninteracting current

Let us now consider the case of a noninteracting systems coupled to two electrodes (L/R) described by the self-energies

$$\mathbf{\Sigma}^<_{L/R}(\omega) = in_F(\omega-\mu_{L/R})\mathbf{\Gamma}_{L/R}(\omega), \tag{3.17a}$$

$$\mathbf{\Sigma}^>_{L/R}(\omega) = i\{n_F(\omega-\mu_{L/R})-1\}\mathbf{\Gamma}_{L/R}(\omega). \tag{3.17b}$$

Since there are no additional self-energies in the problem the Keldysh equations Eq. (2.67) simply read

$$\mathbf{G}^{\lessgtr}(\omega) = \mathbf{G}^r(\omega)\left[\mathbf{\Sigma}^{\lessgtr}_L(\omega) + \mathbf{\Sigma}^{\lessgtr}_R(\omega)\right]\mathbf{G}^a(\omega) \tag{3.18}$$

The particle current from left lead can be written as

$$\begin{aligned} J_L &= \frac{1}{\hbar}\int_{-\infty}^{\infty} \frac{\mathrm{d}\omega}{2\pi} \mathrm{Tr}\left[\mathbf{\Sigma}^<_L(\omega)\mathbf{G}^>(\omega) - \mathbf{\Sigma}^>_L(\omega)\mathbf{G}^<(\omega)\right], \\ &= \frac{1}{\hbar}\int_{-\infty}^{\infty} \frac{\mathrm{d}\omega}{2\pi} T_{\mathrm{tot}}(\omega)[n_F(\omega-\mu_L) - n_F(\omega-\mu_R)] \end{aligned} \tag{3.19}$$

where the noninteracting transmission probability function has been identified[2]

$$T_{\mathrm{tot}}(\omega) = \mathrm{Tr}[\mathbf{\Gamma}_L(\omega)\mathbf{G}^r(\omega)\mathbf{\Gamma}_R(\omega)\mathbf{G}^a(\omega)]. \tag{3.20}$$

---

[2] The connection between the transmission function and the Green's functions is essentially established via the Fisher-Lee relation [32, 63].

Notice that

$$n_F(\omega-\mu_L)-n_F(\omega-\mu_R) \;=\; n_F(\widetilde{\omega}-eV/2)-n_F(\widetilde{\omega}+eV/2) \qquad (3.21)$$

where $\mu_L=\mu_R+eV$ and $\widetilde{\omega}=\omega-\mu_L+eV/2$. This implies that if $T(\omega)$ is independent of bias the current is an odd function with respect to the bias voltage V. If we make a Taylor expansion of the Fermi distributions in the bias to first order

$$n_F(\widetilde{\omega}+eV/2)-n_F(\widetilde{\omega}-eV/2)\approx eV\Big(\frac{\partial n_F(\widetilde{\omega})}{\partial\widetilde{\omega}}\Big)_{V=0}, \qquad (3.22)$$

we see that if the transmission function is constant for the energies over which the Fermi surface is thermally smeared the zero bias conductance just takes the form of the famous Landauer formula [32]

$$G \;=\; \frac{2e^2}{h}T(\mu), \qquad (3.23)$$

where $\mu=\mu_L=\mu_R$ and a factor of two appears due to spin degeneracy.

3.3 Conservation of current

With the Keldysh equations for steady state Eq. (2.67),

$$\mathbf{G}^{\lessgtr}(\omega) \;=\; \mathbf{G}^r(\omega)\mathbf{\Sigma}^{\lessgtr}_{\text{tot}}(\omega)\mathbf{G}^a(\omega), \qquad (3.24)$$

i.e. $\mathbf{\Sigma}^{\lessgtr}_{\text{tot}}$ being the sum of all self-energy contributions stemming from leads and “internal” interactions, we can derive a useful relation from Eq. (3.9) [32]

$$(\mathbf{G}^a)^{-1}-(\mathbf{G}^r)^{-1} \;=\; (\mathbf{G}^r)^{-1}(\mathbf{G}^>-\mathbf{G}^<)(\mathbf{G}^a)^{-1}=\mathbf{\Sigma}^>_{\text{tot}}-\mathbf{\Sigma}^<_{\text{tot}}. \qquad (3.25)$$

We are now in position to prove an important cancellation

$$\begin{aligned}
&\mathrm{Tr}\left[\mathbf{\Sigma}^<_{\text{tot}}\mathbf{G}^>-\mathbf{\Sigma}^>_{\text{tot}}\mathbf{G}^<\right]\\
&=\mathrm{Tr}\left[\mathbf{\Sigma}^<_{\text{tot}}\mathbf{G}^r\mathbf{\Sigma}^>_{\text{tot}}\mathbf{G}^a-\mathbf{\Sigma}^>_{\text{tot}}\mathbf{G}^r\mathbf{\Sigma}^<_{\text{tot}}\mathbf{G}^a\right]\\
&=\mathrm{Tr}\left[\mathbf{\Sigma}^<_{\text{tot}}\mathbf{G}^r\{\mathbf{\Sigma}^<_{\text{tot}}+(\mathbf{G}^a)^{-1}-(\mathbf{G}^r)^{-1}\}\mathbf{G}^a\right.\\
&\qquad\left.-\{\mathbf{\Sigma}^<_{\text{tot}}+(\mathbf{G}^a)^{-1}-(\mathbf{G}^r)^{-1}\}\mathbf{G}^r\mathbf{\Sigma}^<_{\text{tot}}\mathbf{G}^a\right]\\
&=\mathrm{Tr}\left[\mathbf{\Sigma}^<_{\text{tot}}\mathbf{G}^r\{(\mathbf{G}^a)^{-1}-(\mathbf{G}^r)^{-1}\}\mathbf{G}^a-\{(\mathbf{G}^a)^{-1}-(\mathbf{G}^r)^{-1}\}\mathbf{G}^r\mathbf{\Sigma}^<_{\text{tot}}\mathbf{G}^a\right]\\
&=\mathrm{Tr}\left[\mathbf{\Sigma}^<_{\text{tot}}\{\mathbf{G}^r-\mathbf{G}^a\}-\{\mathbf{G}^r-\mathbf{G}^a\}\mathbf{\Sigma}^<_{\text{tot}}\right]\equiv 0. \qquad (3.26)
\end{aligned}$$

Splitting the total self-energy into contributions from “internal” interactions and from the leads,

$$\mathbf{\Sigma}^{\lessgtr}_{\text{tot}}(\omega) \;=\; \mathbf{\Sigma}^{\lessgtr}_{\text{int}}(\omega)+\sum_{\alpha=1}^{M}\mathbf{\Sigma}^{\alpha,\lessgtr}(\omega), \qquad (3.27)$$

the current conservation condition

$$\sum_{\alpha=1}^{M}J^\alpha=0, \qquad (3.28)$$

implies the following constraint on the self-energy $\mathbf{\Sigma}_{\text{int}}$

$$
\begin{aligned}
\sum_{\alpha=1}^{M} J^{\alpha} &= \sum_{\alpha} \frac{1}{\hbar} \int_{-\infty}^{\infty} \frac{\mathrm{d}\omega}{2\pi} \mathrm{Tr}\left[\mathbf{\Sigma}^{\alpha,<}(\omega)\mathbf{G}^{>}(\omega) - \mathbf{\Sigma}^{\alpha,>}(\omega)\mathbf{G}^{<}(\omega)\right] \\
&= \frac{1}{\hbar} \int_{-\infty}^{\infty} \frac{\mathrm{d}\omega}{2\pi} \mathrm{Tr}\left[\{\mathbf{\Sigma}_{\text{tot}}^{<}(\omega) - \mathbf{\Sigma}_{\text{int}}^{<}(\omega)\}\mathbf{G}^{>}(\omega)\right. \\
&\qquad\qquad \left. - \{\mathbf{\Sigma}_{\text{tot}}^{>}(\omega) - \mathbf{\Sigma}_{\text{int}}^{>}(\omega)\}\mathbf{G}^{<}(\omega)\right] \\
&= \frac{1}{\hbar} \int_{-\infty}^{\infty} \frac{\mathrm{d}\omega}{2\pi} \mathrm{Tr}\left[-\mathbf{\Sigma}_{\text{int}}^{<}(\omega)\mathbf{G}^{>}(\omega) + \mathbf{\Sigma}_{\text{int}}^{>}(\omega)\mathbf{G}^{<}(\omega)\right] = 0? \qquad (3.29)
\end{aligned}
$$

Obviously this shows that if there are no internal interactions the current is conserved. The situation is different in the interacting case. Here we want to describe the internal interactions in terms of appropriate self-energies, but such can often only be obtained approximately. Therefore one may (unintentionally) choose an approximation which violates of the continuity equation, which of course is not physical. Eq. (3.29) thus provides a way to test if the self-energy approximation is current conserving.

3.3.1 Current conservation in SCBA

We are now in position to show that the self-consistent Born approximation (SCBA) for the electron-phonon interaction is current conserving. In this approximation scheme the lesser and greater self-energies are given by Eq. (2.88),

$$
\mathbf{\Sigma}_{\text{SCBA}}^{\lessgtr}(\sigma,\omega) = i\hbar \sum_{\lambda} \int_{-\infty}^{\infty} \frac{\mathrm{d}\omega'}{2\pi} \mathbf{M}^{\lambda} D_0^{\lessgtr}(\lambda,\omega-\omega')\mathbf{G}^{\lessgtr}(\sigma,\omega')\mathbf{M}^{\lambda}. \qquad (3.30)
$$

Considering equilibrium phonons,

$$
D_0^{\lessgtr}(\lambda,\omega) = -2\pi i[(N_{\lambda}+1)\delta(\omega \pm \Omega_{\lambda}) + N_{\lambda}\delta(\omega \mp \Omega_{\lambda})], \qquad (3.31)
$$

the integral over ω' in Eq. (3.30) can be performed yielding

$$
\mathbf{\Sigma}_{\text{SCBA}}^{\lessgtr}(\omega) = i\hbar \sum_{\lambda} \mathbf{M}^{\lambda}\{(N_{\lambda}+1)\mathbf{G}^{\lessgtr}(\omega \pm \Omega_{\lambda}) + N_{\lambda}\mathbf{G}^{\lessgtr}(\omega \mp \Omega_{\lambda})\}\mathbf{M}^{\lambda}, \qquad (3.32)
$$

When Eq. (3.32) is inserted in Eq. (3.29), and a variable substitution as well as a cyclic permutation in the trace is used, one finds

$$
\begin{aligned}
\sum_{\alpha=1}^{M} J^{\alpha} &= i \sum_{\lambda} \int_{-\infty}^{\infty} \frac{\mathrm{d}\omega}{2\pi} \\
&\quad \times \mathrm{Tr}\{-\mathbf{M}^{\lambda}[(N_{\lambda}+1)\mathbf{G}^{<}(\omega+\Omega_{\lambda}) + N_{\lambda}\mathbf{G}^{<}(\omega-\Omega_{\lambda})]\mathbf{M}^{\lambda}\mathbf{G}^{>}(\omega) \\
&\qquad + \mathbf{M}^{\lambda}[(N_{\lambda}+1)\mathbf{G}^{>}(\omega-\Omega_{\lambda}) + N_{\lambda}\mathbf{G}^{>}(\omega+\Omega_{\lambda})]\mathbf{M}^{\lambda}\mathbf{G}^{<}(\omega)\} \\
&= 0, \qquad (3.33)
\end{aligned}
$$

i.e. that the SCBA really *is* current conserving.

3.4 Energy flux and energy conservation

Along similar lines as of the derivation of the current expression we can also consider the flow of energy through the system. The energy flux P^α *into* the interacting region from lead α is defined as

$$\begin{aligned} P^\alpha &\equiv -\langle \dot{\mathscr{H}}^\alpha_{\mathrm{lead}} \rangle = -\frac{i}{\hbar}\langle [\mathscr{H}, \mathscr{H}^\alpha_{\mathrm{lead}}] \rangle \\ &= \frac{i}{\hbar}\sum_{k,n}(\varepsilon_{k\alpha}-\mu_\alpha)\Big(V_{k\alpha,n}\langle c^\dagger_{k\alpha} d_n\rangle - V^*_{k\alpha,n}\langle d^\dagger_n c_{k\alpha}\rangle\Big). \end{aligned} \tag{3.34}$$

Similar to Eq. (3.10) we find that this can be written as[3]

$$\begin{aligned} P^\alpha &= \frac{1}{\hbar}\int_{-\infty}^{\infty}\frac{\mathrm{d}\omega}{2\pi}(\omega-\mu_\alpha)\mathrm{Tr}\left[\mathbf{\Sigma}^{\alpha,<}(\omega)\mathbf{G}^>(\omega) - \mathbf{\Sigma}^{\alpha,>}(\omega)\mathbf{G}^<(\omega)\right] \\ &= \frac{1}{\hbar}\int_{-\infty}^{\infty}\frac{\mathrm{d}\omega}{2\pi}\,\omega\mathrm{Tr}\left[\mathbf{\Sigma}^{\alpha,<}(\omega)\mathbf{G}^>(\omega) - \mathbf{\Sigma}^{\alpha,>}(\omega)\mathbf{G}^<(\omega)\right] - \mu_\alpha J^\alpha. \end{aligned} \tag{3.35}$$

Now, summing the flux from all leads gives the total incoming power to the system

$$\sum_{\alpha=1}^{M} P^\alpha = \frac{1}{\hbar}\int_{-\infty}^{\infty}\frac{\mathrm{d}\omega}{2\pi}\,\omega\mathrm{Tr}\left[-\mathbf{\Sigma}^<_{\mathrm{int}}(\omega)\mathbf{G}^>(\omega) + \mathbf{\Sigma}^>_{\mathrm{int}}(\omega)\mathbf{G}^<(\omega)\right] - \sum_{\alpha=1}^{M}\mu_\alpha J^\alpha \tag{3.36}$$

In the above μ_α is the reference to which we measure single-particle energies in reservoir α. For the system as a whole we want to measure these with respect to a common reference point, and we can take $\mu_\alpha = e\phi_{\mathrm{ref}}$. This implies that the last term in Eq. (3.36) vanishes $\sum_{\alpha=1}^{M}\mu_\alpha J^\alpha = e\phi_{\mathrm{ref}}\sum_{\alpha=1}^{M} J^\alpha = 0$ due to current conservation.

We interpret the total incoming power to the system as being transmitted to the phonon system, i.e. that

$$P_{\mathrm{ph}} = \sum_{\alpha=1}^{M} P^\alpha \tag{3.37}$$

$$= \frac{1}{\hbar}\int_{-\infty}^{\infty}\frac{\mathrm{d}\omega}{2\pi}\,\omega\mathrm{Tr}\left[-\mathbf{\Sigma}^<_{\mathrm{int}}(\omega)\mathbf{G}^>(\omega) + \mathbf{\Sigma}^>_{\mathrm{int}}(\omega)\mathbf{G}^<(\omega)\right]. \tag{3.38}$$

We see that if there are no interactions there are no dissipation inside the system (the electrons dissipate their energy deep inside the reservoirs). The situation is different with an electron-phonon interaction where electrons can transmit energy to the ionic oscillators by emitting phonons. In our approach (within 1BA/SCBA) we do not treat such heating effects since we have modelled the phonon system as unperturbed by the electrons. Thus, any power transmitted according to Eq. (3.38) must be interpreted as being immediately absorbed from the phonon modes into some external thermostat.

---

[3] Using that the leads are “diagonalizable,” i.e. that we can use $\delta(\omega-\varepsilon_k)$ to make the substitution $\omega \leftrightarrow \varepsilon_k$.

Chapter 4

Numerical implementation

4.1 Introduction

This chapter concerns the numerical implementation of the nonequilibrium Green's function (NEGF) formulation put forward in the previous chapters for inelastic transport in nanosystems.

For several reasons the choice of programming language fell on the high-level language PYTHON [64]. First of all it is an open source software which has gained widespread use for scientific computing with a variety of extension modules available. PYTHON is an interpreted language which makes the development of programs relatively easy and fast and its object oriented programming abilities allow for writing efficient and compact codes. On the other hand PYTHON programs can be very fast and handle huge arrays of data in an efficient manner because critical computations may be carried out by interfacing various state-of-the-art low-level routines.

A further motivation for this choice of language was also to acquire programming skills compatible with existing in-house software at the Department of Micro and Nanotechnology, since PYTHON offers effective linking to routines written in both C and FORTRAN, and to binary data file structures in NETCDF (network Common Data Form).

As we have seen in Chap. 3 the Green's functions and self-energies involved in the theoretical description of inelastic electron transport have been given matrix representations with each element being a function of energy. For a numerical treatment we sample these functions on an energy grid which effectively makes the Green's functions and the self-energies three-dimensional data structures. Such multidimensional structures – and typical operations on them – are featured in the extension module NUMERICAL PYTHON which also provides interface to FFT and LAPACK FORTRAN libraries. This extension module was therefore used in the present implementation.

4.2 Program structure

The method developed in this project for calculation of current-voltage (I–V) characteristics of nanosystems has the structure illustrated in Fig. 4.1. Initially one sets up the parameters describing the system. This include the Hamiltonian $\mathbf{H}$ for bare electrons in the interacting region (without the phonons), an interaction matrix $\mathbf{M}^{\lambda}$ for a single phonon mode λ with energy Ω_{λ}, a temperature T characterizing both the equilibrium distribution of electrons in the leads as well as the phonon mode occupation, the equilibrium chemical potential $\mu_{\rm eq}$ for the filling level of the system, and the retarded self-energies $\mathbf{\Sigma}^{r}_{L/R}(\omega)$ due to coupling to the leads.

Concerning the numerical calculation there are two important settings. One is the energy grid of linearly spaced points ω_i used for the numerical sampling. It should span a sufficiently large energy range while at the same time resolve the variations of all Green's functions, self-energies, etc. Also there is a setting $\Delta_{\rm conv}$ which sets a convergence criterium for the iteration procedure towards self-consistency.

The calculation of a complete I–V device characteristic now proceeds as independent computations of the current for different bias conditions. These bias settings determine the lesser self-energy

$$\mathbf{\Sigma}^{<}_{L/R}(\omega_i) \;=\; n_F(\omega_i-\mu_{L/R})\Big[\mathbf{\Sigma}^{a}_{L/R}(\omega_i)-\mathbf{\Sigma}^{r}_{L/R}(\omega_i)\Big], \tag{4.1}$$

and hence also the Green's functions

$$\mathbf{G}^{0,r}(\omega_i) \;=\; \Big[(\omega_i+i\eta)\mathbf{1}-\mathbf{H}-\mathbf{\Sigma}^{r}_{L}(\omega_i)-\mathbf{\Sigma}^{r}_{R}(\omega_i)\Big]^{-1}, \tag{4.2a}$$

$$\mathbf{G}^{0,<}(\omega_i) \;=\; \mathbf{G}^{r}(\omega_i)\Big[\mathbf{\Sigma}^{<}_{\rm L}(\omega_i)+\mathbf{\Sigma}^{<}_{\rm R}(\omega_i)\Big]\mathbf{G}^{a}(\omega_i). \tag{4.2b}$$

for the system without the electron-phonon interaction. Since we are considering steady state it is – as pointed out in Chap. 2 – sufficient to work with two independent Green's functions; these are usually the retarded and the lesser ones. At this point we can compute the noninteracting current for a later comparison with the interacting result. Optionally the program also outputs other information derived from the Green's functions, e.g. the spectral function $\mathbf{A}_0(\omega)$.

The next step is an attempt to find the self-consistent solution for the interacting Green's functions and the electron-phonon self-energies, cf. Eq. (2.89)

$$\mathbf{G}^{r}(\omega_i) \;=\; \Big[(\omega_i+i\eta)\mathbf{1}-\mathbf{H}-\mathbf{\Sigma}^{r}_{L}(\omega_i)-\mathbf{\Sigma}^{r}_{R}(\omega_i)-\mathbf{\Sigma}^{r}_{\rm ph}(\omega_i)\Big]^{-1}, \tag{4.3a}$$

$$\mathbf{G}^{<}(\omega_i) \;=\; \mathbf{G}^{r}(\omega_i)\Big[\mathbf{\Sigma}^{<}_{\rm L}(\omega_i)+\mathbf{\Sigma}^{<}_{\rm R}(\omega_i)+\mathbf{\Sigma}^{<}_{\rm ph}(\omega_i)\Big]\mathbf{G}^{a}(\omega_i). \tag{4.3b}$$

For relatively weak electron-phonon interaction it is possible to obtain the self-consistent solution simply by straight forward iteration of the above expressions. But for stronger interactions more sophisticated schemes are

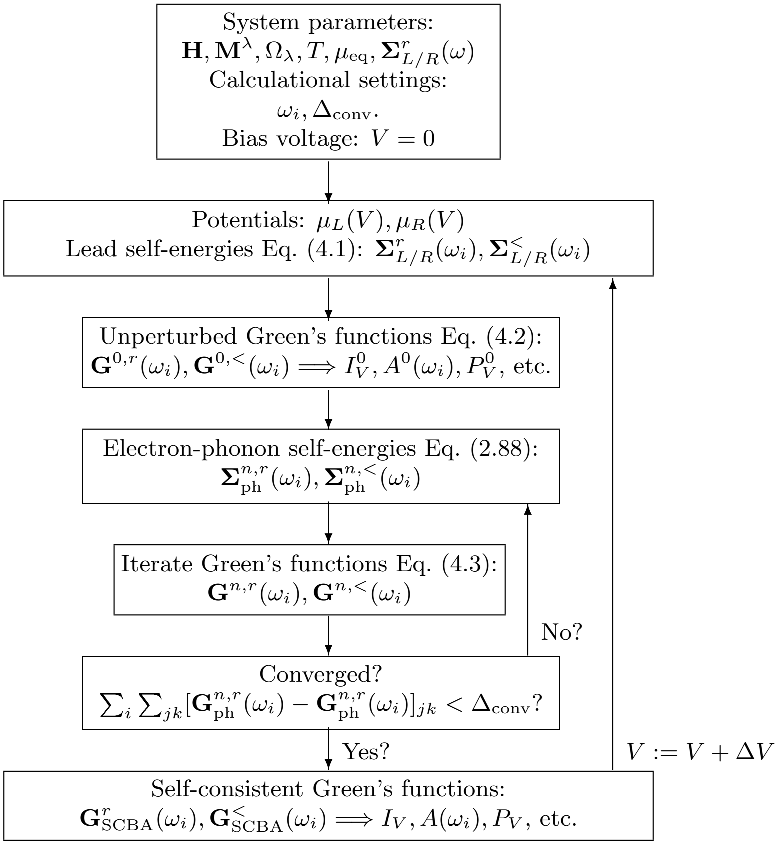

Figure 4.1: *Block diagram illustrating the iterative procedure used to calculate a device $I - V$ characteristic.*

often necessary. One such strategy is to slowly ramp up the interaction, i.e. to obtain the self-consistent solution corresponding to $x\mathbf{M}^\lambda,\ x \leq 1$ which then is taken as initial guess for the increased interaction $(x + \delta x)\mathbf{M}^\lambda$.

At the end of each cycle in the iteration procedure towards self-consistency one computes the sum of element-wise distances between the newly obtained and the previous retarded Green's function. If this sum is lower than Δ_{conv} the iteration is considered to have converged and the self-consistent Green's functions determined.

The calculation ends by computation of the interacting current Eq. (3.10), and optionally other properties such as the spectral function $\mathbf{A}(\omega)$ or the power P_{sys} transmitted Eq. (3.38). The procedure just described can now be repeated for another bias voltage. A full I–V curve should finally be checked to be robust against changes of the calculational settings.

It is worth mentioning that in the iteration procedure outlined above the computation of the retarded electron-phonon self-energy involves a Hilbert transform of the electron Green's functions. This is because the Fock-like diagram (Fig. 2.6) evaluated with free phonon propagators $D_0^r(\lambda,\omega)$ involve terms of the form

$$\mathscr{P}\int \frac{\mathrm{d}\omega'}{2\pi}\frac{\mathbf{G}^r(\sigma,\omega') + \mathbf{G}^<(\sigma,\omega')}{\omega - \omega' \pm \Omega_\lambda}. \tag{4.4}$$

With a discrete representation of the electron Green's functions the Hilbert transform can conveniently be calculated utilizing the Fast Fourier Transform (FFT) algorithm. The technical details of how this was implemented are found in Appendix B.

Chapter 5

Resonant tunneling through a single electronic state

5.1 Introduction

This chapter provides a documentation of the transport code developed in Python as described in Chap. 4 by comparing with results reported in the literature. We compare with some of the work by several researchers from the early 1990s on resonant tunneling in semiconductor double-barrier structures [47, 48, 49, 50, 51, 52]. In particular we will focus on the results by Wingreen *et al.* [48] and by Hyldgaard *et al.* [52].

We consider a region between two ideal leads described by a Hamiltonian

$$\begin{aligned} \mathscr{H} &= \mathscr{H}_{\mathrm{e}} + \mathscr{H}_{\mathrm{ph}} + \mathscr{H}_{\text{e-ph}}, && (5.1a)\\ \mathscr{H}_{\mathrm{e}} &= \sum_{\sigma} \varepsilon_0 d^\dagger_\sigma d_\sigma, && (5.1b)\\ \mathscr{H}_{\mathrm{ph}} &= \Omega b^\dagger b\ , && (5.1c)\\ \mathscr{H}_{\text{e-ph}} &= \sum_{\sigma} M d^\dagger_\sigma d_\sigma (b^\dagger + b), && (5.1d) \end{aligned}$$

where ε_0 is a single electronic level created in a double-barrier potential well, Ω is the energy of an optical phonon mode, and M the electron-phonon interaction element.

In order to calculate the current we need the Green's function for the central site and appropriate self-energies from the leads. In absence of electron-phonon interaction the problem of hopping to and from ideal leads can be exactly solved. The central site Green's functions are simply

$$\begin{aligned} G^{0,r}(\sigma,\omega) &= \frac{1}{\omega - \varepsilon_0 + i\eta - \Sigma^r_L(\omega) - \Sigma^r_R(\omega)}, && (5.2a)\\ G^{0,<}(\sigma,\omega) &= |G^{0,r}(\sigma,\omega)|^2 \Big[\Sigma^<_L(\omega) + \Sigma^<_R(\omega)\Big], && (5.2b) \end{aligned}$$

Physical quantity	Symbol	WBL-SPA	WBL	Semi-elliptic
Electrode band-width	W	∞	∞	5.70
Lower band edge	ϕ	$-\infty$	$-\infty$	-0.70
Escape rate (FWHM)	Γ	0.05	0.05	0.055
Nonint. resonance level	ε_0	10.00	0.00	0.57
Equilibr. chem. potential	μ	0.00	0.00	0.00
Phonon mode energy	Ω	1.00	1.00	1.00
Electron-phonon coupl.	M	0.32	0.32	0.32
Temperature	k_BT	0.001	$0.001, 0.020, 0.040$	0.010
Reference		Fig. 5.2	Fig. 5.3, 5.4, 5.5	5.6

Table 5.1: *Parameters characterizing three different systems for which the resonant tunneling currents have been calculated. The energy scale is set by the phonon mode energy* Ω.

where the self-energies due to the leads are customarily expressed as

$$\Sigma^r_{L/R}(\omega) \;=\; \Delta_{L/R}(\omega) - i\Gamma_{L/R}(\omega)/2, \tag{5.3a}$$

$$\Sigma^<_{L/R}(\omega) \;=\; in_F(\omega - \mu_{L/R})\Gamma_{L/R}(\omega), \tag{5.3b}$$

valid for leads in (local) equilibrium. Both $\Delta_{L/R}(\omega)$ and $\Gamma_{L/R}(\omega)$ are defined as real functions. The first of them represents an energy dependent renormalization of the resonant level, while the second can be interpreted as an escape rate that effectively broadens the level spectral function.

Below we consider some specific approximations for $\Delta_{L/R}(\omega)$ and $\Gamma_{L/R}(\omega)$ characterized by the following electrode parameters: Band-width W, lower band edge ϕ, and escape rate strength Γ. In particular we consider three different systems with parameters as listed in Tab. 5.1.

5.2 Wide-band limit

The simplest approximation for the lead self-energies is the so-called wide-band limit (WBL) in which one takes $\Delta(\omega) = 0$, $\Gamma(\omega) = \Gamma$ and $W \to \infty$. In this situation the propagator (retarded Green's function) of the localized state acquires a well-defined life-time as set by the total escape rate $\Gamma \equiv \Gamma_L + \Gamma_R$, and the corresponding unperturbed spectral function $A_0(\omega)$ becomes a Lorentzian

$$A_0(\omega) \;=\; \frac{\Gamma}{(\omega - \varepsilon_0)^2 + (\Gamma/2)^2}, \tag{5.4}$$

where Γ is the full width half maximum (FWHM). A schematic of the system in equilibrium is shown in Fig. 5.1.

5.2.1 Single particle limit

The first case we want to study is the single particle approximation (SPA). Physically, this limit corresponds to the electronic level being far above the

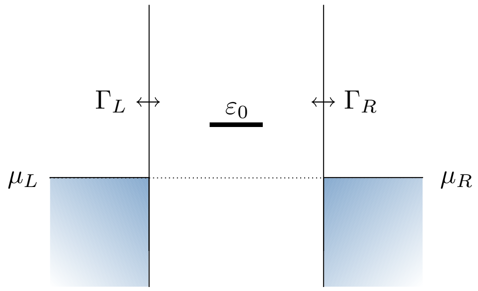

Figure 5.1: *Schematic of resonant tunneling through a localized level in WBL.*

Fermi levels in the reservoirs, cf. Fig. 5.1. For this particular limit the electron-phonon interaction problem can be solved exactly as was done by Wingreen, Jacobsen, and Wilkins [47]. They determined the total transmission probability $T_{\mathrm{tot}}(\omega)$ at zero temperature for an electron tunneling through a level ε_0 coupled to an optical phonon mode with energy Ω. Their result is

$$\begin{aligned} T_{\mathrm{tot}}(\omega) &= \Gamma_L \Gamma_R e^{-2g} \sum_{m=0}^{\infty} \frac{g^m}{m!} \qquad (5.5) \\ &\times \left| \sum_{j=0}^{m} (-1)^j \binom{m}{j} \sum_{l=0}^{\infty} \left(\frac{1}{\omega - (\varepsilon_0 - g\Omega) - (j+l)\Omega + i\Gamma/2} \right) \right|^2, \end{aligned}$$

where $g \equiv (M/\Omega)^2$ is the coupling constant and $\Gamma \equiv \Gamma_L + \Gamma_R$ the total escape rate. The spectral function and the transmission function are related via[1]

$$A(\omega) = \frac{\Gamma_L + \Gamma_R}{\Gamma_L \Gamma_R} T_{\mathrm{tot}}(\omega), \qquad (5.6)$$

which lead us to the exact SPA spectral function[2]

$$\begin{aligned} A_{\mathrm{SPA}}(\omega) &= \Gamma e^{-2g} \sum_{m=0}^{\infty} \frac{g^m}{m!} \qquad (5.7) \\ &\times \left| \sum_{j=0}^{m} (-1)^j \binom{m}{j} \sum_{l=0}^{\infty} \left(\frac{1}{\omega - (\varepsilon_0 - g\Omega) - (j+l)\Omega + i\Gamma/2} \right) \right|^2. \end{aligned}$$

---

[1] This connection naturally comes about from the Fisher-Lee relations [32, 63].

[2] The SPA result resembles a generalization of the independent boson model for Einstein phonons [40]. In this simpler model the electron-phonon interaction is considered to couple to an isolated electron state, i.e. a state which is not broadened at all. This situation can be solved exactly by various techniques and leads to an interacting electronic spectral function which is a series of δ-functions with weights given by a Poisson distribution,

$$A(\omega) = 2\pi e^{-g} \sum_{m=0}^{\infty} \frac{g^m}{m!} \delta(\omega - (\varepsilon_0 - g\Omega) - m\Omega).$$

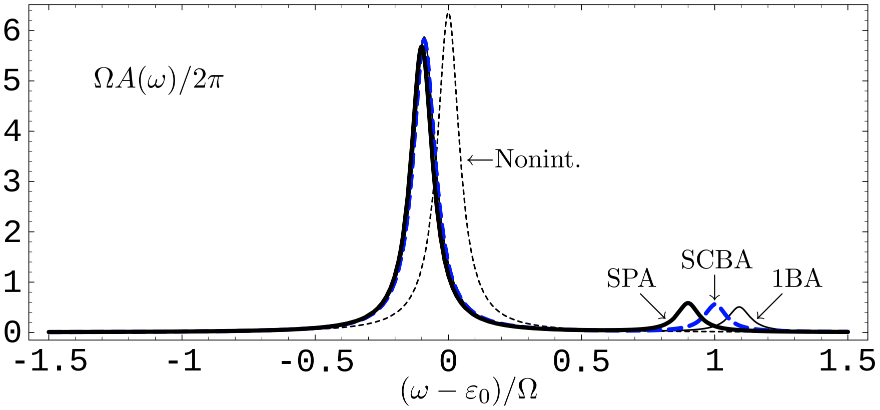

Figure 5.2: *Comparison of the perturbative results 1BA and SCBA (for very low temperatures $k_B T = 0.001\Omega$) with the exact single particle limit (strictly zero temperature). The full thin line is 1BA, the blue dashed is SCBA, the black thick line is the exact SPA result, and the thin dotted line is noninteracting case. It is seen that the phonon satellite peaks for 1BA and SCBA are positioned slightly away from the exact one.*

This result for the spectral function is shown in Fig. 5.2 for specific parameters as stated in the column denoted by WBL-SPA in Tab. 5.1. In the same figure we also plot the spectral functions found via 1BA and SCBA as well as the noninteracting one.

One observes that the spectral function develops a phonon sideband roughly displaced by the phonon mode energy Ω from the main peak. Also, the electron-phonon coupling shifts the main peak towards lower energies. This is called a polaronic shift since the electronic state is dressed by a polarization of the surrounding medium via the phonon interaction (the phonon mode represents to ionic oscillation). Besides these common features one notices that whereas the main peaks of 1BA and SCBA seem to agree quite nicely with the exact one the phonon satellites are incorrectly positioned. As one iterates the Green's functions towards self-consistency the satellite moves to lower energies and finally settles at the position Ω away from the *unperturbed* peak. The exact result is that the satellite should be Ω away from the *renormalized* main peak. These deviations of the SCBA from exact results were also observed by Král [65] who argued that these were related to neglect of crossed diagrams, i.e. higher order self-energy diagrams. The inadequacies of the SCBA for the detailed spectral features have also been addressed by Stauber *et al.* [66].

The phonon satellites can be understood in the following way: An incoming electron with energy around $\varepsilon_0 + m\Omega$ can emit m phonons and thereby become resonant with the localized level. This causes a sideband for phonon-assisted tunneling events above ε_0 in the transmission probability. The satellites thus relate to *in-scattering* processes because the level is initially empty in SPA. Since we are at zero temperature the incoming electron cannot absorb phonons. Thus, if the temperature is finite one would

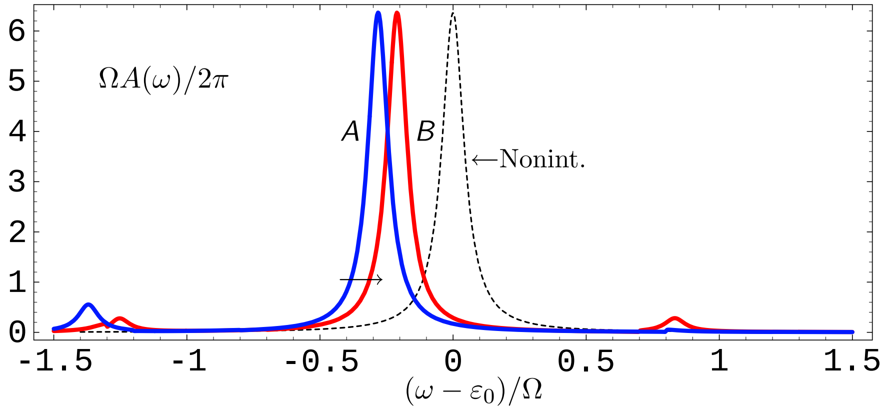

Figure 5.3: *Spectral function in the WBL with finite filling. As the bias voltage is swept one observes a crossover between two characteristic regimes A and B corresponding to a filled or a half-filled level. The blue curve belongs to regime A ($eV = 0.4\Omega$) and the red curve to regime B ($eV = 0.6\Omega$). The arrow indicates the crossover from A to B as the bias voltage is increased. The black dotted line is the noninteracting spectral function plotted for reference.*

also find sidebands below ε_0.

We end by noting that the numerical spectral functions fulfill the sum rule

$$\int_{-4\Omega}^{4\Omega} \frac{\mathrm{d}\omega}{2\pi} A_0(\omega) \approx \int_{-4\Omega}^{4\Omega} \frac{\mathrm{d}\omega}{2\pi} A_{1\mathrm{BA}}(\omega) \approx \int_{-4\Omega}^{4\Omega} \frac{\mathrm{d}\omega}{2\pi} A_{\mathrm{SCBA}}(\omega) \approx 0.992 \ . \qquad (5.8)$$

5.2.2 Finite filling

When we consider the presence of a Fermi sea there are no longer analytical results available. Instead we choose to compare our method with results reported by Hyldgaard *et al.* [52] who studied this kind of models. Let us in particular focus on a system where the resonant level coincides with the (equilibrium) chemical potential μ.

First, we study how the spectral function behaves under various bias conditions. Here we take the bias voltage to be applied symmetrically, i.e. $\mu_{L(R)} = \mu + (-)eV/2$. All parameters used in this calculation can be found in Tab. 5.1. The results are shown in Fig. 5.3. The observed trend is clear: One finds that the shape of spectral function more or less has two characteristic forms; the blue curve in the plot is representative in the bias range $0.0 \leq eV \lesssim 0.4\Omega$ while the red curve in the range $eV \gtrsim 0.6\Omega$. We denote these two regimes A and B respectively. In between these one observes a rather sudden crossover which corresponds to the change from the level being almost completely filled to being exactly half-filled.

The overall shift of the main peak is directly – but not exclusively – related to the Hartree-diagram which effectively lowers the bare level by an amount proportional to the electron occupation. The shift expresses that the indirect Frölich electron-electron interaction is an attractive one because

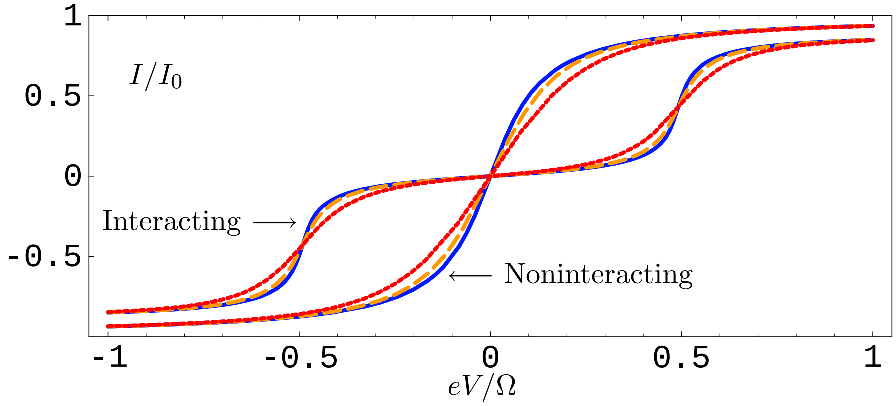

Figure 5.4: *I–V characteristics in the WBL. The current is scaled by the saturation value $I_0 = 2\Gamma_L\Gamma_R/(\Gamma_L+\Gamma_R)$. The different curves correspond to the temperatures $k_BT = 0.001\Omega$ (full blue), $k_BT = 0.020\Omega$ (dashed orange), and $k_BT = 0.040\Omega$ (dotted red).*

the level energy is lowered. This behavior was also observed by Hyldgaard *et al.* [52].

The full I–V characteristic of the system in WBL is shown in Fig. 5.4 for a range of low temperatures. Both the noninteracting as well as the interacting results are plotted. Their very different shapes are predominantly due to the polaronic shift. In the noninteracting case the system is resonantly aligned in equilibrium whereas for the interacting case the resonant condition is obtained at a finite bias voltage.

The same calculations are also presented in terms of differential conductance in Fig. 5.5. Two observations are worth mentioning: First, the effect of increasing the temperature is effectively a smearing of the conductance peaks. At sufficiently low temperatures we find that the noninteracting zero-bias conductance is exactly the quantum unit $G_0 = 2e^2/h$ which is expected since the system is precisely on resonance. In the interacting case we note that the differential conductance becomes larger than the quantum unit. This is an artifact of the combined effect of resonant transport and drift of the resonant level with bias (crossover from regime A to B). Second, in the inset of the interacting plot we observe additional fine structure due to resonant transmission processes via the phonon sidebands.

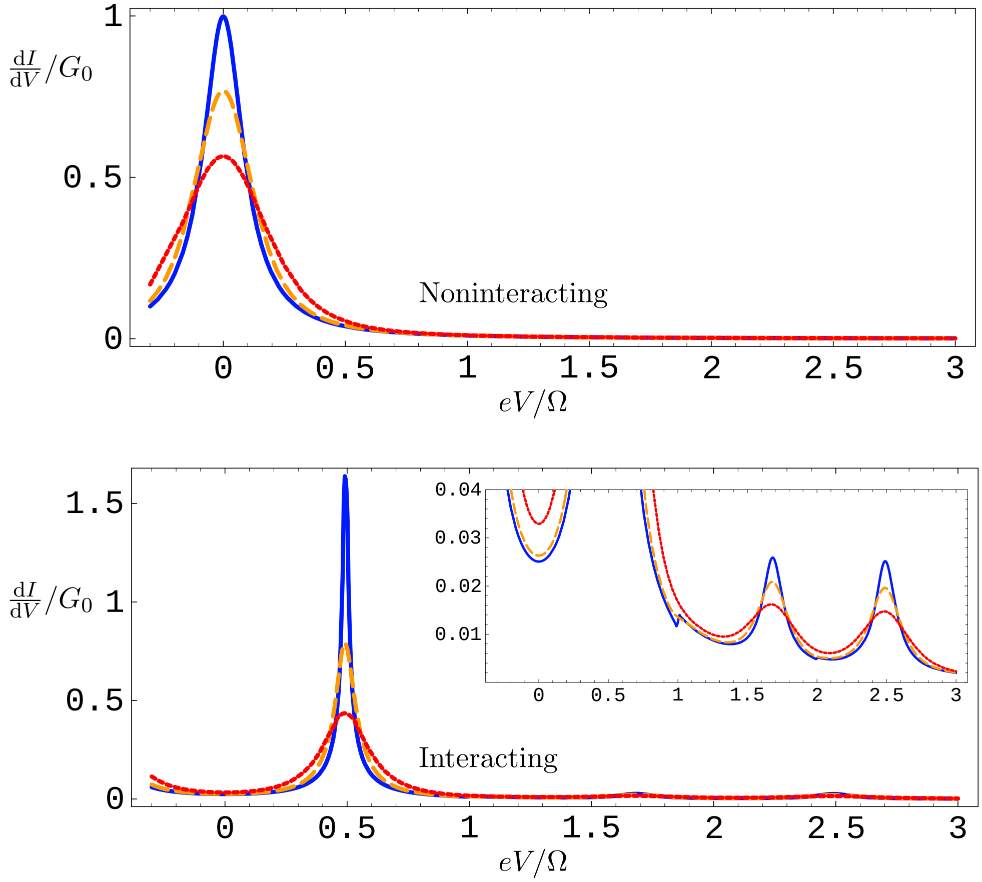

Figure 5.5: *Differential conductance in the WBL where the upper (lower) plot is for the noninteracting (interacting) situation. The different curves correspond to* $k_BT = 0.001\Omega$ *(full blue),* $k_BT = 0.020\Omega$ *(dashed orange), and* $k_BT = 0.040\Omega$ *(dotted red). The inset shows the fine conductance peaks related to the phonon sidebands.*

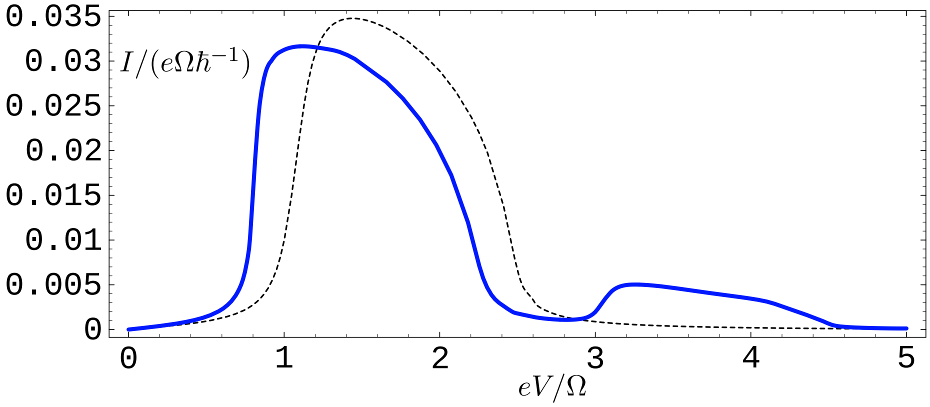

Figure 5.6: *Electrical current of a RTD modelled with finite band-widths of the leads. The full blue line (dashed black) is the interacting (noninteracting) calculation. Both characteristics show NDR. In the valley region one observes that the electron-phonon interaction gives rise to a secondary current peak. This calculation agrees quantitatively with Hyldgaard et al. [52].*

5.3 Finite band-widths and negative differential resistance

The I–V characteristics calculated in the previous section missed one of the key features of a resonant tunneling diode (RTD) namely the negative differential resistance (NDR) which is an effect related to finite band-widths of the contacts [32, 37, 67, 68]. Standard realizations of RTDs comprise single quantum wells fabricated as layered structures on n-doped wafers of GaAs with barriers formed by GaAlAs. In order to model the shallow Fermi seas and the relatively narrow band-width in semiconducting conduction bands we follow Hyldgaard *et al.* [52] and take them to be described by simple semi-infinite one-dimensional tight-binding chains.

As shown in Appendix C the appropriate escape rates $\Gamma_{L/R}(\omega)$ within this model for the leads are functions with semi-elliptic shapes

$$\Gamma_{L/R}(\omega) \;=\; \Gamma_{L/R}\theta(1-|x|)(1-x^2), \qquad x = \frac{\omega-(\phi+W/2)}{W/2}, \tag{5.9}$$

where W specifies the band-width and ϕ the position of the lower band edge. For simplicity we take $\Delta(\omega) = 0$.

We choose equivalent parameters as those employed by Hyldgaard *et al.* These are listed in Tab. 5.1 in the last column. The complete I–V characteristic is shown in Fig. 5.6, which quantitatively agrees with Hyldgaard *et al.* (Fig. 7 in [52]). The device calculation clearly exhibits NDR both with and without electron-phonon interaction. The main effect of the interaction is in valley region where one observes a secondary current peak. This kind of additional structures related to optical phonons are also observed experimentally [69].

One can understand the qualitative features of the calculation from the

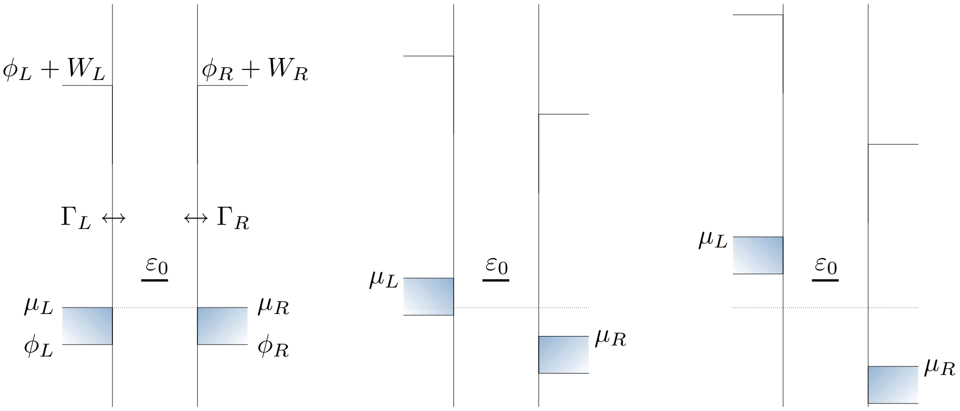

Figure 5.7: *Schematics of resonant tunneling through a single localized level. The electrodes have a finite band-width and shallow Fermi seas. The system is sketched for three different bias conditions. To the left the system is in equilibrium and the (identical) leads are aligned. In the central figure a bias voltage has been applied symmetrically with respect to the equilibrium chemical potential in such a way that the left electrode becomes resonant with the localized level. To the right the bias has been increased even further such that the left band falls above the level* ε_0 *which leads to a decrease of the current (valley region).*

schematics shown in Fig. 5.7. The localized level is considered to be positioned well above the Fermi level and the bias voltage to be applied symmetrically across the device. For a small voltage one will only observe tiny currents flowing. But when the chemical potential in the left electrode aligns with the localized state a large resonant current is activated. When the bias increases further the current starts to fall off as the lower band edge of the left electrode passes the localized level. In this situation a resonant current will only sustain if the electrons can emit phonons. The secondary current peak in the interacting I–V characteristic exactly corresponds to such inelastic processes.

5.4 Conclusions

In this section we demonstrated how the developed numerical routine reproduces various results from the literature on resonant tunneling in semiconductor double-barrier structures. In particular we considered the features of the single-level spectral function. It was found that the electron-phonon interaction gave rise to phonon sidebands as well as a polaronic shift of the main peak. Compared with an exact result in the single particle limit we observed that the phonon satellites in the 1BA/SCBA were not exactly located at their correct positions. We also repeated a calculation by Hyldgaard *et al.* on a full I–V characteristic of a resonant tunneling diode. The model showed both NDR and a phonon-induced secondary current peak.

Chapter 6

Comparison with exact diagonalization method

6.1 Introduction

In Chap. 5 we discussed the electron-phonon interaction in relation to resonant tunneling through a single localized state. It was found that the interaction gave rise to both an overall shift of the level and to satellite peaks in the spectral function. We compared our perturbative approach with an exact result and found that the main peak was quite accurately described while the position of phonon induced satellites were slightly off the correct place.

The conclusions mentioned above concerned a single level in the single particle limit only. Since we in this thesis are interested in more general systems consisting of several electronic states under finite filling conditions a number of questions arises: How accurate are the first Born approximation (1BA) as well as the self-consistent Born approximation (SCBA) generally? How are eventual phonon sidebands located in these approximations? What is the nature of the excitations made possible by the phonon interaction?

In order to address such questions and to gain some understanding for the spectral function for systems of several electronic levels this chapter is devoted a study of exact diagonalization of an isolated 3-level system that interacts with a single longitudinal optical phonon mode. This will allow us to put both 1BA and SCBA to test under general conditions.

One possible approach to a many-particle problem is to attempt to solve it by numerically exact diagonalization of the full Hamiltonian. The major disadvantage of this is that only relatively simple problems can be handled on today's computers since the computational load scales poorly with the dimensionality of the Fock-space. For instance, with N spin-degenerate fermionic states the full Fock-space has dimension 4^N since each individual state can be either empty or singly/doubly occupied according to the Pauli principle. With $N = 10$ a matrix representation of the full Hamiltonian will contain $\sim 10^{12}$ elements; obviously one thus needs to think twice before attempting a simpleminded diagonalization.

The strategy we want to employ here to solve a 3-level problem with electron-phonon interaction is to assign matrix representations to the second quantized annihilation and creation operators which then allows for constructing the full Hamiltonian by matrix multiplications. A general description of how this can be done is found in Appendix D. One immediately faces the problem that boson operators are represented by semi-infinite matrices since their occupation is unbound. In order handle the problem numerically we are forced to introduce the approximation related to a truncation of the boson space.

After a presentation of the Hamiltonian we set out by examining single particle excitations in the 3-level system containing $N = 3$ electrons at zero temperature. The analysis allows for establishing the numerically exact spectral function. In relation to this result we finally discuss the spectral functions found for a similar system via 1BA and SCBA in the limit of very weak coupling to electrodes.

6.2 Isolated 3-level tight-binding model

We take an isolated 3-level electronic system interacting with a single phonon mode to be described by the usual Frölich Hamiltonian

$$\mathscr{H} = \mathscr{H}_{\text{el}} + \mathscr{H}_{\text{e-ph}} + \mathscr{H}_{\text{ph}}, \tag{6.1a}$$

$$\mathscr{H}_{\text{el}} = \sum_{i,j=1}^{3} \sum_{\sigma} c_{i\sigma}^{\dagger} \mathbf{H}_{ij} c_{j\sigma}, \tag{6.1b}$$

$$\mathscr{H}_{\text{e-ph}} = \sum_{i,j=1}^{3} \sum_{\sigma} c_{i\sigma}^{\dagger} \mathbf{M}_{ij} c_{j\sigma} (b^{\dagger} + b), \tag{6.1c}$$

$$\mathscr{H}_{\text{ph}} = \Omega\Big(b^{\dagger} b + \frac{1}{2}\Big), \tag{6.1d}$$

where $\mathscr{H}_{\text{el}}$ describes the unperturbed electrons, $\mathscr{H}_{\text{e-ph}}$ the electron-phonon interaction, and $\mathscr{H}_{\text{ph}}$ the single harmonic oscillator. In particular we shall consider the system to be a degenerate 3-site tight-binding chain in which the central site is allowed to oscillate along the direction of the chain. We therefore take the parameters to be given in a real-space representation by

$$\mathbf{H} = \begin{pmatrix} \varepsilon_0 & -t_0 & 0 \\ -t_0 & \varepsilon_0 & -t_0 \\ 0 & -t_0 & \varepsilon_0 \end{pmatrix}, \qquad \mathbf{M} = \begin{pmatrix} 0 & m & 0 \\ m & 0 & -m \\ 0 & -m & 0 \end{pmatrix}, \tag{6.2}$$

where ε_0 is the on-site energy, t_0 the hopping parameter, and m the modulation of the hopping by small displacements (to linear order). By taking the diagonal elements of $\mathbf{M}$ to be zero we ignore the static self-screening, i.e. polaronic shifts of the bare levels.

Equivalently we can represent the system in the basis where $\mathbf{H}$ is diagonal,

$$\begin{aligned}\widetilde{\mathbf{H}} &= \mathbf{R}^\dagger \mathbf{H}\mathbf{R} = \begin{pmatrix} \varepsilon_+ & 0 & 0 \\ 0 & \varepsilon_0 & 0 \\ 0 & 0 & \varepsilon_- \end{pmatrix} = \begin{pmatrix} \varepsilon_0 + \sqrt{2}t_0 & 0 & 0 \\ 0 & \varepsilon_0 & 0 \\ 0 & 0 & \varepsilon_0 - \sqrt{2}t_0 \end{pmatrix}, \quad (6.3\text{a}) \\ \widetilde{\mathbf{M}} &= \mathbf{R}^\dagger \mathbf{M}\mathbf{R} = \begin{pmatrix} 0 & m & 0 \\ m & 0 & -m \\ 0 & -m & 0 \end{pmatrix}, \quad (6.3\text{b})\end{aligned}$$

with

$$\mathbf{R} = \frac{1}{2}\begin{pmatrix} 1 & -\sqrt{2} & 1 \\ -\sqrt{2} & 0 & \sqrt{2} \\ 1 & \sqrt{2} & 1 \end{pmatrix}, \quad (6.4)$$

defining the transformation. We thus see that in the energy eigenbasis we have the usual bonding, non-bonding, and antibonding states with energies ε_-, ε_0, and ε_+, respectively. We also notice that $\widetilde{\mathbf{M}}$ couples *between* the energy states similarly as $\mathbf{M}$ coupled between neighboring sites. For simplicity we take $\varepsilon_0 = 0$ below.

6.3 The spectral function

We now want to determine the spectral function for the interacting system described above. Let us begin by considering the single-particle zero-temperature retarded Green's function $G^r_{i\sigma,j\sigma'}(t,t')$ defined as [39]

$$G^r_{i\sigma,j\sigma'}(t,t') = -i\hbar^{-1}\theta(t-t')\langle \mathrm{GS}|\{c_{i\sigma}(t), c^\dagger_{j\sigma'}(t')\}|\mathrm{GS}\rangle, \quad (6.5)$$

with operators expressed in the Heisenberg picture and $|\mathrm{GS}\rangle$ being the ground state of the interacting system. When the Hamiltonian $\mathscr{H}$, the fermion number operator $\mathscr{N}$, and the total spin operator $\mathscr{S}_z$ commute they possess a common set of orthonormal eigenfunctions $\{|\Psi_n\rangle\}$ that fulfill the eigenvalue equations

$$\begin{aligned}\mathscr{H}|\Psi_n\rangle &= E_n|\Psi_n\rangle, \quad (6.6\text{a}) \\ \mathscr{N}|\Psi_n\rangle &= N|\Psi_n\rangle, \quad (6.6\text{b}) \\ \mathscr{S}_z|\Psi_n\rangle &= S_z|\Psi_n\rangle, \quad (6.6\text{c})\end{aligned}$$

and obey the completeness relation

$$\sum_n |\Psi_n\rangle\langle\Psi_n| = 1. \quad (6.7)$$

Inserting the complete set into the retarded Green's function we find

$$\begin{aligned}i\hbar G^r_{i\sigma,j\sigma'}(t,0) &= \theta(t)\langle \mathrm{GS}|e^{i\mathscr{H}t/\hbar}c_{i\sigma}e^{-i\mathscr{H}t/\hbar}c^\dagger_{j\sigma'} + c^\dagger_{j\sigma'}e^{i\mathscr{H}t/\hbar}c_{i\sigma}e^{-i\mathscr{H}t/\hbar}|\mathrm{GS}\rangle \\ &= \theta(t)\sum_n \Big[e^{-i(E_n-E_{GS})t/\hbar}\langle \mathrm{GS}|c_{i\sigma}|\Psi_n\rangle\langle\Psi_n|c^\dagger_{j\sigma'}|\mathrm{GS}\rangle \\ &\qquad + e^{i(E_n-E_{GS})t/\hbar}\langle \mathrm{GS}|c^\dagger_{j\sigma'}|\Psi_n\rangle\langle\Psi_n|c_{i\sigma}|\mathrm{GS}\rangle\Big], \quad (6.8)\end{aligned}$$

which has the Fourier transform

$$G^r_{i\sigma,j\sigma'}(\omega) \; = \; \sum_n \left[\frac{\langle \mathrm{GS}|c_{i\sigma}|\Psi_n\rangle\langle\Psi_n|c^\dagger_{j\sigma'}|\mathrm{GS}\rangle}{\omega - E_n + E_{GS} + i\eta} + \frac{\langle \mathrm{GS}|c^\dagger_{j\sigma'}|\Psi_n\rangle\langle\Psi_n|c_{i\sigma}|\mathrm{GS}\rangle}{\omega + E_n - E_{GS} + i\eta} \right]. \tag{6.9}$$

Of particular interest is the trace of the spectral function $A(\omega)$ defined as

$$\begin{aligned} A(\omega) \; &\equiv \; \mathrm{Tr}[\mathbf{A}_{i\sigma,j\sigma'}(\omega)] \\ &= \; -2\sum_{i\sigma} \Im\mathrm{m}[G^r_{i\sigma,i\sigma}(\omega)] \\ &= \; 2\pi \sum_{i\sigma}\sum_n \left[|\langle\Psi_n|c^\dagger_{i\sigma}|\mathrm{GS}\rangle|^2 \delta(\omega - E^P_n) + |\langle\Psi_n|c_{i\sigma}|\mathrm{GS}\rangle|^2\delta(\omega - E^H_n) \right], \end{aligned} \tag{6.10}$$

where we have introduced the excitation energies of particles $E^P_n \equiv E_n - E_{GS}$ and of holes $E^H_n \equiv -E_n + E_{GS}$. For a given energy ω the total spectral function $A(\omega)$ thus expresses the ability of the system to absorb both particles and holes. Because both possibilities are included in this way the quantity maps out dynamical properties of the system without considering which particular states that are occupied with particles. The interacting spectral function may though indirectly depend on the filling, cf. Chap. 4.

6.4 Numerical calculations

In order to numerically evaluate the total spectral function Eq. (6.10) we need to decide on a ground state $|GS\rangle$ for the system. From now on we therefore choose it to be the unique one with $N = 3$ electrons and total spin up $S_z = 1/2$, i.e. a half-filled system.

The diagonalization technique has been implemented in MATHEMATICA. According to Appendix D we assign matrix representations to the fermion creation and annihilation operators and truncate the boson space appropriately. As examined below in Sec. 6.4.3 it is, for the parameters considered here, very accurate just to keep only the phonon states $\{|0\rangle, |1\rangle, |2\rangle\, |3\rangle\}$.

With these operator representations at hand we can also build matrix representations for the Hamiltonian $\mathscr{H}$, the number operator $\mathscr{N}$, and the total spin component operator $\mathscr{S}_z$. Among the common eigenvectors with eigenvalues $N = 3$ and $S_z = 1/2$ the ground state can then be picked out as the one which has the lowest energy.

6.4.1 Noninteracting case

The ground state in the noninteracting case is simply

$$|GS^{N=3}\rangle_0 \; = \tag{6.11}$$

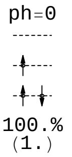

,

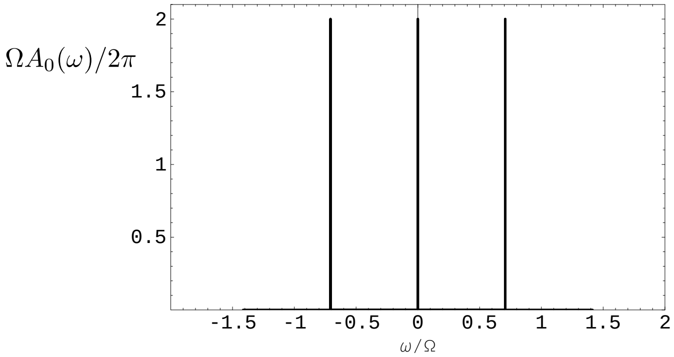

Figure 6.1: *Spectral function $A_0(\omega)$ for the noninteracting case $m = 0.0\Omega$ and $t_0 = 0.5\Omega$. The delta functions are represented by columns with heights corresponding to the sum of all weights.*

where we have introduced a schematic representation of a particular state – here the noninteracting ground state – in terms of the noninteracting basis states. The three dotted lines indicate the electronic levels (upper is ε_+, middle is ε_0, and lower is ε_-) and an arrow the occupation of such a level by a particle with either spin up or spin down. The number of phonons is represented by a number "`ph`" above the figure, and the state resolved "probability" (in percent) as well as the corresponding amplitude (in parenthesis) are found below.[1]

Having a ground state with $N = 3$ particles, the only eigenvectors that contribute to the spectral function in Eq. (6.10) are those that belong to subspaces of $N = 3 \pm 1$ particles and total spin $S_z = 1/2 \pm 1/2$. Projecting the full Hamiltonian onto each of these subspaces it is a simple task to find the eigenvectors[2] and thus for each eigenvector to calculate the matrix element and corresponding excitation energy as of Eq. (6.10). The spectral function $A_0(\omega)$ for the noninteracting case $m = 0.0\Omega$ and $t_0 = 0.5\Omega$ is shown in Fig. 6.1. The excitation energies correspond exactly to the electronic level energies $\varepsilon_+, \varepsilon_0$, and ε_-, and the calculated spectral function fulfills the sum rule,

$$\int_{-\infty}^{\infty} \frac{\mathrm{d}\omega}{2\pi} A_0(\omega) = 6. \tag{6.12}$$

Let us take a closer look at the peak at $\omega = \varepsilon_- \simeq -0.7071\Omega$. Among the eigenvectors in the subspace of $N = 2$ and $S_z = 1/2 \pm 1/2$ there are three that correspond to this excitation energy. They have the representations,

---

[1] Resolving a state $|\Psi\rangle$, the "amplitude" is the overlap $\langle\phi_\nu|\Psi\rangle$ ($|\phi_\nu\rangle$ being a noninteracting basis vector), and the "probability" just its absolute square $|\langle\phi_\nu|\Psi\rangle|^2$.

[2] We use the `Eigenvectors` and `GramSchmidt` methods in MATHEMATICA.

weights and energies[3]

$$|\Psi_4^{N=2}\rangle_0 =$$

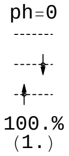

$$, \tag{6.13a}$$

$$\sum_{i\sigma} |\langle\Psi_4|c_{i\sigma}|GS\rangle_0|^2 = 0, \qquad E_{GS} - \langle\Psi_4|H|\Psi_4\rangle_0 = -0.7071\Omega \ ,$$

$$|\Psi_5^{N=2}\rangle_0 =$$

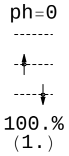

$$, \tag{6.13b}$$

$$\sum_{i\sigma} |\langle\Psi_5|c_{i\sigma}|GS\rangle_0|^2 = 1, \qquad E_{GS} - \langle\Psi_5|H|\Psi_5\rangle_0 = -0.7071\Omega \ ,$$

$$|\Psi_6^{N=2}\rangle_0 =$$

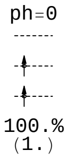

$$, \tag{6.13c}$$

$$\sum_{i\sigma} |\langle\Psi_5|c_{i\sigma}|GS\rangle_0|^2 = 1, \qquad E_{GS} - \langle\Psi_6|H|\Psi_6\rangle_0 = -0.7071\Omega \ .$$

From the schematic representation it is clear that the state named $|\Psi_4\rangle_0$ has zero overlap with the state $c_{i\sigma}|\mathrm{GS}\rangle_0$ because annihilating a particle from the ground state never leaves a spin-$\uparrow$ particle in the nonbonding state with energy ε_0. Along similar reasoning it is also clear why the two others have overlap one with the ground state.

Considering particle creation one finds among the eigenvectors in the subspace of $N = 4$ and $S_z = 1/2 \pm 1/2$ that there are actually none corresponding to energy $\omega = \varepsilon_-$. This is so because the ground state has ε_- doubly occupied and it is only possible to inject holes.

Repeating the analysis on the other two peaks we are lead to conclude that at $\omega = \varepsilon_0$ one can inject both particles with spin-$\downarrow$ and holes with spin-$\uparrow$, and at $\omega = \varepsilon_+$ one can inject only particles of either spin.

6.4.2 Interacting case

Let us now consider the corresponding ground state for the interacting case $m = 0.2\Omega$ and $t_0 = 0.5\Omega$. The easiest way to determine $|GS\rangle$ is to project the full Hamiltonian onto the subspace of $N = 3$ particles and of total spin $S_z = 1/2$ and then pick out the eigenvector with the lowest energy. By doing

---

[3] The eigenvectors are labelled by an arbitrary index number originating from MATHEMATICA.

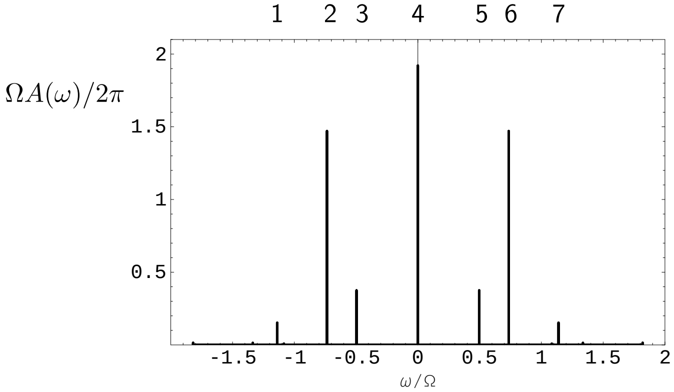

Figure 6.2: *Spectral function $A(\omega)$ for the interacting case $m = 0.2\Omega$ and $t_0 = 0.5\Omega$. The delta functions are represented by columns with heights corresponding to the sum of all weights. The seven most important peaks have been labelled 1-7.*

so there is no need for finding the complete common set of eigenvectors. The ground state is found to have a representation

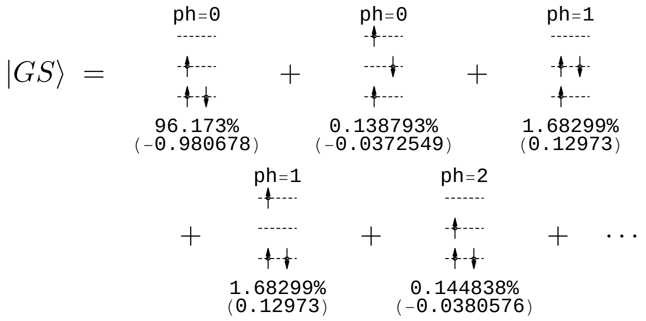

(6.14)

We see that the interacting ground state is "almost" as the noninteracting one but with a little mixture of states including one phonon.

With the ground state at hand we find the eigenvectors of the Hamiltonian belonging to the subspaces $N = 3 \pm 1$ particles and total spin $S_z = 1/2 \pm 1/2$ and calculate the matrix elements and the corresponding excitation energies to determine the spectral function $A(\omega)$. This is shown in Fig. 6.2. The vibrational interaction is seen to induce new peaks in the excitation spectrum. The noninteracting peaks persist to a certain extent but their weights are lowered and positions slightly shifted. Also the interacting spectral function fulfills the sum rule,

$$\int_{-\infty}^{\infty} \frac{\mathrm{d}\omega}{2\pi} A(\omega) = 6. \tag{6.15}$$

Let us first analyze peak 2 around $\omega \approx -0.74$. Among the eigenvectors of the Hamiltonian in the subspaces of $N = 2$ and $S_z = 1/2 \pm 1/2$ there are two important contributions,

$|\Psi_{36}^{N=2}\rangle =$

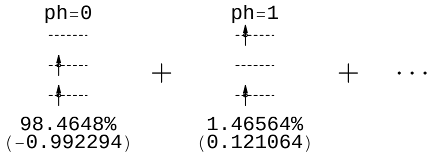

(6.16a)

$$\sum_{i\sigma} |\langle\Psi_{36}|c_{i\sigma}|GS\rangle|^2 = 0.980368 \ , \qquad E_{GS} - \langle\Psi_{36}|H|\Psi_{36}\rangle = -0.7356\Omega \ ,$$

$|\Psi_{37}^{N=2}\rangle =$

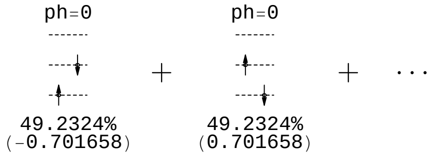

(6.16b)

$$\sum_{i\sigma} |\langle\Psi_{37}|c_{i\sigma}|GS\rangle|^2 = 0.490184 \ , \qquad E_{GS} - \langle\Psi_{37}|H|\Psi_{37}\rangle = -0.7356\Omega \ .$$

The schematic representations of these states show very little phonon character and peak 2 is therefore expected not to be much affected by the electron-phonon interaction. This conclusion nicely agrees with the fact that almost the same excitation energy was also contained in the noninteracting spectral function, cf. Fig. 6.1.

The situation is quite different if one looks at the new peaks that arise in the interacting case. For peak 3 around $\omega \approx -0.5\Omega$, we have only one important energy eigenvector,

$|\Psi_{31}^{N=2}\rangle =$

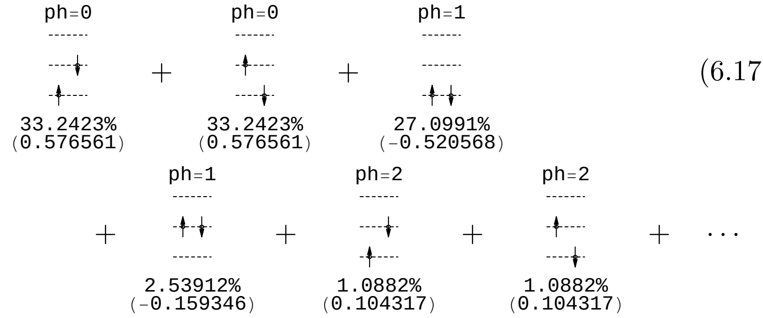

(6.17)

$$\sum_{i\sigma} |\langle\Psi_{31}|c_{i\sigma}|GS\rangle|^2 = 0.374903 \ , \qquad E_{GS} - \langle\Psi_{31}|H|\Psi_{31}\rangle = -0.4965\Omega \ ,$$

which clearly has a phononic signature. From the schematic representation one understands why the energy is slightly larger than ε_-: The excitation energy of the two first basis vectors correspond to $\omega = -0.7071\Omega$ while the third to $\omega = -0.4142\Omega$ and all others to even higher energies. The weighted result must hence be a shift upwards.

For peak 1 around $\omega \approx -1.13\Omega$ there is one important energy eigenvec-

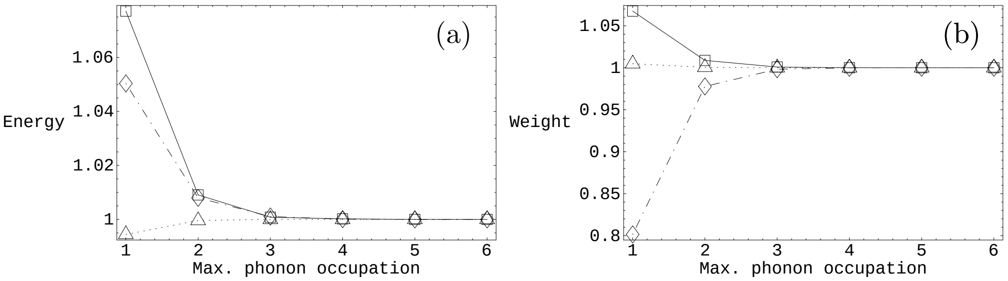

Figure 6.3: *Convergence of (a) scaled peak positions $E(N_{ph})/E(6)$ and (b) scaled peak weights $W(N_{ph})/W(6)$ with increasing number of phonon states included in the calculation for $m = 0.2\Omega$. The symbols denote $\diamond$ for peak 1, $\triangle$ for peak 2, and $\square$ for peak 3.*

tor,

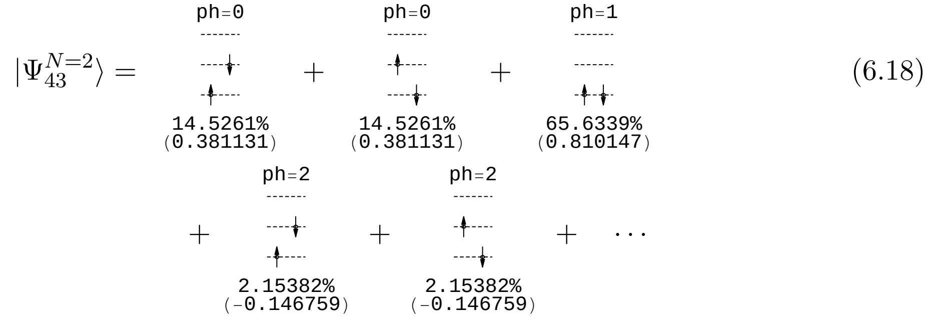

$$|\Psi_{43}^{N=2}\rangle = \overset{\text{ph=0}}{\underset{\substack{14.5261\% \\ (0.381131)}}{\begin{smallmatrix} - \\ \downarrow \\ \uparrow \end{smallmatrix}}} + \overset{\text{ph=0}}{\underset{\substack{14.5261\% \\ (0.381131)}}{\begin{smallmatrix} - \\ \uparrow \\ \downarrow \end{smallmatrix}}} + \overset{\text{ph=1}}{\underset{\substack{65.6339\% \\ (0.810147)}}{\begin{smallmatrix} - \\ - \\ \uparrow\downarrow \end{smallmatrix}}} \tag{6.18}$$

$$+ \overset{\text{ph=2}}{\underset{\substack{2.15382\% \\ (-0.146759)}}{\begin{smallmatrix} - \\ \downarrow \\ \uparrow \end{smallmatrix}}} + \overset{\text{ph=2}}{\underset{\substack{2.15382\% \\ (-0.146759)}}{\begin{smallmatrix} - \\ \uparrow \\ \downarrow \end{smallmatrix}}} + \cdots$$

$$\sum_{i\sigma} |\langle \Psi_{43} | c_{i\sigma} | GS \rangle|^2 = 0.152712 \; , \qquad E_{GS} - \langle \Psi_{43} | H | \Psi_{43} \rangle = -1.1386\Omega \; .$$

We see that this eigenstate is largely dominated by a single state with one phonon. For this reason one can interpret excitation 1 as a hole formation accompanied by creation of a virtual phonon.

Similarly one can understand the peaks 5-7 in terms of particle excitations, i.e. to excitations involving the creation of particles in the system.

6.4.3 Convergence

In order to have a numerically correct description of the system one needs to make sure that the artificial truncation of the boson space does not affect the results. To check this we have picked out the three peaks 1-3 for $m = 0.2\Omega$, and studied how their position and weights change with the maximum number of phonons included. The results are shown in Fig. 6.3. The difference between including 5 or 6 phonons was found to be absolutely negligible for our purposes, so we normalize the data with respect to the 6-phonon results, i.e. we plot scaled peak positions $E(N_{\rm ph})/E(6)$ and scaled peak weights $W(N_{\rm ph})/W(6)$ for each peak.

The figure illustrates that by including only phonon states $\{|0\rangle, |1\rangle, |2\rangle\, |3\rangle\}$ the results are accurate within 1%. From this one expects that the descrip-

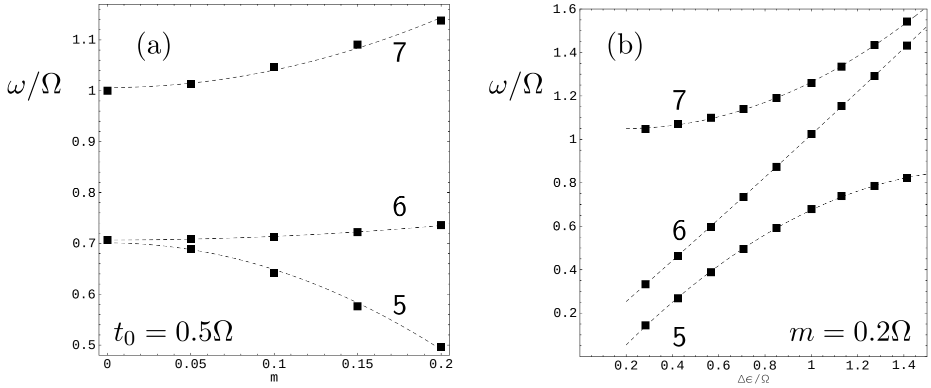

Figure 6.4: *Position of the peaks* 5*-*7 *(a) for various interaction strengths* m *with best fits of the form* $c_1x^2 + c_2$ *and (b) for different level spacings* $\Delta\varepsilon = \sqrt{2}t_0$ *with best fits of the form* $c_1x^2 + c_2x + c_3$*.*

tion will be even better if the interaction is weaker. In conclusion, all results presented in Sec. 6.4 (where $m \leq 0.2\Omega$) should be very accurate.

6.4.4 Interaction strength

We can now explore how the interaction strength changes the position of the peaks. In Fig. 6.4a the position of the peaks 5-7 are shown as the interaction strength m is varied between 0 and 0.2Ω. The dotted lines connecting the data points are the fits

$$\begin{aligned} 5: \quad \omega/\Omega &= 0.7010 - 5.2418(m/\Omega)^2, && (6.19a)\\ 6: \quad \omega/\Omega &= 0.7066 + 0.7113(m/\Omega)^2, && (6.19b)\\ 7: \quad \omega/\Omega &= 1.0063 + 3.4407(m/\Omega)^2. && (6.19c) \end{aligned}$$

The fits clearly show that the perturbation is roughly second order in m/Ω and that the position of peak 6 is not much affected by the interaction (as opposite to the two others 5 and 7).

6.4.5 Level spacing

We also want to examine how things are altered with different level spacings, or equivalently, with different hopping strengths t_0. In Fig. 6.4b the position of the peaks 5-7 are shown for various level spacings $\Delta\varepsilon = \sqrt{2}t_0$ and fixed interaction strength $m = 0.2\Omega$. The dotted lines are best fits

$$\begin{aligned} 5: \quad \omega/\Omega &= -0.1700 + 1.1882\Delta\varepsilon/\Omega - 0.3432(\Delta\varepsilon/\Omega)^2, && (6.20a)\\ 6: \quad \omega/\Omega &= 0.0670 + 0.9264\Delta\varepsilon/\Omega + 0.0284(\Delta\varepsilon/\Omega)^2, && (6.20b)\\ 7: \quad \omega/\Omega &= 1.0621 - 0.1276\Delta\varepsilon/\Omega + 0.3290(\Delta\varepsilon/\Omega)^2. && (6.20c) \end{aligned}$$

We see that peak 6 scales linearly with the level spacing $\Delta\varepsilon$ which is exactly what one expects for the antibonding state in the noninteracting case. Also

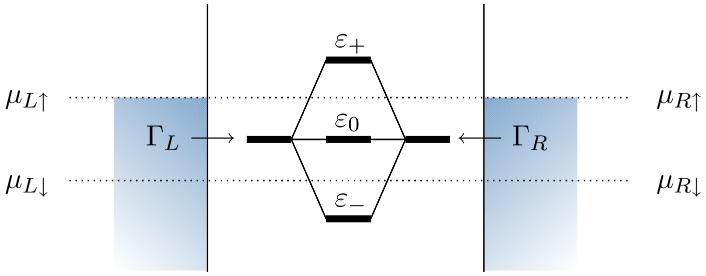

Figure 6.5: *The 3-level tight-binding chain placed in between two particle reservoirs. The 3 levels are shown both in real-space as well as in the energy basis. For a tiny but finite coupling of the system to the leads we can apply the NEGF method to determine the equilibrium spectral function $A(\omega)$ in 1BA and SCBA. In order to model the ground state of the completely isolated system we need to consider a spin-polarized filling as illustrated.*

it looks like that peak 5 (7) approaches $\omega = \Omega$ for $\Delta\varepsilon \to \infty$ ($\Delta\varepsilon \to 0$), i.e. that it is related to processes involving peak 4 (6) with one virtual phonon.

6.5 Calculations based on 1BA and SCBA

In the previous Sec. 6.4 we determined a numerically exact spectral function for the interacting system by diagonalization of the Hamiltonian, cf. Fig. 6.2. In this section we attempt a similar calculation using the perturbative methods of 1BA and SCBA.

First, our method based on Green's functions cannot numerically handle δ-functions as is appropriate for the isolated system. We thus need to introduce a tiny broadening which may be interpreted as an artificial coupling to particle reservoirs. Let us therefore think of the system to be in the usual transport setup where it is located in between two leads as illustrated in Fig. 6.5. For simplicity we model the leads in the wide-band limit (WBL) and consider only coupling of the end sites in the chain to either the left or right electrode, i.e. in a real-space representation we have

$$\mathbf{\Gamma}_L = \begin{pmatrix} \Gamma_L & 0 & 0 \\ 0 & 0 & 0 \\ 0 & 0 & 0 \end{pmatrix}, \qquad \mathbf{\Gamma}_R = \begin{pmatrix} 0 & 0 & 0 \\ 0 & 0 & 0 \\ 0 & 0 & \Gamma_R \end{pmatrix}, \tag{6.21}$$

In the limit $\Gamma_L = \Gamma_R \to 0$ we recover the completely isolated 3-level system. In the following we take the broadening to be significantly smaller than the typical energy scale of the problem and use $\Gamma_L = \Gamma_R = 10^{-2}\Omega$.

Secondly, we want to compare with the ground state chosen in Sec. 6.4 with $N = 3$ electrons and total spin $S_z = 1/2$, i.e. a half-filled system. In order to force an occupation of two particles with spin-$\uparrow$ and one with spin-$\downarrow$ we need to consider spin-polarized electrodes. Since the level broadening is

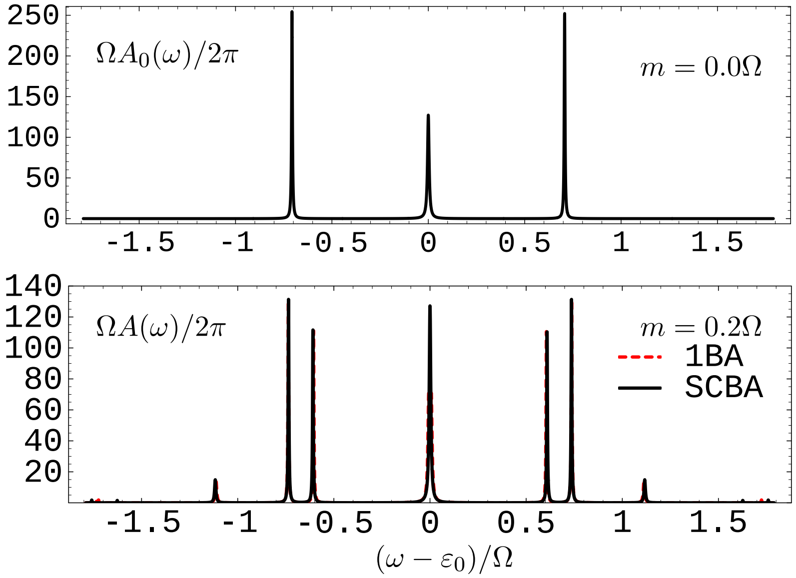

Figure 6.6: *Spectral function for the 3-level system very weakly coupled to spin-polarized electrodes. The upper plot is the noninteracting case while the lower one is for $m = 0.2\Omega$ in both 1BA and SCBA.*

much smaller than the level spacing we choose the (equilibrium) filling of spin-↑ (↓) particles $\mu_\uparrow$ ($\mu_\downarrow$) to be in between the antibonding (bonding) state and the nonbonding state as illustrated on Fig. 6.5.

Finally, we want to compare with a zero-temperature calculation. We therefore also take the thermal energy available to be much smaller than the typical energy scale of the problem and use $k_BT = 4 \cdot 10^{-4}\Omega$.

We are now in a position to apply the perturbative methods of 1BA and SCBA to calculate the equilibrium spectral functions. The results for both with and without electron-phonon interaction are shown in Fig. 6.6. We also plot the spin-resolved spectral functions in Fig. 6.7 which show that each peak corresponds to a particular spin orientation, i.e. the excitations have a spin-polarized nature.

The spectral functions fulfill the sum rule

$$\int_{-2\Omega}^{2\Omega} \frac{\mathrm{d}\omega}{2\pi} A_0(\omega) = \int_{-2\Omega}^{2\Omega} \frac{\mathrm{d}\omega}{2\pi} A_{1\mathrm{BA}}(\omega) = \int_{-2\Omega}^{2\Omega} \frac{\mathrm{d}\omega}{2\pi} A_{\mathrm{SCBA}}(\omega) = 5.999 \pm 0.001 \tag{6.22}$$

6.6 Comparison and conclusions

By comparison of Fig. 6.1 and 6.2 with Fig. 6.6 we see that the position of the peaks agree qualitatively. For a more quantitative comparison we have traced the position of the peaks 5-7 and their equivalent ones in 1BA/SCBA for various interaction strengths $0 \leq m \leq 0.2\Omega$. This is shown in Fig. 6.8.

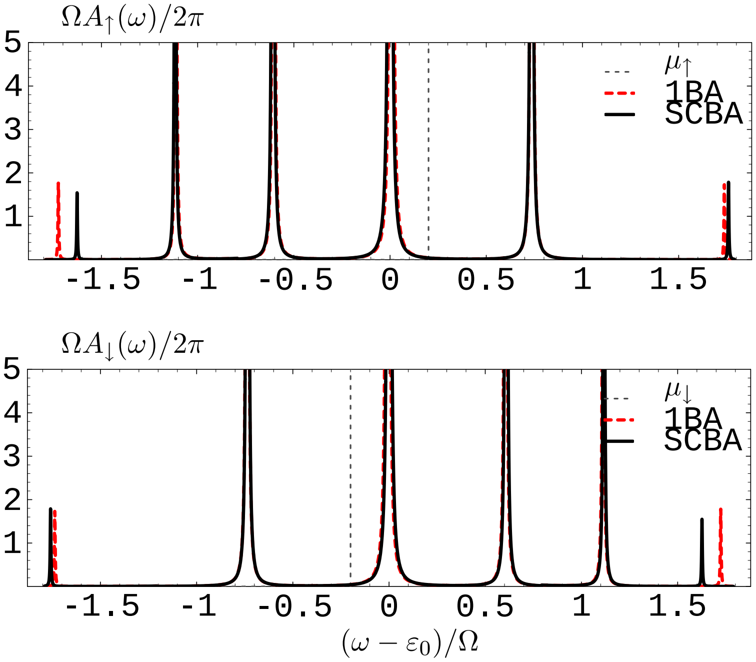

Figure 6.7: *Spin-resolved spectral functions for the 3-level system for* $m = 0.2\Omega$.

One observes that the two peaks 6 and 7 are relatively well described by 1BA/SCBA whereas peak 5 differs significantly between the two methods.

In conclusion, we have studied the features of the equilibrium spectral function for an isolated 3-level electronic system with phonon interaction using a numerically exact diagonalization technique. The results were compared with perturbative calculations within 1BA/SCBA for a similar, but thermodynamically open, system. This comparison yielded information about the accuracy of the 1BA/SCBA and showed that these approximations gave a fairly reasonable qualitative description for the particular system under consideration.

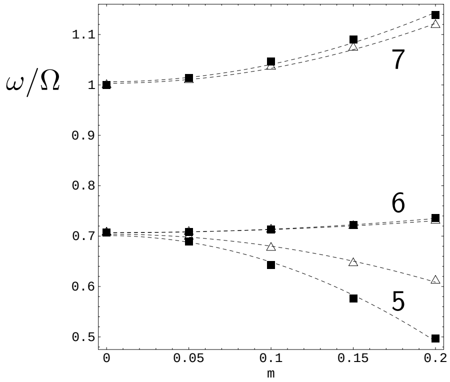

Figure 6.8: *Comparison of the peak positions within 1BA/SCBA (denoted by* $\triangle$*) to those found by exact diagonalization (*$\blacksquare$*).*

Chapter 7

Tight-binding model of inelastic transport in atomic wires

7.1 Introduction

In this chapter we want to apply our nonequilibrium Green's function (NEGF) method for inelastic transport to metallic atomic wires. In particular we have the experiments performed by Agraït *et al.* [28, 70] in our minds. As mentioned in Chap. 1 they measured the differential conductance of atomic gold wires at low temperatures ($4.2K$) using an STM. Their chains consisted of up to (around) seven atoms, a number which seems to be about the upper limit for stable configurations. The chains – especially the longer ones – were observed to display a characteristic conductance drop due to inelastic scattering of electrons presumably against a single phonon mode, cf. Fig. 1.5.

It is an intriguing question why only a single mode seems to be involved. Agraït *et al.* proposed that the Au wires essentially behave as infinite one-dimensional conductors where momentum is conserved, and, consequently, electrons can only excite longitudinal vibrations of the atomic chain whose wave number is twice the Fermi wave number k_F. This can be understood from Fig. 7.1 which illustrates the allowed inelastic transitions in a one-dimensional band. Thus, for the infinite chain only one longitudinal mode couples to the electrons and hence shows up in the conductance spectrum.

One might dispute that wires of up to (only) seven atoms behave as infinite chains in which phonons are free waves rather than (quasi-)localized vibrations. As mentioned in Chap. 2 momentum conservation in the electron-phonon interaction does not strictly holds for systems lacking translational invariance so electrons are generally able to interact with phonons of different wavelengths.

From a theoretical point of view it is a challenge to determine the actual modes of vibration and their influence on the current. One such approach

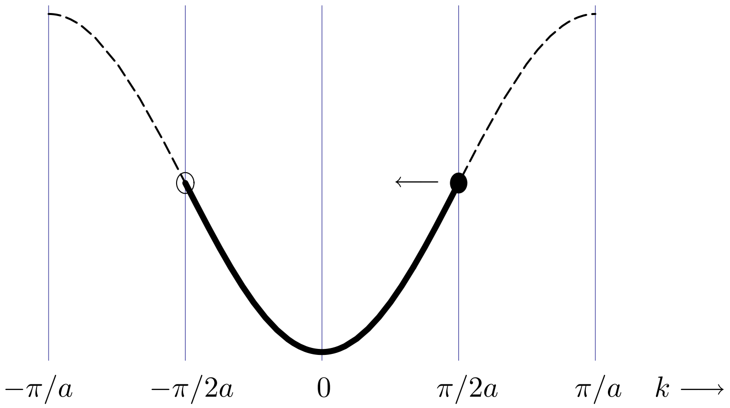

Figure 7.1: *A simple picture of allowed electron scattering processes in an infinite one-dimensional tight-binding chain with interatomic distance a. For one conduction electron per atom in the chain the characteristic cosine-band is half-filled and the Fermi wavevector equals* $k_F = \pi/2a$. *Since phonon energies are orders of magnitude smaller than electron energies, it implies that under a small bias voltage (compared to the band-width) the electrons can only backscatter to unoccupied states, i.e. only phonons with a wavevector of* $2k_F$ *may be excited.*

has been presented by Montgomery *et al.* [36]. They considered a *three-dimensional* single-orbital tight-binding model for a system consisting of a linear nine-atom chain connected to semi-infinite metallic electrodes.

With parameters fitted for Au they determined the phonon modes for a geometry in which the wire atoms as well as a number of atoms in the contact region were allowed to move. Based on standard first-order perturbation theory for the inelastic scattering rate, as well as some suitable simplifications, they arrived at an equation for the total inelastically backscattered current. In terms of conductance their result suggests a series of drops at different biases with each drop corresponding to activation of a particular phonon mode. In particular they found two dominant drops corresponding to two different longitudinal vibrations.

In this chapter we take a slightly different approach for modelling the experiment. As a simplification of the problem we restrict the description to a *one-dimensional* single-orbital tight-binding model and determine phonon modes for an N-atom wire connected to rigid electrodes. In this aspect our treatment is – in contrast to Montgomery *et al.*'s – limited to longitudinal phonon modes only. But, as their results suggest these modes are the important ones. On the other hand, our treatment of the inelastic effects is based on the full NEGF method described in the previous chapters.

The calculation of the phonon modes and the electron-phonon couplings falls in two parts: First, we determine the vibrational modes of the chain simply by modelling the heavy ions as classical balls-and-springs. Second, we expand a parametric dependence of the electronic hopping elements on atomic displacements to linear order to find the couplings. Often this second step is referred to as the Su-Schrieffer-Heeger (SSH) model [71], a model which recently have been invoked in various contexts of inelastic molecular transport [72, 73, 74].

As pointed out in Sec. 2.4.2 the correct treatment of the electron-phonon interaction in the Born-Oppenheimer approximation is to include the dynamical electronic screening when one calculates the modes. Here we will just assume that we can find appropriate spring constants that give authentic modes and frequencies.

It is known that a one-dimensional metal is subject to a so-called Peierl's instability which, at low temperatures, opens up a gap in the band structure due to a static structural distortion [75]. Essentially this effect is a result of a competition between an increase in elastic strain energy associated with the atomic dimerization and a decrease in electronic energy due to change in the band structure. However, according to theoretical calculations for Au atomic chains the Peierl's distortion seem to be neglible (at most slightly noticeable just before the wire breaks) [76, 77]. We therefore in the following disregard any such effects in our treatment.

7.2 Vibrations of one-dimensional chains

We set out by considering the mechanics of the atomic system. The motion of the ions are considered as small oscillations about positions of equilibrium and for this situation the Lagrangian formulation of the problem is a suitable choice [78]. It is assumed that the deviations of the system from stable equilibrium are small enough to be described within the harmonic approximation, i.e. that these can be modelled by a system of coupled linear harmonic oscillators. The Lagrangian for a system consisting of N atoms is given by

$$\mathscr{L} = T - V, \tag{7.1a}$$

$$T = \frac{1}{2}\sum_{i=1}^{N} m_i \dot{q}_i^2, \tag{7.1b}$$

$$V = \frac{1}{2}\sum_{i=1}^{N-1}\sum_{j=1}^{N-1} K_{i,j}(q_i - q_j)^2, \tag{7.1c}$$

where q_i is the deviation of atom i from its equilibrium position. The mass of atom i is denoted m_i and the effective spring constant for mutual interaction between atom i and j is denoted $K_{i,j}$. We narrow the problem by considering only nearest neighbor interactions here, i.e. $K_{i,j} = K_i\delta_{i,j-1}$.

7.2.1 Normal modes of vibration

Introducing the vector notation $q \equiv (q_1, q_2, \ldots, q_N)^T$ the kinetic energy T and potential energy V can be written on a matrix form

$$T = \frac{1}{2}\dot{q}^T \mathbf{T} \dot{q}, \tag{7.2a}$$

$$V = \frac{1}{2} q^T \mathbf{V} q, \tag{7.2b}$$

where $(\mathbf{T})_{ij} = m_i \delta_{i,j}$ and $(\mathbf{V})_{ij} = (K_i + K_{i-1})\delta_{i,j} - K_i \delta_{i,j-1} - K_{i-1}\delta_{i,j+1}$ are matrix representations in basis $\{q_i\}$.

Before looking at the equations of motion it is convenient to transform into a new set of coordinates defined by the scaling $\zeta_i = \sqrt{m_i} q_i$. This step is essential if the masses are different. In the vector notation we define $\zeta \equiv (\zeta_1, \zeta_2, \ldots, \zeta_N)^T$ and write

$$q = \mathbf{A}\zeta, \qquad [L] = [M^{-1/2}][M^{1/2}L] \tag{7.3}$$

where $(\mathbf{A})_{ij} = (m_i)^{-1/2}\delta_{i,j}$ is the (real symmetric) orthogonal transformation matrix from $\{\zeta_i\}$ to $\{q_i\}$ basis. Inserted in Eq. (7.2) the transformation yields

$$T = \frac{1}{2}\dot{\zeta}^T \mathbf{1} \dot{\zeta}, \tag{7.4a}$$

$$V = \frac{1}{2}\zeta^T \widetilde{\mathbf{V}} \zeta, \tag{7.4b}$$

where $\mathbf{1}$ is the identity matrix and $\widetilde{\mathbf{V}} = \mathbf{A}\mathbf{V}\mathbf{A}^{-1}$ describes the potential in the new set of coordinates $\{\zeta_i\}$. Now, taking the ζ_i's as generalized coordinates, the Lagrange equations

$$\frac{\mathrm{d}}{\mathrm{d}t}\left(\frac{\partial L}{\partial \dot{\zeta}_i}\right) - \frac{\partial L}{\partial \zeta_i} = 0, \tag{7.5}$$

give the following N equations of motion

$$\ddot{\zeta}_i + \sum_j (\widetilde{\mathbf{V}})_{ij}\zeta_j = 0, \tag{7.6}$$

or simply

$$\ddot{\zeta} + \widetilde{\mathbf{V}}\zeta = 0. \tag{7.7}$$

Looking for an oscillatory solution of the problem we try

$$\zeta_i = c_i e^{-i\omega t} \tag{7.8}$$

which yields the matrix problem

$$(\widetilde{\mathbf{V}} - \omega^2 \mathbf{1})\zeta = 0 \tag{7.9}$$

for the coefficients. The above only has a solution if the determinant vanishes

$$|\widetilde{\mathbf{V}} - \omega^2 \mathbf{1}| = 0. \tag{7.10}$$

This equation is known as the *characteristic* or *secular* equation of the matrix. In general, there are N solutions for ω^2. For each of these we find the corresponding eigenvector e_λ from Eq. (7.9) by insertion of the eigenvalue. We take these eigenvectors to be normalized as $e_\lambda \cdot e_\lambda = 1$.

With these eigenvectors we build a real orthogonal transformation matrix $\mathbf{B}$

$$\mathbf{B} = [e_1 e_2 \cdots e_N], \tag{7.11}$$

that relates the coordinates $\{\zeta_i\}$ to a new set of coordinates $\{Q_\lambda\}$ as

$$\zeta = \mathbf{B}Q, \qquad [M^{1/2}L] = [1][M^{1/2}L]. \tag{7.12}$$

Now, the combined transformation $\mathbf{C} = \mathbf{AB}$ simultaneously diagonalizes both $\mathbf{T}$ and $\mathbf{V}$ in Eq. (7.2),

$$T = \frac{1}{2}\dot{Q}^T \mathbf{1} \dot{Q}, \tag{7.13a}$$

$$V = \frac{1}{2} Q^T \mathbf{\Lambda} Q, \tag{7.13b}$$

where $\mathbf{\Lambda} = \mathbf{C}^{-1}\mathbf{V}\mathbf{C}$ contains the eigenfrequencies ω_λ along the diagonal. These new coordinates Q_λ are customarily called the *normal coordinates* of the system because each normal coordinate corresponds to a vibration of the system with only one frequency ω_λ. The relation to the initial coordinates q_i is given by

$$q = \mathbf{C}Q = \mathbf{AB}Q. \tag{7.14}$$

We will also refer to the *conjugate momentum* P_λ to normal coordinate Q_λ defined as [78]

$$P_\lambda \equiv \frac{\partial L}{\partial \dot{Q}_\lambda} = \dot{Q}_\lambda. \tag{7.15}$$

where the last equality follows from Eq. (7.13). The terms canonical or generalized momentum are also often used for P_λ.

7.2.2 Quantization of the vibrations

The vibrations are now canonically quantized by assuming that the normal mode operators Q_λ and P_λ have the usual commutation relation

$$[Q_\lambda, P_{\lambda'}] = i\hbar \delta_{\lambda,\lambda'}. \tag{7.16}$$

Defining dimensionless operators,

$$b_\lambda = \sqrt{\frac{\omega_\lambda}{2\hbar}}Q_\lambda + i\sqrt{\frac{1}{2\hbar\omega_\lambda}}P_\lambda, \tag{7.17a}$$

$$b_\lambda^\dagger = \sqrt{\frac{\omega_\lambda}{2\hbar}}Q_\lambda - i\sqrt{\frac{1}{2\hbar\omega_\lambda}}P_\lambda, \tag{7.17b}$$

which from Eq. (7.16) satisfies the relation $[b_\lambda, b_{\lambda'}^\dagger] = \delta_{\lambda,\lambda'}$, we write Q_λ and P_λ in terms of these

$$Q_\lambda = \sqrt{\frac{\hbar}{2\omega_\lambda}}(b_\lambda^\dagger + b_\lambda), \tag{7.18a}$$

$$P_\lambda = i\sqrt{\frac{\hbar\omega_\lambda}{2}}(b_\lambda^\dagger - b_\lambda). \tag{7.18b}$$

We can also express the initial coordinates q_i in terms of the dimensionless operators b_λ and $b_\lambda^\dagger$ as

$$\begin{aligned} q_i &= \sum_{j,\lambda} \mathbf{A}_{ij}\mathbf{B}_{j\lambda}\sqrt{\frac{\hbar}{2\omega_\lambda}}(b_\lambda^\dagger + b_\lambda) \\ &= \sum_\lambda (e_\lambda)_i \sqrt{\frac{\hbar}{2m_i\omega_\lambda}}(b_\lambda^\dagger + b_\lambda). \end{aligned} \tag{7.19}$$

In terms of the normal coordinates we can write the Hamiltonian $\mathscr{H}_{\text{ion}}$ for the atomic system as

$$\begin{aligned} \mathscr{H}_{\text{ion}} &= T + V \\ &= \frac{1}{2}\sum_\lambda (P_\lambda P_\lambda + \omega_\lambda^2 Q_\lambda Q_\lambda) \\ &= \sum_\lambda \Omega_\lambda (b_\lambda^\dagger b_\lambda + \frac{1}{2}), \end{aligned} \tag{7.20}$$

where $\Omega_\lambda = \hbar\omega_\lambda$ is the mode energy. This form makes it evident that the system is considered as consisting of N independent oscillators.

7.3 Tight binding model for electronic orbitals

We next turn towards a model for the electronic system. In a tight-binding description of the conducting electrons we write the electronic Hamiltonian as

$$\mathscr{H}_{\text{e}} = \sum_i \xi_i c_i^\dagger c_i + \frac{1}{2}\sum_{i,j} t_{i,j}(c_i^\dagger c_j + \text{h.c.}), \tag{7.21}$$

where ξ_i is the on-site energy and $t_{i,j}$ the hopping element between localized orbitals $|i\rangle$ and $|j\rangle$. As mentioned in Sec. 7.1 the effect of the longitudinal

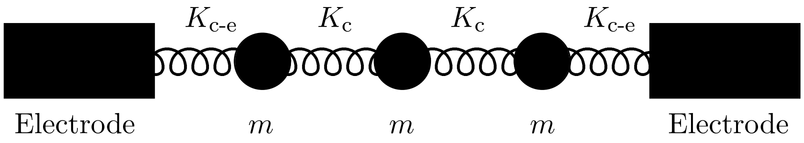

Figure 7.2: *Graphical representation of balls-and-springs model where the ends are fixed by choosing sufficiently large masses for the numerical calculation. Thus, a 3-atom chain as depicted is modelled with 5 masses and 4 springs.*

vibrations of the ions will be considered in the SSH model [71] in which the hopping parameter $t_{i,j}$ is expanded to first order in terms of the atomic displacements from equilibrium

$$t_{i,j} \;=\; t^0_{i,j} + \alpha_{i,j}(q_i - q_j). \tag{7.22}$$

where $t^0_{i,j}$ is the hopping parameter when $q_i - q_j = 0$ and $\alpha_{i,j} = (\mathrm{d}t_{i,j}/\mathrm{d}q_i)_{q_i=0}$ $= -\alpha_{j,i}$. Inserting the quantized expression Eq. (7.19) for q_i we get

$$t_{i,j} \;=\; t^0_{i,j} + \sum_\lambda (\mathbf{M}^\lambda)_{ij}(b^\dagger_\lambda + b_\lambda) \tag{7.23}$$

where the electron-phonon coupling $\mathbf{M}^\lambda$ has been identified as

$$(\mathbf{M}^\lambda)_{ij} \;=\; \alpha_{i,j}\left\{\frac{(e_\lambda)_i}{\sqrt{m_i}} - \frac{(e_\lambda)_j}{\sqrt{m_j}}\right\}\sqrt{\frac{\hbar}{2\omega_\lambda}}. \tag{7.24}$$

The full hamiltonian for the system can thus be written as

$$\mathscr{H} \;=\; \mathscr{H}^0_{\mathrm{e}} + \mathscr{H}_{\text{e-ph}} + \mathscr{H}_{\text{ion}}, \tag{7.25a}$$

$$\mathscr{H}^0_{\mathrm{e}} \;=\; \sum_i \xi_i\, c^\dagger_i c_j + \frac{1}{2}\sum_{i,j} t^0_{i,j}(c^\dagger_i c_j + \text{h.c.}), \tag{7.25b}$$

$$\mathscr{H}_{\text{e-ph}} \;=\; \frac{1}{2}\sum_{\lambda,i,j}(\mathbf{M}^\lambda)_{ij}(c^\dagger_i c_j + \text{h.c.})(b^\dagger_\lambda + b_\lambda) \tag{7.25c}$$

$$\mathscr{H}_{\text{ion}} \;=\; \sum_\lambda \Omega_\lambda(b^\dagger_\lambda b_\lambda + \frac{1}{2}). \tag{7.25d}$$

where $\Omega_\lambda = \hbar\omega_\lambda$ and $(\mathbf{M}^\lambda)_{ij} = (\mathbf{M}^\lambda)_{ji}$ is a real symmetric matrix.

7.4 Numerics

The approach described above in Sec. 7.2 and 7.3 provides a way to calculate the different electron-phonon couplings given some model parameters for the spring constants $K_{i,j}$ and the masses m_i as well as the hopping $t^0_{i,j}$ and its modulation $\alpha_{i,j}$ with atomic displacements. Note that the prescription for the determination of normal modes and eigenfrequencies as put forward in Sec. 7.2 handles the general case where all spring constants and masses are different.

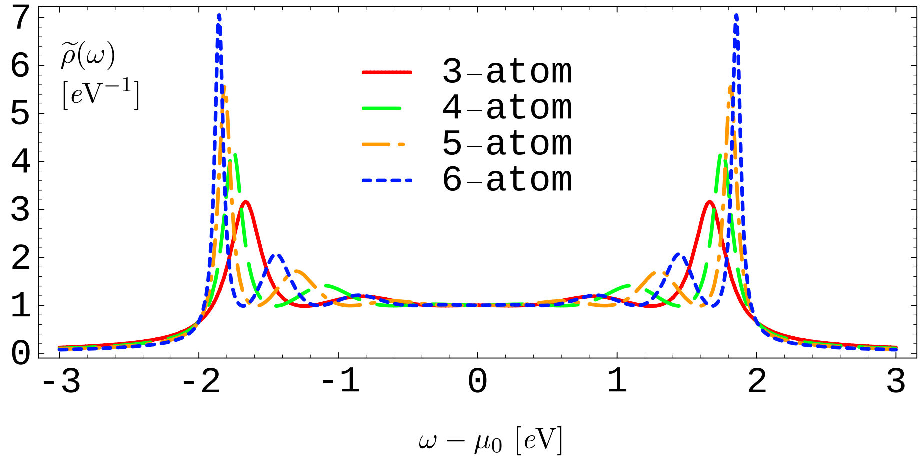

Figure 7.3: *Density of states (DOS) for the N-atomic systems normalized by the total number of sites in the model, i.e. $\widetilde{\rho}(\omega) = \rho(\omega)/(N+2)$. One sees the signature of divergences at the band edges characteristic for the infinite one-dimensional tight-binding chain.*

7.4.1 Parameters for Au chains

Let us now extract some reasonable parameters for the atomic Au chains. As a generic example we consider a 3-atom wire coupled to two electrodes as illustrated in Fig. 7.2. Each electrode is represented by a (fixed) single electronic orbital which we think of as being coupled to the next layers in the electrode. Our strategy is to determine the modes of vibration for the chain by considering an isolated system of five masses (three masses in the chain and two electrodes) and four springs.

As indicated on the figure we take the spring constant $K_{\text{c-e}}$ between end sites of the chain and the electrodes to be different than that between atoms inside the chain K_c. The reason for this is the general property of metallic bonding that bond strengths increase with decreasing coordination number [36]. Since the contact atoms – linking the end sites of the wire with the bulk electrodes – have more bonds than atoms inside the chain we expect K_{c} to be slightly stiffer than $K_{\text{c-e}}$. In the following we assume this effect is appropriately accounted for by taking $K_{\text{c}} = 2K_{\text{c-e}}$.

The masses m_i of the atoms in the chain is for obvious reasons taken to be that of Au (197 a.m.u. [75]). The masses of the electrodes are considered to be infinitely large which serves to keep them fixed in space (numerically it is sufficient that they are a couple of orders of magnitude larger than m_i). For the tight-binding model we choose for the nearest neighbor hopping element $t^0_{i,j} = 1eV$, for the broadening of the contact atoms $\Gamma_{L/R} = 2eV$, and for the equilibrium filling level $\mu_{\text{eq}} = 0$. These parameters serve to yield an unperturbed zero-bias conductance of one quantum unit $G_0 = 2e^2/h$ appropriate for Au chains. Beside capturing this essential property their precise values does not seem to be determining for the outcome of the present

Physical quantity	Symbol	Value	Unit
Equilibrium filling	μ_{eq}	0.00	eV
On-site energy	ξ_i	0.00	eV
Intersite hopping	$t^0_{i,j}$	1.00	eV
Hopping modulation	$\alpha_{i,j}$	0.96	eV/Å
Electrode coupling	$\Gamma_{L/R}$	2.00	eV
Temperature	T	4.20	K
Atomic mass	m	197	a.m.u.†
Spring constant in chain	K_{c}	2.00	$e\mathrm{V}/\mathrm{Å}^2$
Spring constant chain-electrode	$K_{\text{c-e}}$	1.00	$e\mathrm{V}/\mathrm{Å}^2$

† Atomic weight of Au

Table 7.1: *Parameters used in the present model of Au atomic chains.*

analysis. In Fig. 7.3 we show the density of states for a number of shorter tight-binding chains. Also, we set the temperature to $T = 4.2K$ as in the experiment.

We do now have two more parameters to be determined, a spring constant K_{c} and the linear expansion coefficient $\alpha_{i,j}$ introduced in Eq. (7.22) describing the modulation of the hopping amplitude by an atomic displacement. First, we expect the mode frequencies to be of the order ~10-20meV which is obtained by taking $K_{\mathrm{c}} = 2e\mathrm{V}/\mathrm{Å}^2$. Finally, we try $\alpha_{i,j} = 0.96e\mathrm{V}/\mathrm{Å}$. Since this quantity is a proportionality factor for the coupling matrix we expect the effects of the interaction to scale with it as well. As we will see below it turns out that for this particular choice we actually recover conductance drops of the same order as in the experiment. All parameters used in our numerical calculations are summarized in Tab. 7.1.[1]

7.4.2 Vibrational modes and couplings

The prescribed method in Sec. 7.2 is used to determine its normal modes and normal frequencies for N-atomic chains.[2] As an example we visualize the results of such calculations for the 3-atom and the 4-atom chain in Fig. 7.4 and 7.5, respectively. Since we include the electrode masses in the calculation we find $N + 2$ modes for an N-atomic wire. Two of these modes will be disregarded since one corresponds to a trivial translation (T)

---

[1] The mechanical properties of the infinite Au chain have been studied using DFT by Bahn [77] (p. 62). For the relaxed structure he calculated the following parameters: Interatomic distance $d = 2.65$Å, (s-band) hopping matrix element estimate $t_0 = 0.55e$V, derivative $\alpha = \partial t/\partial d \approx 0.6e\mathrm{V}/\mathrm{Å}$, and elastic constant $K_0 = 8e\mathrm{V}/\mathrm{Å}^2$. He further found that the effective elastic constant goes down as the wire is stretched from equilibrium. In conclusion, we see that our very different approaches seem to yield roughly the same parameter values.

[2] For the numerical calculations it is convenient to adopt the atomic units where $m_e = \hbar = e = 1$ and one thus measures energies in Hartree's $E_h = 2 \cdot 13.6056923e$V, lengths in Bohr radii $r_0 = 0.529177$Å, and masses in units of electron rest masses $m_e = 9.1093826 \cdot 10^{-31}$kg (a.m.u.) [79].

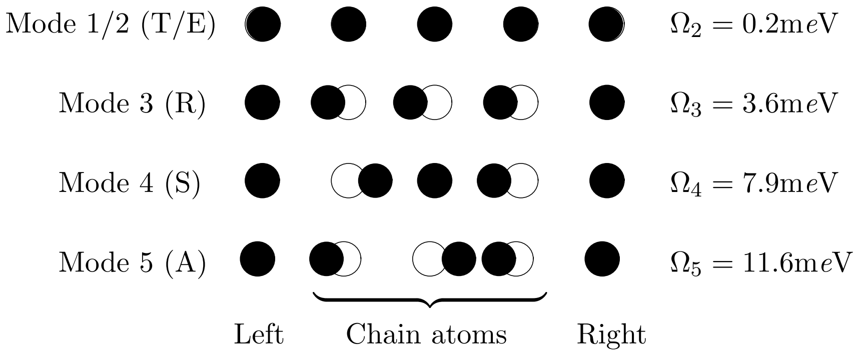

Figure 7.4: *Graphical representation of the normal modes of the 3-atom chain. Mode 1 corresponds to a translation (T) of the whole chain and mode 2 to oscillation of the electrodes (E). These modes will be disregarded in our calculations. The modes labelled 3-5 are the three relevant ones for our 3-atom wire. We will refer to mode 3 as the rigid (R) mode since the whole chain oscillates as one piece. Mode 4 is seen to be a symmetric (S) mode while mode 5 is antisymmetric (A).*

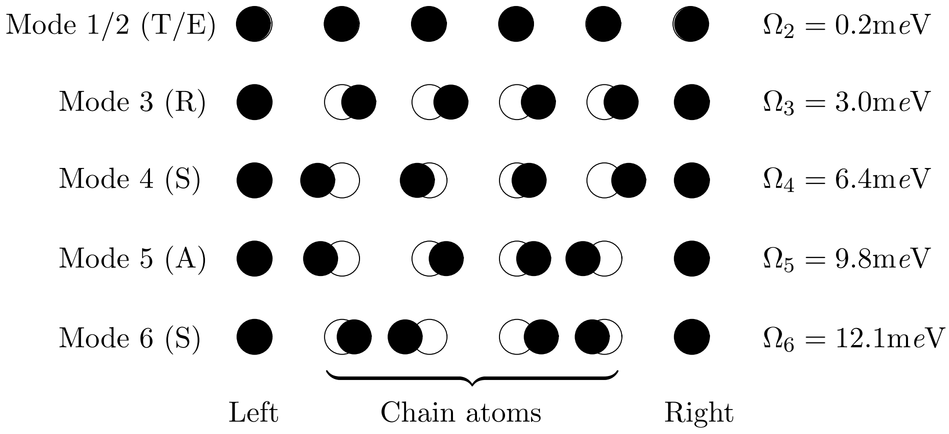

Figure 7.5: *Graphical representation of the normal modes of the 4-atom chain. As mentioned in the caption of Fig. 7.4 we disregard modes 1-2 (T) and (E). The modes labelled 3-6 are the relevant ones for the 4-atom chain.*

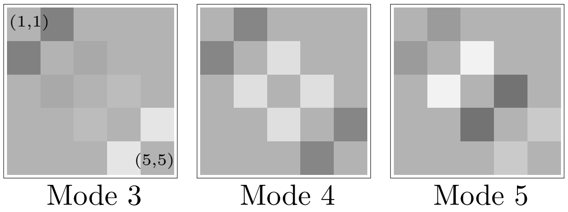

(a) 3-atom chain

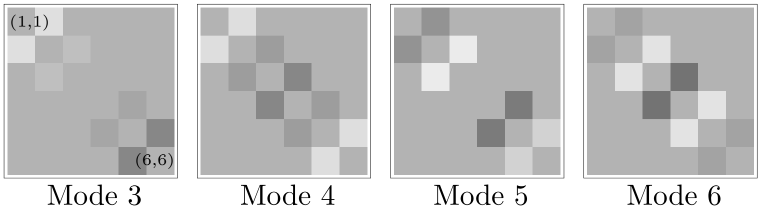

(b) 4-atom chain

Figure 7.6: *Density plot of the interaction matrices in real-space basis of the 3-atom and 4-atom chains. The zero-point is set by the graylevel of the diagonal and a dark (bright) area indicates the corresponding element of the matrix is positive (negative).*

of the whole system and another one to a fixed chain and slowly oscillating electrodes (E).

For each mode we determine the electron-phonon coupling matrix $\mathbf{M}^\lambda$ from Eq. (7.24). For the 3-atom system our description this is a 5×5 matrix and for the 4-atom system a 6×6 matrix. To communicate what these matrices look like in the real-space tight-binding representation we show density plots of these in Fig. 7.6. Since we restricted the model to nearest neighbor hopping the only nonzero elements are those adjacent to the main diagonal. In the density plot the grayscale deviation from neutral (e.g. diagonal elements) expresses both sign and magnitude of each element.

The first observation is that all coupling matrices contain elements of the same order of magnitude $|M_{i,j}^\lambda| \lesssim 30\mathrm{m}e\mathrm{V}$. From this alone one could imagine that they should all influence the electron transport, but as we will see below such conclusions are elusive.

Another observation is that the higher the energy of a mode is (larger label number) the more the elements are changing along the nonzero diagonals. This simply reflects that the higher energy of a mode the shorter is the corresponding wavelength, cf. Fig. 7.4 and 7.5.

7.4.3 Conductance

As mentioned above we treat the (fixed) contact atoms as being coupled to bulk electrodes represented by a constant level broadening $\Gamma_{L/R}$. At this point we thus have all ingredients at hand for a full I–V calculation based on our NEGF method for inelastic transport.

For instance, in order to investigate the influence of mode $\lambda = 5$ on the conduction through the 3-atom chain ($\Omega_5 = 11.6\mathrm{m}e\mathrm{V}$) we have the following parameters

$$\mathbf{H}^0 = \begin{pmatrix} 0 & -1 & 0 & 0 & 0 \\ -1 & 0 & -1 & 0 & 0 \\ 0 & -1 & 0 & -1 & 0 \\ 0 & 0 & -1 & 0 & -1 \\ 0 & 0 & 0 & -1 & 0 \end{pmatrix}, \tag{7.26a}$$

$$\mathbf{\Gamma}_L = \begin{pmatrix} 2 & 0 & 0 & 0 & 0 \\ 0 & 0 & 0 & 0 & 0 \\ 0 & 0 & 0 & 0 & 0 \\ 0 & 0 & 0 & 0 & 0 \\ 0 & 0 & 0 & 0 & 0 \end{pmatrix}, \qquad \mathbf{\Gamma}_R = \begin{pmatrix} 0 & 0 & 0 & 0 & 0 \\ 0 & 0 & 0 & 0 & 0 \\ 0 & 0 & 0 & 0 & 0 \\ 0 & 0 & 0 & 0 & 0 \\ 0 & 0 & 0 & 0 & 2 \end{pmatrix}, \tag{7.26b}$$

$$\mathbf{M}^{\lambda=5} = \begin{pmatrix} 0 & 0.013 & 0 & 0 & 0 \\ 0.013 & 0 & -0.035 & 0 & 0 \\ 0 & -0.035 & 0 & 0.035 & 0 \\ 0 & 0 & 0.035 & 0 & -0.013 \\ 0 & 0 & 0 & -0.013 & 0 \end{pmatrix}, \tag{7.26c}$$

where the above quantities have units eV.

For all modes of both the 3-atom and 4-atom chain we carried out a full I–V calculation taking the bias voltage to be applied symmetrically across the wire, i.e. $\mu_{L(R)} = \mu_{\mathrm{eq}} + (-)eV/2$. The results of these calculations are shown in terms of differential conductance in Fig. 7.7.

For the 3-atom chain we observe a conductance drop at the threshold voltages for modes 3 and 5 but see absolutely no signature from mode 4. For the 4-atom chain we similarly find conductance drops for modes 4 and 6 whereas none for 3 and 5. Considering the coupling matrices only, the pattern that some modes have a drop while others do not is *a priori* unexpected. Also, it looks like the high energy mode is the one that causes the most significant conductance drop (around 1%).

We have also studied chains of more atoms ranging up to 40 atoms. The results are summarized in Tab. 7.2 and are in accord with the findings mentioned above for the 3- and 4-atom chains. The findings suggest some kind of selection rule for which modes that influence the electron transport:

> *the conductance through wires with an odd (even) number of atoms are only affected by antisymmetric (symmetric) vibrational modes.*

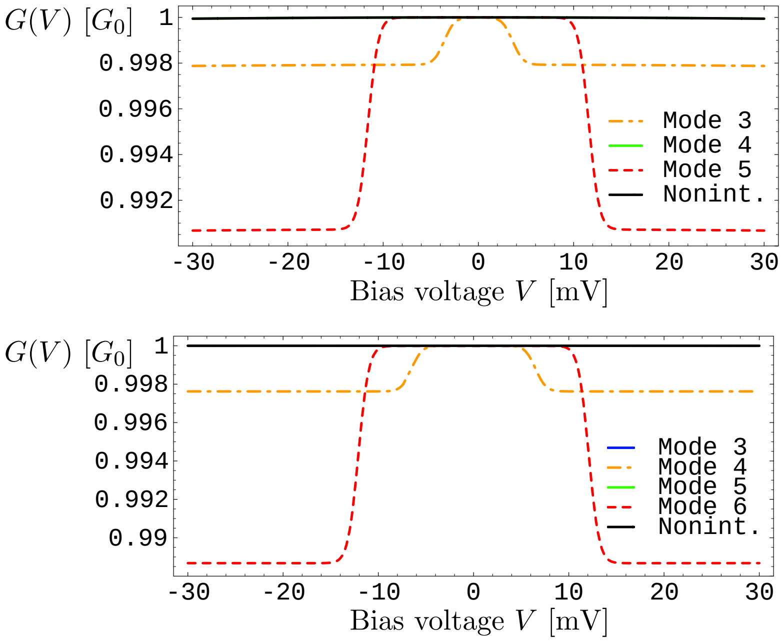

Figure 7.7: *Differential conductance $G(V)$ of the 3-atom chain (upper plot) and the 4-atom chain (lower plot).*

The above stated selection rule does also seem to hold for less symmetric settings. For the 4-atom chain we have made a few spot checks with different filling level ($\mu_{\text{eq}} = 0.1eV$) and asymmetric biases ($\mu_L = \mu_{\text{eq}} + 2eV/3$, $\mu_R = \mu_{\text{eq}} - eV/3$). Essentially our selection rule holds here as well.[3]

From Tab. 7.2 we also observe that the conductance drops seem to increase with increasing wire length. This relationship is investigated in Fig. 7.8 for the mode with highest energy $\lambda = N$. The figure clearly shows that the conductance drop scales linearly with the length of the chain and that the intercept of a linear fit is close to zero. From this we conclude that the inelastic scattering of electrons from this mode is taking place inside the wire, i.e. it does not seem to be related to scattering at contact-wire interface.

---

[3] We do actually numerically detect a tiny drop for mode 5 for these settings but it is still much smaller than modes 4 and 6.

Atoms in chain	Mode	Ω_λ [meV]	Max$\|M^\lambda_{i,j}\|$ [meV]	$\Delta G/G_0$ [%]	Attribute
3	1	0.0	–	–	T
	2	0.2	5.0	–	E
	3	3.6	28.0	0.20	R
	4	7.9	24.6	$< 10^{-3}$	S
	5	11.6	35.3	0.93	A
4	1	0.0	–	–	T
	2	0.2	4.5	–	E
	3	3.0	24.6	$< 10^{-3}$	R
	4	6.4	24.4	0.24	S
	5	9.8	31.1	$< 10^{-3}$	A
	6	12.1	35.7	1.17	S
5	1	0.0	–	–	T
	2	0.1	4.1	–	E
	3	2.6	21.9	0.12	R
	4	5.5	23.4	$< 10^{-3}$	S
	5	8.4	22.3	0.25	A
	6	10.8	29.7	$< 10^{-3}$	S
	7	12.4	31.2	1.35	A
6	1	0.0	–	–	T
	2	0.1	3.7	–	E
	3	2.3	19.8	$< 10^{-3}$	R
	4	4.8	22.1	0.15	S
	5	7.3	20.6	$< 10^{-3}$	A
	6	9.6	26.0	0.25	S
	7	11.4	26.3	$< 10^{-3}$	A
	8	12.6	30.2	1.58	S
19	15	10.9	–	0.12	A
	16	11.5	–	$< 10^{-2}$	S
	17	11.9	–	0.21	A
	18	12.3	–	$< 10^{-2}$	S
	19	12.6	–	0.53	A
	20	12.8	–	$< 10^{-2}$	S
	21	12.9	–	4.55	A
20	16	11.1	–	0.12	S
	17	11.6	–	$< 10^{-2}$	A
	18	12.0	–	0.22	S
	19	12.4	–	$< 10^{-2}$	A
	20	12.6	–	0.57	S
	21	12.8	–	$< 10^{-2}$	A
	22	12.9	–	4.78	S
30	32	13.0	–	6.70	S
40	42	13.0	–	8.65	S

Table 7.2: *Numerical results for the study of atomic chains of various lengths. The attributes of the modes are described by one of the following tags: (T) translation of the whole system, (E) oscillating electrodes, (R) rigid vibrational mode, (S) symmetric mode, and (A) antisymmetric mode.*

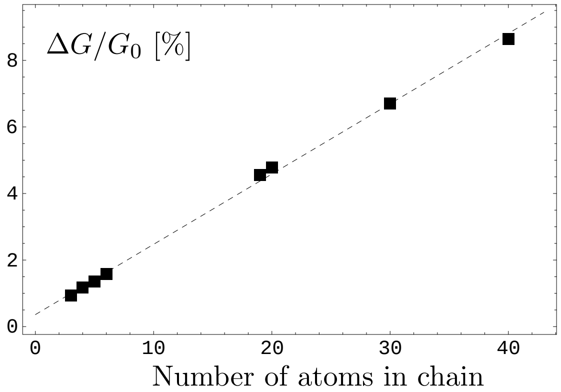

Figure 7.8: *Conductance drop for the (dominant) highest energy mode $\lambda = N$ as a function of number of atoms in the chain. The dotted line is a linear fit.*

7.4.4 Energy dissipation

As shown in Chap. 3 we can – in a very similar fashion as we calculate the current – also compute the power P_{ph} transferred to the phonon system within the framework of our first/self-consistent Born approximations (1BA/SCBA). It is worth restating that we model the phonons as unperturbed by the electrons. This imperfect simplification has the interpretation that any excitation in the phonon system caused by a passing electron is damped out before the next electron enters the wire. In other words, any excess energy than thermally available in the oscillators is immediately absorbed.

The voltage-dependency of P_{ph}, determined from Eq. (3.38), has been calculated for each of the modes for the 3-atom and 4-atom chains.[4] The results are plotted in Fig. 7.9. As expected we find that when the bias voltage is large enough to activate a given mode the conductance drop is accompanied by an energy transfer to the phonon system. We see that it is the same modes that give significant conductance drops that also have significant influence on the power balance.

In Fig. 7.9 we show both the absolute value of the calculated power transfer $P_{\mathrm{ph}}(V)$ as well as the relative value P_{ph}/P_0, where the total electronic power P_0 passing through the wire is defined as

$$P_0(V) \equiv G_0 V^2. \tag{7.27}$$

As seen on the figure the transferred power is relatively small ($< 0.3\%$) compared to P_0. This finding is in agreement with the experimental fact that Au atomic chains can sustain very large currents up to 80μA (corresponding to a voltage up to 1V) [80], i.e. that most of the power carried by the current is dissipated in the electrodes far away from the contact.

---

[4] As one sees from Eq. (3.38) the convergence of the integral on a finite interval is slower than for the current Eq. (3.16) because of the factor ω. Thus, a grid sufficiently ranged for a current calculation might not be so for a power calculation.

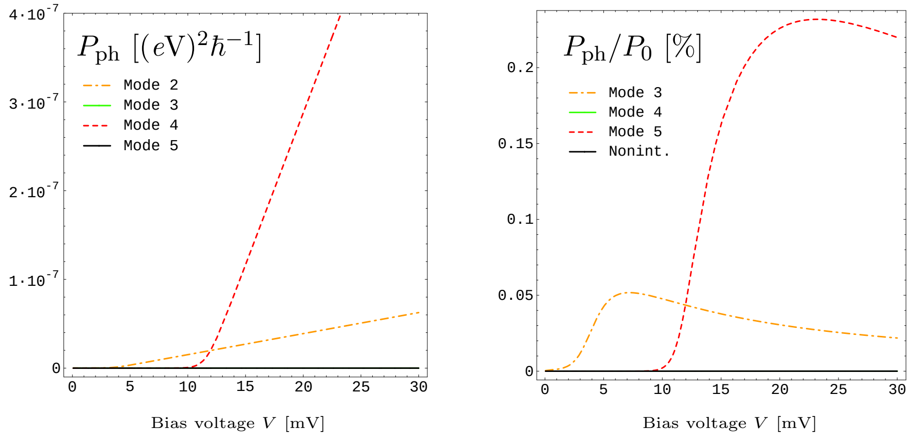

(a) 3-atom chain

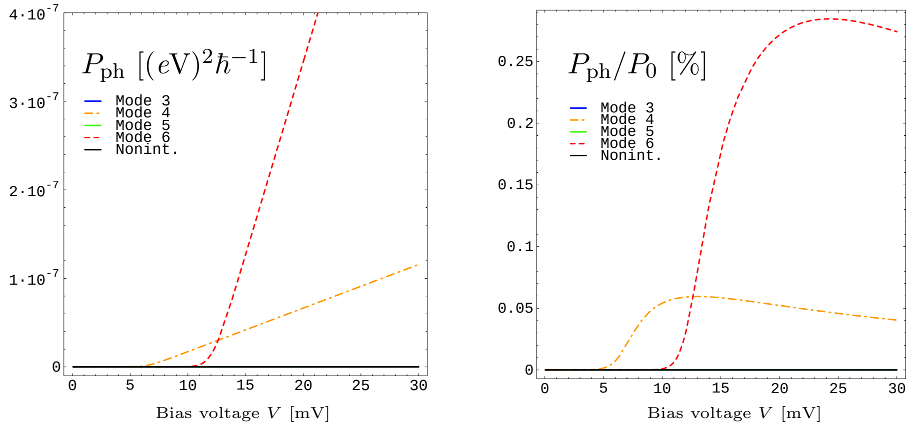

(b) 4-atom chain

Figure 7.9: *Power P_{ph} transferred to the phonon system for the 3-atom and 4-atom chain. The plots to the left show the absolute values while the plots to the right are scaled by the electronic power passing through the wire $P_0(V) \equiv G_0V^2$.*

The plots of the absolute power transfer (left plots in Fig. 7.9) are seen to go linearly with bias voltage above the threshold voltage. This is a very non-ohmic behavior that fits perfectly with a ballistic picture of the transport through the wire: We know that the current is proportional to the (externally) applied bias since the conductance is fairly constant. Thus, when the incoming particles have a certain probability for being inelastically backscattered – and thereby transferring energy to the phonon system – we expect the power to scale linearly with the current.

7.5 Conclusions

In this chapter we studied inelastic effects in metallic atomic wires using our NEGF method combined with a fairly simple one-dimensional model to determine the electron-phonon couplings. This model had two main ingredients: First, the vibrational modes and frequencies of the heavy atoms in the chain were found by modelling the system as classical ball-and-springs. This allowed for writing the mechanical problem in terms of normal coordinates for independent oscillators, which then were canonically quantized by imposing the usual operator commutation relation. Second, the electronic system were described by the SSH model in which a parametric dependence of hopping elements on atomic displacements were expanded to linear order. This in turn lead to an explicit expression for the electron-phonon coupling matrices Eq. (7.24).

With model parameters fitted to describe Au wires we calculated the electron-phonon coupling matrices for chains of up to 40 atoms. It was found that independent of length the coupling matrices all contained elements of roughly the same order of magnitude. From this alone one could be lead to believe that they should all have impact on the conductance. This hypothesis were found not to be consistent with the NEGF calculations which indicated a selection rule. Also, the calculations disclosed one dominant mode in the conductance spectrum namely the one with the shortest wavelength.

From the theory presented in this chapter it is straightforward to improve the description by including elastic constants between second-nearest neighbors,[5] or principally between all masses, and to extend to three dimensions (one just take indexes $i, j \in \{1, 2, \ldots, 3N\}$).

---

[5] The importance of such long-ranged contributions for real systems has been pointed out by Montgomery *et al.* [36].

Chapter 8

Summary

8.1 Achievements

In this thesis we have described a method based on nonequilibrium Green's functions (NEGF) for modelling of inelastic electron transport in nanosystems. The general motivation was the future prospects of molecular electronics for which a detailed understanding of inelastic effects will certainly be cardinal.

The essential elements of the presented method were a perturbative treatment of the electron-phonon interaction, a Meir-Wingreen like expression for the current, and the Born-Oppenheimer approximation for separation of the electronic and nuclear degrees of freedom. Whereas most theoretical work by others along these lines focused on transport via a single or a few molecular levels, we generalized to a description involving a large number of electronic states. The method was implemented in PYTHON and compared with results in the literature as well as with own calculations based on an exact diagonalization technique.

As an example demonstrating the full potential of our method we studied electron transport through Au atomic chains of various lengths. The incitement was to gain understanding of the experimentally observed inelastic scattering of electrons in such wires by phonons. A main discovery was that one cannot *a priori* tell from the electron-phonon coupling matrices only which modes that impacts on the current flow.

8.2 *Ab initio* approach to inelastic transport

In Chap. 1 we stated that one of the goals for this work was to develop a method compatible with *ab initio* calculations of electronic structure, vibrational modes, and electron-vibration couplings. To confirm that this was actually achieved we now discuss how these methods can be combined and present some preliminary results on an Au atomic wire.

As shown in Chap. 7 the normal modes of vibration are determined from a description of the atomic system in terms of springs and masses. The

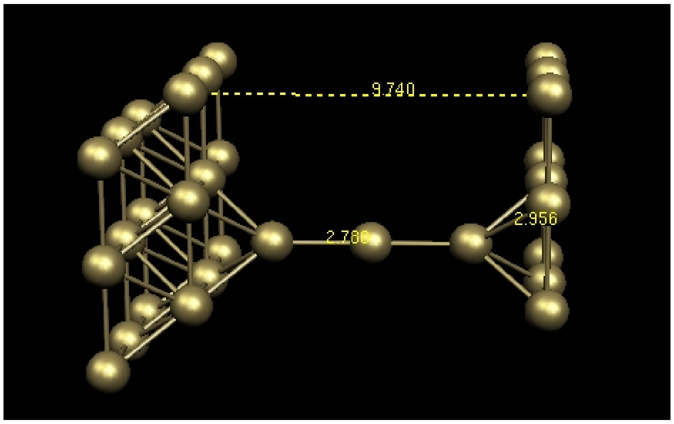

Figure 8.1: *The 3-atom Au chain between gold electrodes being the object for our ab initio calculations. As quoted in the picture, the electrode separation is 9.740Å, the interatomic bond length 2.788Å, and the wire-electrode bond length 2.956Å.*

elastic constants can be determined *ab initio* either by considering forces F_i or by derivatives of the total energy U via

$$K_{i\mu,j\nu} = \frac{\partial F_{i\mu}}{\partial q_{j\nu}} = -\frac{\partial^2 U}{\partial q_{i\mu}\partial q_{j\nu}}, \tag{8.1}$$

where $F_{i\mu}$ is the force component along μ exerted on atom i and $q_{j\nu}$ the component ν of a displacement of atom j from its equilibrium position. $K_{i\mu,j\nu}$ is often referred to as the *force strength matrix* or the *dynamical matrix*. From $K_{i\mu,j\nu}$ and m_i one obtains the normal mode vectors $\{e_\lambda\}$ and normal frequencies $\{\omega_\lambda\}$.

The electronic structure of a Coulomb interacting electron gas moving in some static electron-ion potential can be calculated by density functional theory (DFT) provided the exchange-correlation functional [81, 82]. The method is based on finding the self-consistent solutions to the Kohn-Sham equations which in turn essentially provide the electronic Hamiltonian $\mathscr{H}_\mathrm{e}$ given some particular configuration of the ions. Therefore, if one expands it to linear order in the atomic displacements,

$$\mathscr{H}_\mathrm{e} = \mathscr{H}_\mathrm{e}^0 + \sum_{i\mu} \frac{\partial \mathscr{H}_\mathrm{e}}{\partial q_{i\mu}} q_{i\mu}, \tag{8.2}$$

it is in principle possible to determine the operator $\partial\mathscr{H}_\mathrm{e}/\partial q_{i\mu}$, e.g. by finite difference methods. Expressing the coordinate operators $q_{i\mu}$ in terms of the dimensionless normal mode operators b_λ and $b_\lambda^\dagger$ as in Eq. (7.19) the electron-phonon interaction is given by

$$\mathscr{H}_\text{e-ph} = \sum_{i\mu} \frac{\partial \mathscr{H}_\mathrm{e}}{\partial q_{i\mu}} \sum_\lambda (e_\lambda)_{i\mu} \sqrt{\frac{\hbar}{2m_i\omega_\lambda}} (b_\lambda^\dagger + b_\lambda). \tag{8.3}$$

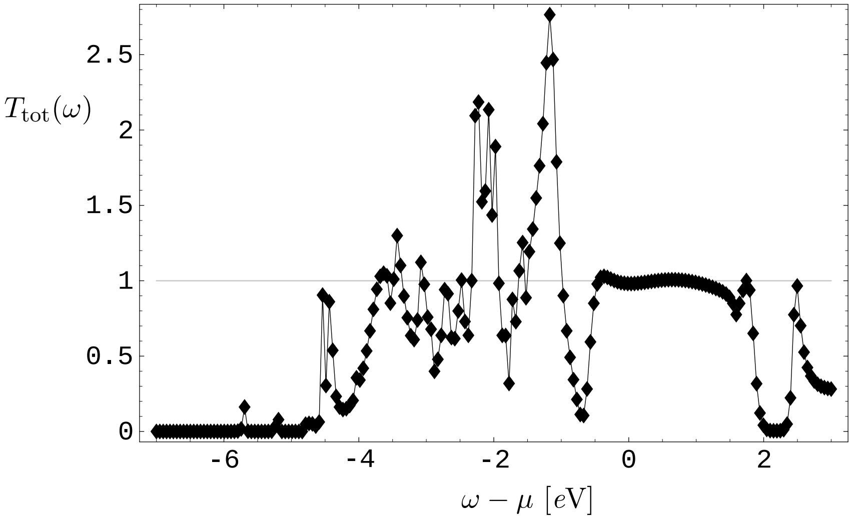

Figure 8.2: *Total transmission function $T_{tot}(\omega)$ of the 3-atom Au chain calculated with* TRANSIESTA.

In a collaborative effort between M. Brandbyge,[1] N. Lorente,[2] and the present writer, we have studied a 3-atom Au chain between two (100) semi-infinite gold electrodes with different approaches to DFT. A small unit cell (3×3) and the so-called Γ-point approximation in the plane perpendicular to the transport direction were used. The geometry is shown in Fig. 8.1.

With the nonequilibrium electronic structure code TRANSIESTA [33], which is based on a basis set of atomic orbitals, we first calculated the transport properties of the system without any vibrational interactions. The results – confirming a zero-bias conductance around the quantum G_0 – are shown in Fig. 8.2. Next, we determined the different vibrational modes and couplings using the plane-wave code DACAPO [83] for the exactly same system (coordinates, exchange-correlation potential, etc.). Among these modes we picked out *one*, essentially the longitudinal antisymmetric mode ($\lambda = 5$) shown in Fig. 7.4.

Now, because of one-to-one correspondence between the eigenstates found by these two methods it is possible to map the electron-phonon coupling matrix from DACAPO's energy basis onto TRANSIESTA's atomic orbital basis.

This imperfect combination of two different schemes originates in the fact that it is not trivial to determine $\partial \mathscr{H}_{\rm e}/\partial q_{i\mu}$ in a non-orthogonal localized basis as is used in TRANSIESTA. In a plane-wave code as DACAPO this task is simpler since the basis states are orthogonal and independent of q_i. On the other hand, in order to calculate transport one needs unambiguously to be able to partition the system, e.g. to define "left" and "right" electrodes.

---

[1] MIC, Department of Micro and Nanotechnology, Technical University of Denmark.

[2] Laboratoire Collisions, Agrégats, Réactivité, IRSAMC, at Université Paul Sabatier, Toulouse, France.

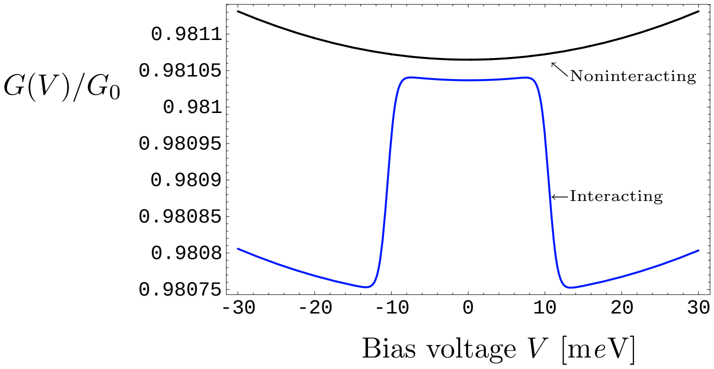

Figure 8.3: *NEGF calculation of the differential conductance for the 3-atom Au chain with and without electron-vibration interaction. The mode considered here is a longitudinal antisymmetric mode with energy* $\Omega = 10.5meV$.

Such a division is problematic within the plane-wave scheme.

Without going into the technical details the above mentioned approach essentially lead us to suitable forms for the 3-atom Hamiltonian $\mathbf{H}$, the electron-vibration coupling $\mathbf{M}$ for the mode chosen, and self-energies due to the semi-infinite electrodes $\mathbf{\Sigma}^r_{L/R}(\omega)$. Taking these as input for a calculation with the present NEGF method we found the conductance characteristics shown in Fig. 8.3. As is evident the calculation does *not* reproduce the $\sim$1% conductance drop experimentally observed. Even though the qualitative features look promising the quantitative drop at the threshold voltage is by far too small.

There are many aspects which need to be investigated before one can draw conclusions. For instance, how appropriate is the unit cell? How accurate is a mapping between the two DFT schemes? Did we consider the relevant mode? Was the particular vibrational mode well described by oscillations of the three wire atoms only? Regardless of these points our message is that the method developed here in principle is compatible with *ab initio* calculations.

8.3 Outlook

Projects as the present one, limited in time, are likely to leave a number of open questions and unresolved issues. In that respect the work put forth here is no exception. Accordingly, we state some ideas for future work below.

In relation to the discussion in Sec. 8.2 a complete calculation of parameters with DFT for the Au atomic wires is obvious. It would be relevant to consider different chain lengths as well as larger "interacting" regions that include also a number of electrode atoms. In particular one could systematically calculate the effect of the different vibrational modes. Preferably we would like to be able to perform all necessary computations without mixing two different DFT schemes.

Regarding the actual NEGF method there are also some things to improve. So far we have only treated the interaction with a single vibrational mode at a time. But in real systems the modes are inseparable. It would therefore be relevant to treat all modes simultaneously.

Our description of the phonon system did not allow for studying heating effects. This highly important aspect might be addressed if also the renormalization of the phonon Green's functions were taken into account. Such a study could also include a model for the coupling of the phonon modes to the environment, in the simplest way just by introducing a finite lifetime by hand.

Finally, a deeper understanding of the tight-binding model and the physics behind the observed selection rule would be relevant to pursue.

Appendix A

Green's functions for noninteracting particles

In this appendix we derive the real-time Green's functions for noninteracting particles. The results are completely standard and can be found in almost any book on many-particle physics. Nevertheless, since they are used again and again in this work it is useful to have them ready at hand.

A.1 Fermions

The Hamiltonian for free (noninteracting) fermions is

$$H_0 \;=\; \sum_{k\sigma} \xi_k c^\dagger_{k\sigma} c_{k\sigma}, \tag{A.1}$$

where $\xi_k = \varepsilon_k - \mu$ is the single-particle energy measured with respect to the chemical potential and $c_{k\sigma}(c^\dagger_{k\sigma})$ is the fermion annihilation (creation) operator. The time-evolution of the annihilation operator in the Heisenberg picture is

$$c_{k\sigma}(t) \;\equiv\; e^{iH_0t/\hbar} c_{k\sigma} e^{-iH_0t/\hbar}, \tag{A.2}$$

so the operator obeys the equation

$$\begin{aligned} i\hbar\frac{\partial}{\partial t} c_{k\sigma}(t) \;&=\; [c_{k\sigma}, H_0](t) \\ &=\; \sum_{k'\sigma'} \xi_{k'} [c_{k\sigma}, c^\dagger_{k'\sigma'} c_{k'\sigma'}](t) = \xi_k c_{k\sigma}(t), \end{aligned} \tag{A.3}$$

where we have used the relation

$$[A, BC] \;=\; \{A, B\}C - B\{A, C\}, \tag{A.4}$$

and the usual fermion anticommutation relations

$$\{c_{k\sigma}, c_{k'\sigma'}\} = \{c^\dagger_{k\sigma}, c^\dagger_{k\sigma}\} = 0, \tag{A.5a}$$

$$\{c_{k\sigma}, c^\dagger_{k\sigma}\} = \delta_{k,k'}\delta_{\sigma,\sigma'}. \tag{A.5b}$$

Eq. (A.3) has the simple solution

$$c_{k\sigma}(t) \;=\; e^{-i\xi_k t/\hbar} c_{k\sigma}. \tag{A.6}$$

The fermion creation operator $c^\dagger_{k\sigma}$ is just the hermitian conjugate of $c_{k\sigma}$, i.e.

$$c^\dagger_{k\sigma}(t) \;=\; e^{i\xi_k t/\hbar} c^\dagger_{k\sigma}. \tag{A.7}$$

The fermion real-time single-particle Green's functions are now simply given as

$$\begin{aligned}
G_0^<(k\sigma t, k'\sigma' t') &\equiv i\hbar^{-1}\langle c^\dagger_{k'\sigma'}(t') c_{k\sigma}(t)\rangle_0 \\
&= i\hbar^{-1} e^{-i\xi_k(t-t')/\hbar}\langle n_{k\sigma}\rangle_0 \delta_{k,k'}\delta_{\sigma,\sigma'}, && \text{(A.8a)}\\
G_0^>(k\sigma t, k'\sigma' t') &\equiv -i\hbar^{-1}\langle c_{k\sigma}(t) c^\dagger_{k'\sigma'}(t')\rangle_0 \\
&= -i\hbar^{-1} e^{-i\xi_k(t-t')/\hbar}[1-\langle n_{k\sigma}\rangle_0]\delta_{k,k'}\delta_{\sigma,\sigma'}, && \text{(A.8b)}\\
G_0^r(k\sigma t, k'\sigma' t') &\equiv -i\hbar^{-1}\theta(t-t')\langle\{c_{k\sigma}(t), c^\dagger_{k'\sigma'}(t')\}\rangle_0 \\
&= -i\hbar^{-1}\theta(t-t') e^{-i\xi_k(t-t')/\hbar}\delta_{k,k'}\delta_{\sigma,\sigma'}, && \text{(A.8c)}\\
G_0^a(k\sigma t, k'\sigma' t') &\equiv i\hbar^{-1}\theta(t'-t)\langle\{c_{k\sigma}(t), c^\dagger_{k'\sigma'}(t')\}\rangle_0 \\
&= i\hbar^{-1}\theta(t'-t) e^{-i\xi_k(t-t')/\hbar}\delta_{k,k'}\delta_{\sigma,\sigma'}, && \text{(A.8d)}
\end{aligned}$$

where $n_{k\sigma} \equiv c^\dagger_{k\sigma} c_{k\sigma}$. The Green's functions have the Fourier transforms $\left(f(\omega) \equiv \int_{-\infty}^{\infty} \mathrm{d}t e^{i\omega t/\hbar} f(t)\right)$

$$\begin{aligned}
G_0^<(k\sigma,\omega) &= 2\pi i\langle n_{k\sigma}\rangle \delta(\omega-\xi_k), && \text{(A.9a)}\\
G_0^>(k\sigma,\omega) &= 2\pi i\{\langle n_{k\sigma}\rangle - 1\}\delta(\omega-\xi_k), && \text{(A.9b)}\\
G_0^r(k\sigma,\omega) &= \frac{1}{\omega-\xi_k+i\eta}, \qquad \eta = 0^+ && \text{(A.9c)}\\
G_0^a(k\sigma,\omega) &= \frac{1}{\omega-\xi_k-i\eta}, \qquad \eta = 0^+. && \text{(A.9d)}
\end{aligned}$$

If we consider the particles to be in thermal equilibrium we find the Fermi-Dirac distribution function

$$\begin{aligned}
\langle n_{k\sigma}\rangle = n_F(\xi_k) &\equiv \mathrm{Tr}[\rho n_{k\sigma}] = \frac{\mathrm{Tr}[e^{\beta H_0} n_{k\sigma}]}{\mathrm{Tr}[e^{\beta H_0}]} \\
&= \frac{\sum_{n_{k\sigma}=0,1} n_{k\sigma} e^{-\beta\xi_k n_{k\sigma}}}{\sum_{n_{k\sigma}=0,1} e^{-\beta\xi_k n_{k\sigma}}} = \frac{1}{e^{\beta\xi_k}+1}, && \text{(A.10)}
\end{aligned}$$

where $\beta \equiv (k_B T)^{-1}$. The fermion spectral function $A_0(k\sigma,\omega)$ is defined as

$$\begin{aligned}
A_0(k\sigma,\omega) &= i[G_0^r(k\sigma,\omega) - G_0^a(k\sigma,\omega)] \\
&= -2\Im\mathrm{m}[G_0^r(k\sigma,\omega)] \\
&= 2\pi\delta(\omega-\xi_k), && \text{(A.11)}
\end{aligned}$$

where the following relation was used

$$\frac{1}{x - i\eta} \;=\; \mathscr{P}\frac{1}{x} - i\pi\delta(x), \qquad \eta = 0^+. \tag{A.12}$$

The spectral function is seen to fulfill the sum rule

$$\int_{-\infty}^{\infty} \frac{\mathrm{d}\omega}{2\pi} A_0(k\sigma, \omega) \;=\; 1. \tag{A.13}$$

Notice the relations valid in equilibrium

$$G_0^<(k\sigma, \omega) \;=\; i n_F(\omega) A_0(k\sigma, \omega), \tag{A.14a}$$

$$G_0^>(k\sigma, \omega) \;=\; i\{n_F(\omega) - 1\} A_0(k\sigma, \omega), \tag{A.14b}$$

A.2 Bosons

The Hamiltonian for free (noninteracting) bosons is

$$H_0 \;=\; \sum_\lambda \Omega_\lambda \Big(b_\lambda^\dagger b_\lambda + \frac{1}{2} \Big), \tag{A.15}$$

where Ω_λ is the energy of mode λ and b_λ ($b_\lambda^\dagger$) is the corresponding boson annihilation (creation) operator. The time-evolution of the annihilation operator in the Heisenberg picture is

$$b_\lambda(t) \;\equiv\; e^{iH_0 t/\hbar} b_\lambda e^{-iH_0 t/\hbar}, \tag{A.16}$$

so the operator obeys the equation

$$\begin{aligned} i\hbar \frac{\partial}{\partial t} b_\lambda(t) \;&=\; [b_\lambda, H_0](t) \\ &=\; \sum_{\lambda'} \Omega_{\lambda'} [b_\lambda, b_{\lambda'}^\dagger b_{\lambda'}](t) = \Omega_\lambda b_\lambda(t), \end{aligned} \tag{A.17}$$

where we have used the relation

$$[A, BC] \;=\; B[A, C] + [A, B]C, \tag{A.18}$$

and the usual boson commutation relations

$$[b_\lambda, b_{\lambda'}] = [b_\lambda^\dagger, b_{\lambda'}^\dagger] = 0, \tag{A.19a}$$

$$[b_\lambda, b_{\lambda'}^\dagger] = \delta_{\lambda,\lambda'}. \tag{A.19b}$$

Eq. (A.17) has the simple solution

$$b_\lambda(t) \;=\; e^{-i\Omega_\lambda t/\hbar} b_\lambda. \tag{A.20}$$

The boson creation operator $b_\lambda^\dagger$ is just the hermitian conjugate of b_λ, i.e.

$$b_\lambda^\dagger(t) \;=\; e^{i\Omega_\lambda t/\hbar} b_\lambda^\dagger. \tag{A.21}$$

The boson real-time single-particle Green's functions are now simply given as

$$\begin{aligned}
D_0^<(\lambda t, \lambda' t') &\equiv -i\hbar^{-1}\langle [b_{\lambda'}^\dagger + b_{\lambda'}](t')[b_\lambda^\dagger + b_\lambda](t)\rangle_0 && \text{(A.22a)}\\
&= -i\hbar^{-1}\left(\langle b_{\lambda'}^\dagger(t')b_\lambda(t)\rangle_0 + \langle b_{\lambda'}(t')b_\lambda^\dagger(t)\rangle_0\right)\\
&= -i\hbar^{-1}\left(e^{i(\Omega_{\lambda'}t'-\Omega_\lambda t)/\hbar}\langle b_{\lambda'}^\dagger b_\lambda\rangle_0 + e^{-i(\Omega_{\lambda'}t'-\Omega_\lambda t)/\hbar}\langle b_{\lambda'} b_\lambda^\dagger\rangle_0\right)\\
&= -i\hbar^{-1}\left(e^{-i\Omega_\lambda(t-t')/\hbar}\langle n_\lambda\rangle_0 + e^{i\Omega_\lambda(t-t')/\hbar}[\langle n_\lambda\rangle_0 + 1]\right)\delta_{\lambda,\lambda'},\\
D_0^>(\lambda t, \lambda' t') &= D_0^<(\lambda' t', \lambda t), && \text{(A.22b)}\\
D_0^r(\lambda t, \lambda' t') &\equiv -i\hbar^{-1}\theta(t-t')\left\langle\Big[[b_\lambda^\dagger + b_\lambda](t), [b_{\lambda'}^\dagger + b_{\lambda'}](t')\Big]\right\rangle_0 && \text{(A.22c)}\\
&= -i\hbar^{-1}\theta(t-t')\left(\langle [b_\lambda^\dagger(t), b_{\lambda'}(t')]\rangle_0 + \langle [b_\lambda(t), b_{\lambda'}^\dagger(t')]\rangle_0\right)\\
&= -i\hbar^{-1}\theta(t-t')\left(-e^{i\Omega_\lambda(t-t')/\hbar} + e^{-i\Omega_\lambda(t-t')/\hbar}\right)\delta_{\lambda,\lambda'},\\
D_0^a(\lambda t, \lambda' t') &= i\hbar^{-1}\theta(t'-t)\left\langle\Big[[b_\lambda^\dagger + b_\lambda](t), [b_{\lambda'}^\dagger + b_{\lambda'}](t')\Big]\right\rangle_0 && \text{(A.22d)}\\
&= i\hbar^{-1}\theta(t'-t)\left(-e^{i\Omega_\lambda(t-t')/\hbar} + e^{-i\Omega_\lambda(t-t')/\hbar}\right)\delta_{\lambda,\lambda'},
\end{aligned}$$

where $n_\lambda \equiv b_\lambda^\dagger b_\lambda$. The Green's functions have the Fourier transforms

$$\begin{aligned}
D_0^<(\lambda, \omega) &= -2\pi i\left\{\langle n_\lambda\rangle\delta(\omega - \Omega_\lambda) + (\langle n_\lambda\rangle + 1)\delta(\omega + \Omega_\lambda)\right\}, && \text{(A.23a)}\\
D_0^>(\lambda, \omega) &= -2\pi i\left\{\langle n_\lambda\rangle\delta(\omega + \Omega_\lambda) + (\langle n_\lambda\rangle + 1)\delta(\omega - \Omega_\lambda)\right\}, && \text{(A.23b)}\\
D_0^r(\lambda, \omega) &= \frac{1}{\omega - \Omega_\lambda + i\eta} - \frac{1}{\omega + \Omega_\lambda + i\eta}, \qquad \eta = 0^+ && \text{(A.23c)}\\
D_0^a(\lambda, \omega) &= \frac{1}{\omega - \Omega_\lambda - i\eta} - \frac{1}{\omega + \Omega_\lambda - i\eta}, \qquad \eta = 0^+. && \text{(A.23d)}
\end{aligned}$$

If we consider the particles to be in thermal equilibrium we find the Bose-Einstein distribution function

$$\begin{aligned}
\langle n_\lambda\rangle = n_B(\Omega_\lambda) &\equiv \mathrm{Tr}[\rho n_\lambda] = \frac{\mathrm{Tr}[e^{\beta H_0}\ n_\lambda]}{\mathrm{Tr}[e^{\beta H_0}]}\\
&= \frac{\sum_{n_\lambda=0}^\infty n_\lambda e^{-\beta\Omega_\lambda n_\lambda}}{\sum_{n_\lambda=0}^\infty e^{-\beta\Omega_\lambda n_\lambda}} = \frac{\sum_{n_\lambda=0}^\infty n_\lambda X^{n_\lambda}}{\sum_{n_\lambda=0}^\infty X^{n_\lambda}}\\
&= \frac{X\sum_{n_\lambda=0}^\infty n_\lambda X^{n_\lambda-1}}{\sum_{n_\lambda=0}^\infty X^{n_\lambda}} = \frac{X\frac{\mathrm{d}}{\mathrm{d}X}\sum_{n_\lambda=0}^\infty X^{n_\lambda}}{\sum_{n_\lambda=0}^\infty X^{n_\lambda}}\\
&= \frac{X\frac{\mathrm{d}}{\mathrm{d}X}\frac{1}{1-X}}{\frac{1}{1-X}} = \frac{X}{1-X}\\
&= \frac{1}{e^{\beta\Omega_\lambda} - 1}, && \text{(A.24)}
\end{aligned}$$

where $X \equiv e^{-\beta\Omega_\lambda} < 1$ ensures the geometric series is converging. The boson spectral function $B_0(\lambda,\omega)$ is similar to the fermion case

$$\begin{aligned} B_0(\lambda,\omega) &= i[D_0^r(\lambda,\omega) - D_0^a(\lambda,\omega)] \\ &= -2\Im\mathrm{m}[D_0^r(\lambda,\omega)] \\ &= 2\pi\delta(\omega-\Omega_\lambda) - 2\pi\delta(\omega+\Omega_\lambda), \end{aligned} \tag{A.25}$$

fulfilling the sum rule

$$\int_{-\infty}^{\infty} \frac{\mathrm{d}\omega}{2\pi} B_0(\lambda,\omega) = 0. \tag{A.26}$$

Notice the relations valid in equilibrium

$$D_0^<(k\sigma,\omega) = -in_B(\omega)B_0(k\sigma,\omega), \tag{A.27a}$$

$$D_0^>(k\sigma,\omega) = -i\{n_B(\omega)+1\}B_0(k\sigma,\omega), \tag{A.27b}$$

which are easily seen to be correct realizing that

$$n_B(\omega) + 1 = n_B(-\omega). \tag{A.28}$$

Appendix B

Hilbert transform

The purpose of this appendix is to derive a way to calculate the Hilbert transform of a function $f(x)$ sampled by a finite number of points on an equidistant grid utilizing the fast Fourier transform (FFT) algorithm. The numerical methods applied here are well described by Press *et al.* in *Numerical Recipes* [84]; in particular their chapter 13.9 on computing Fourier integrals using FFT is useful.

B.1 Numerical method

The Hilbert transform of a function $f(x)$ is defined as [85]

$$H\{f\}(y) = \frac{1}{\pi}\mathscr{P}\int_{-\infty}^{\infty} \mathrm{d}x \frac{f(x)}{x-y}, \tag{B.1}$$

where $\mathscr{P}$ denotes the Cauchy principal value integral. The first observation is that the Hilbert transform of $f(x)$ is basically a convolution with the function $g(x) = -1/x$. One may therefore consider to make use of the *convolution theorem* which states that the convolution of two functions is equal to the product of their individual Fourier transforms.

A similar theorem also holds for the discrete convolution of two lists where the computation can be done in a very fast way with FFT: First one finds the discrete Fourier transform of each list, then the transforms are multiplied element by element, and finally one computes the inverse discrete transform to yield the convolved list.

Now, say we know $f_i = f(x_i)$ on the equidistant grid $x_i = x_0 + i \cdot \Delta$ (i.e. with grid point separation Δ) one might be tempted to do the Hilbert transform by sampling $g(x)$ on x_i as well and appeal to a discrete convolution. But, as pointed out by Press *et al.* [84], special care must be taken when one wants to approximate Fourier integrals of continuous functions by discrete Fourier transforms. Based upon their ideas we therefore consider a more sophisticated method based on linear interpolation.

Let us approximate the function $f(x)$ by a linear interpolation $f_I(x)$ in the following way

$$f(x) \approx f_I(x) \equiv \sum_{i=1}^{N} f_i \psi\left(\frac{x-x_i}{\Delta}\right), \tag{B.2}$$

where $\psi(s)$ is the kernel function associated with linear interpolation,

$$\psi(s) \equiv (1-|s|)\theta(1-|s|). \tag{B.3}$$

The generic kernel function $\psi(s)$ is shown in Fig. B.1. Inserting the interpolated function into Eq. (B.1) we can express the Hilbert transform of $f_I(x)$ on the same discrete grid $x_j = x_0 + j \cdot \Delta$ as

$$H\{f\}(x_j) = H_j \approx \frac{1}{\pi}\mathscr{P}\int_{-\infty}^{\infty} \mathrm{d}x \sum_{i=1}^{N} \psi\left(\frac{x-x_i}{\Delta}\right)\frac{f_i}{x-x_j} = \sum_{i=1}^{N} k_{j-i} f_i, \tag{B.4}$$

where we have identified a transformation kernel

$$\begin{aligned} k_m &\equiv \frac{1}{\pi}\mathscr{P}\int_{-\infty}^{\infty} \mathrm{d}s \frac{\psi(s)}{s-m} \\ &= \frac{1}{\pi}\mathscr{P}\int_{-1}^{0} \mathrm{d}s \frac{1+s}{s-m} + \frac{1}{\pi}\mathscr{P}\int_{0}^{1} \mathrm{d}s \frac{1-s}{s-m} \\ &= \frac{1}{\pi}\big[-(m-1)\ln(m-1) + 2m\ln m - (m+1)\ln(m+1)\big]. \end{aligned} \tag{B.5}$$

In evaluating the integrals leading to Eq. (B.5) we used $m \in \mathbb{Z}$, i.e. that m is never inside the integration range. From Eq. (B.4) it is now evident how the Hilbert transform can be computed by discrete convolution with FFT.

The interpolated function $f_I(x)$ with kernel $\psi(s)$ as in Eq. (B.2) on a finite grid implicitly assumes that the function falls off to zero at the ends of the grid, i.e. that the function has finite support and is fully represented on the grid. If this is not the case one needs to pay special attention to endpoint corrections.

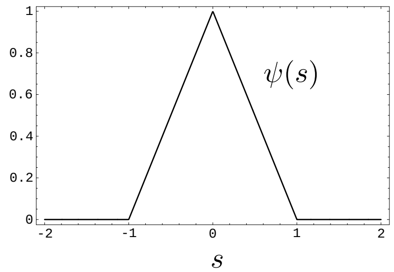

Figure B.1: *Kernel function $\psi(s)$ used for a linear interpolation between equidistant data points.*

B.2 Implementation in Python

The above described trick for computing the Hilbert transform on an equidistant grid has been implemented in the PYTHON programming language [64, 86, 87] as follows:

```
# Hilbert.py BEGIN

import Numeric as N
from math import log
from FFT import fft, inverse_fft

# H[f](y) = 1/\pi p.v._{-\infty}\int^{\infty} dx { f(x)/(x-y) }

def Hilbert(f,ker=None):
    'Hilbert transform'

    def kernel(f):
        'Hilbert transform kernel'
        n = 2*len(f)
        aux = N.zeros(n/2+1,N.Float)
        for i in N.arange(1,n/2+1):
            aux[i] = i*log(i)
        ker = N.zeros(n,N.Float)
        for i in N.arange(1,n/2):
            ker[i] = aux[i+1]-2*aux[i]+aux[i-1]
            ker[n-i] = -ker[i]
        return -fft(ker)/N.pi

    def transform(f,ker):
        'Convolution with kernel'
        n = len(f)
        fpad = fft(N.array((f,N.zeros(n))).flat)
        r = inverse_fft(fpad*ker)
        return r[0:n]

    if ker:
        # A kernel was specified at the function call
        return transform(f,ker), ker
    else:
        ker = kernel(f)
        return transform(f,ker), ker

# Hilbert.py END
```

Appendix C

Semi-infinite one-dimensional tight-binding chain

The semi-infinite one-dimensional tight-binding chain may be used as a simple model for an ideal electrode with finite band-width. Here we want to describe it in terms of Green's functions and find the self-energy that another quantum system acquires if it is coupled to the end of the chain.

The one-dimensional tight-binding chain is described by the Hamiltonian

$$\mathscr{H} \;=\; E\sum_{i=1}^{\infty} c_i^\dagger c_i - t\sum_{i=1}^{\infty}(c_i^\dagger c_{i+1} + \text{h.c.}), \tag{C.1}$$

where E is the on-site energy and t the overlap between neighboring sites. In this real-space basis we can express the retarded Green's function as a semi-infinite matrix

$$\mathbf{G}^r \;=\; \left(\begin{array}{c|ccc} G^r_{11} & G^r_{12} & G^r_{13} & \cdots \\ \hline G^r_{21} & G^r_{22} & G^r_{23} & \cdots \\ G^r_{31} & G^r_{32} & G^r_{33} & \\ \vdots & \vdots & & \ddots \end{array}\right) = \left(\begin{array}{c|ccc} (g^r)^{-1} & t & 0 & \cdots \\ \hline t & (g^r)^{-1} & t & \cdots \\ 0 & t & (g^r)^{-1} & \\ \vdots & \vdots & & \ddots \end{array}\right)^{-1}. \tag{C.2}$$

where $g^r = 1/(\omega - E + i\eta)$ is the free propagator for an isolated site. The structure of the inverse matrix to the right allow us to write [32]

$$\begin{pmatrix} (g^r)^{-1} & t \\ t & (\mathbf{G}^r)^{-1}_{11} \end{pmatrix}\begin{pmatrix} G^r_{11} & G^r_{12} \\ G^r_{21} & G^r_{22} \end{pmatrix} \;=\; \begin{pmatrix} 1 & 0 \\ 0 & 1 \end{pmatrix}, \tag{C.3}$$

which yields the coupled equations

$$(g^r)^{-1}G^r_{11} + tG^r_{21} \;=\; 1, \tag{C.4a}$$

$$tG^r_{11} + (\mathbf{G}^r)^{-1}_{11}G^r_{21} \;=\; 0. \tag{C.4b}$$

Eliminating G^r_{21} we find the solutions

$$G^r_{11} \;=\; \frac{1 \pm \sqrt{1 - 4t^2(g^r)^2}}{2t^2 g^r}. \tag{C.5}$$

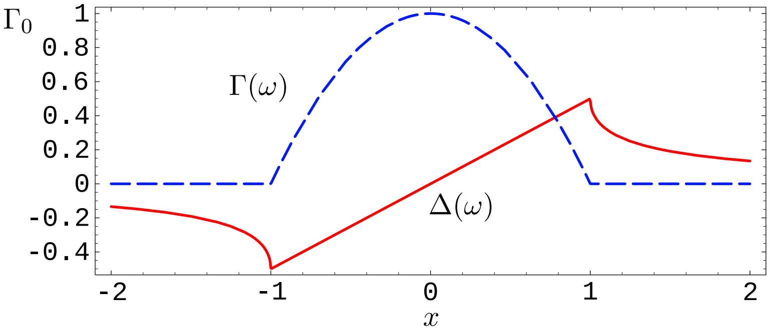

Figure C.1: *Level renormalization* $\Delta(\omega)$ *and escape rate* $\Gamma(\omega)$ *for coupling to a semi-infinite one-dimensional tight-binding chain. The functions are scaled by* $x = (\omega - E)/2|t|$ *and* $\Gamma_0 = 2|V_{1\nu}|^2/|t|$.

In Eq. (C.5) only the "$-$" solution is acceptable since $\lim_{t\to 0} G^r_{11} = g^r$ is required physically. Inserting the expression for g^r we find

$$G^r_{11}(\omega) \;=\; \frac{1}{|t|}\big(x - \mathrm{sgn}(x)\sqrt{x^2-1}\,\big), \tag{C.6}$$

where $x = (\omega - E)/2|t|$. In particular we see that

$$\Re\mathrm{e}G^r_{11}(\omega) \;=\; \frac{1}{|t|} \times \begin{cases} x, & |x| \le 1 \\ \big(x - \mathrm{sgn}(x)\sqrt{x^2-1}\,\big), & |x| > 1 \end{cases} \tag{C.7a}$$

$$\Im\mathrm{m}G^r_{11}(\omega) \;=\; -\frac{1}{|t|}\theta(1-|x|)(1-x^2). \tag{C.7b}$$

Now, if we consider some electronic state $|\nu\rangle$ coupled to the end site of the chain via a tunneling term $V_{1\nu}(c_1^\dagger d_\nu + \mathrm{h.c.})$ its corresponding retarded Green's function $G^r_{\nu\nu}(\omega)$ acquires a self-energy

$$\Sigma^r_{\nu\nu}(\omega) \;=\; V^*_{1\nu}G^r_{11}(\omega)V_{1\nu}, \tag{C.8}$$

which naturally comes about from Dyson's equation. Defining $\Sigma^r_{\nu\nu}(\omega) \equiv \Delta(\omega) - i\Gamma(\omega)/2$ as usual we finally arrive at the following useful expressions

$$\Delta(\omega) \;=\; \frac{\Gamma_0}{2} \times \begin{cases} x, & |x| \le 1 \\ \big(x - \mathrm{sgn}(x)\sqrt{x^2-1}\,\big), & |x| > 1 \end{cases} \tag{C.9a}$$

$$\Gamma(\omega) \;=\; \Gamma_0\theta(1-|x|)(1-x^2), \tag{C.9b}$$

where $\Gamma_0 = 2|V_{1\nu}|^2/|t|$.

Appendix D

Matrix representation of second quantization operators

If one wants to solve a quantum mechanical problem by exact diagonalization one needs to assign matrix representations to the fermion and boson operators involved in the description of the system. In this appendix we device a procedure for constructing such representations in the full Fock-space.

D.1 Single-state basis

A complete basis for the single-state Fock-space $\mathscr{F}_\alpha$ is chosen to be $\{|0\rangle, |\uparrow\rangle \equiv c^\dagger_{\alpha\uparrow}|0\rangle, |\downarrow\rangle \equiv c^\dagger_{\alpha\downarrow}|0\rangle, |\uparrow\downarrow\rangle \equiv c^\dagger_{\alpha\uparrow}c^\dagger_{\alpha\downarrow}|0\rangle\}$, corresponding to the single-particle state being either empty, singly, or double occupied. In this basis the electron creation and annihilation operators can be assigned the following matrix representations [88]

$$\mathbf{c}^\dagger_{\alpha\uparrow} = \begin{pmatrix} 0 & 0 & 0 & 0 \\ 1 & 0 & 0 & 0 \\ 0 & 0 & 0 & 0 \\ 0 & 0 & 1 & 0 \end{pmatrix}, \qquad \mathbf{c}^\dagger_{\alpha\downarrow} = \begin{pmatrix} 0 & 0 & 0 & 0 \\ 0 & 0 & 0 & 0 \\ 1 & 0 & 0 & 0 \\ 0 & -1 & 0 & 0 \end{pmatrix}, \qquad \mathbf{c}_{\alpha\sigma} = [\mathbf{c}^\dagger_{\alpha\sigma}]^T, \tag{D.1}$$

It is easily verified that these operator representations satisfy the usual anticommutation relations for fermion operators

$$\{\mathbf{c}^\dagger_{\alpha\sigma}, \mathbf{c}^\dagger_{\alpha\sigma'}\} = \{\mathbf{c}_{\alpha\sigma}, \mathbf{c}_{\alpha\sigma'}\} = 0, \qquad \{\mathbf{c}_{\alpha\sigma}, \mathbf{c}^\dagger_{\alpha\sigma'}\} = \mathbf{1}_\alpha \delta_{\sigma,\sigma'}, \tag{D.2}$$

where $\mathbf{1}_\alpha$ is the identity matrix. Eq. (D.1) enable us to express operators such as the number operator $n_\alpha = \sum_\sigma c^\dagger_{\alpha\sigma}c_{\alpha\sigma}$ or the single-state Hamiltonian $H_\alpha = \varepsilon_\alpha n_\alpha$ as simple matrix multiplications. Other relevant operators are the spin component S_z and the permutation operator P that will be used later on to secure anticommutation of fermion operators,

$$\mathbf{S}_z = \frac{1}{2}\left(\mathbf{c}^\dagger_{\alpha\uparrow}\mathbf{c}_{\alpha\uparrow} - \mathbf{c}^\dagger_{\alpha\downarrow}\mathbf{c}_{\alpha\downarrow}\right) = \frac{1}{2}\begin{pmatrix} 0 & 0 & 0 & 0 \\ 0 & 1 & 0 & 0 \\ 0 & 0 & -1 & 0 \\ 0 & 0 & 0 & 0 \end{pmatrix}, \tag{D.3}$$

$$\mathbf{P} = \begin{pmatrix} 1 & 0 & 0 & 0 \\ 0 & -1 & 0 & 0 \\ 0 & 0 & -1 & 0 \\ 0 & 0 & 0 & 1 \end{pmatrix}. \tag{D.4}$$

D.2 Two-state basis

We now want to extend the Fock-space with another state β, i.e. $\mathscr{F}_\alpha \to \mathscr{F}_{\alpha\beta} = \mathscr{F}_\alpha \otimes \mathscr{F}_\beta$. A natural basis is $\{|0\rangle, |\uparrow\rangle, |\downarrow\rangle, |\uparrow\downarrow\rangle\}_\alpha \otimes \{|0\rangle, |\uparrow\rangle, |\downarrow\rangle, |\uparrow\downarrow\rangle\}_\beta$, in which the creation operator for state α is simply given as

$$(c^\dagger_{\alpha\sigma})_{\mathscr{F}_{\alpha\beta}} = (c^\dagger_{\alpha\sigma})_{\mathscr{F}_\alpha} \otimes 1_{\mathscr{F}_\beta}. \tag{D.5}$$

Of course the α-operators still anticommute. When it comes to the operators for β special care must be taken in order to preserve anticommutation among both themselves as well as with the α-operators. This is satisfied by defining

$$(c^\dagger_{\beta\sigma})_{\mathscr{F}_{\alpha\beta}} = P_{\mathscr{F}_\alpha} \otimes (c^\dagger_{\beta\sigma})_{\mathscr{F}_\beta}, \tag{D.6}$$

where $(c^\dagger_{\beta\sigma})_{\mathscr{F}_\beta}$ has a representation similar to Eq. (D.1). Other relevant operators are the total number operator N, the total spin component S_z and the permutation operator P

$$\begin{aligned} N_{\mathscr{F}_{\alpha\beta}} &= (n_\alpha)_{\mathscr{F}_\alpha} \otimes 1_{\mathscr{F}_\beta} + 1_{\mathscr{F}_\alpha} \otimes (n_\beta)_{\mathscr{F}_\beta}, && \text{(D.7)} \\ (S_z)_{\mathscr{F}_{\alpha\beta}} &= (S_z)_{\mathscr{F}_\alpha} \otimes 1_{\mathscr{F}_\beta} + 1_{\mathscr{F}_\alpha} \otimes (S_z)_{\mathscr{F}_\beta}, && \text{(D.8)} \\ P_{\mathscr{F}_{\alpha\beta}} &= P_{\mathscr{F}_\alpha} \otimes P_{\mathscr{F}_\beta}. && \text{(D.9)} \end{aligned}$$

D.3 Multiple-state basis

The above sections suggest how to build matrix representations for an arbitrary number of states by adding one state at a time. Thus, the addition of a state ν to Fock-space $\mathscr{F}_{\alpha\beta\ldots\mu}$, thereby generating $\mathscr{F}_{\alpha\beta\ldots\mu\nu} = \mathscr{F}_{\alpha\beta\ldots\mu} \otimes \mathscr{F}_\nu$, implies fermion operators have to be constructed according to

$$\begin{aligned} (c^\dagger_{i\sigma})_{\mathscr{F}_{\alpha\beta\ldots\mu\nu}} &= (c^\dagger_{i\sigma})_{\mathscr{F}_{\alpha\beta\ldots\mu}} \otimes 1_{\mathscr{F}_\nu}, \qquad i \in \{\alpha, \beta, \ldots, \mu\}, && \text{(D.10a)} \\ (c^\dagger_{\nu\sigma})_{\mathscr{F}_{\alpha\beta\ldots\mu\nu}} &= P_{\mathscr{F}_{\alpha\beta\ldots\mu}} \otimes (c^\dagger_{\nu\sigma})_{\mathscr{F}_\nu}, && \text{(D.10b)} \end{aligned}$$

and the other operators according to

$$\begin{aligned} N_{\mathscr{F}_{\alpha\beta\ldots\mu\nu}} &= N_{\mathscr{F}_{\alpha\beta\ldots\mu}} \otimes 1_{\mathscr{F}_\nu} + 1_{\mathscr{F}_{\alpha\beta\ldots\mu}} \otimes N_{\mathscr{F}_\nu}, && \text{(D.11)} \\ (S_z)_{\mathscr{F}_{\alpha\beta\ldots\mu\nu}} &= (S_z)_{\mathscr{F}_{\alpha\beta\ldots\mu}} \otimes 1_{\mathscr{F}_\nu} + 1_{\mathscr{F}_{\alpha\beta\ldots\mu}} \otimes (S_z)_{\mathscr{F}_\nu}, && \text{(D.12)} \\ P_{\mathscr{F}_{\alpha\beta\ldots\mu\nu}} &= P_{\mathscr{F}_{\alpha\beta\ldots\mu}} \otimes P_{\mathscr{F}_\nu}. && \text{(D.13)} \end{aligned}$$

D.4 Bosonic operators

In contrast to a finite fermion Fock-space $\mathscr{F}_{\alpha\beta\ldots\mu\nu}$ caused by the Pauli principle, the Fock-space $\mathscr{B}$ of a single boson state is infinite due to the unbound occupation. A natural basis for $\mathscr{B}$ is $\{|0\rangle, |1\rangle \equiv b^\dagger|0\rangle, |2\rangle \equiv \frac{1}{\sqrt{2}}b^\dagger|1\rangle, \ldots, |n\rangle \equiv \frac{1}{\sqrt{n}}b^\dagger|n-1\rangle, \ldots\}$, in which the boson creation and annihilation operators can be assigned the following matrix representations

$$\mathbf{b}^\dagger = \begin{pmatrix} 0 & 0 & 0 & 0 & \cdots \\ 1 & 0 & 0 & 0 & \\ 0 & \sqrt{2} & 0 & 0 & \\ 0 & 0 & \sqrt{3} & 0 & \\ \vdots & & & & \ddots \end{pmatrix}, \qquad \mathbf{b} = [\mathbf{b}^\dagger]^T = \begin{pmatrix} 0 & 1 & 0 & 0 & \cdots \\ 0 & 0 & \sqrt{2} & 0 & \\ 0 & 0 & 0 & \sqrt{3} & \\ 0 & 0 & 0 & 0 & \\ \vdots & & & & \ddots \end{pmatrix}. \tag{D.14}$$

In the combined Fock-space $\mathscr{F}_{\alpha\beta\ldots\mu\nu} \otimes \mathscr{B}$ we only consider operators F that act in $\mathscr{F}_{\alpha\beta\ldots\mu\nu}$ or operators B that act in $\mathscr{B}$. The extension into the combined space is therefore simply

$$F_{\mathscr{F}_{\alpha\beta\ldots\mu\nu}\otimes\mathscr{B}} = F_{\mathscr{F}_{\alpha\beta\ldots\mu\nu}} \otimes 1_{\mathscr{B}}, \tag{D.15}$$

$$B_{\mathscr{F}_{\alpha\beta\ldots\mu\nu}\otimes\mathscr{B}} = 1_{\mathscr{F}_{\alpha\beta\ldots\mu\nu}} \otimes B_{\mathscr{B}}. \tag{D.16}$$

With the tools above the inclusion of more bosonic operators is straight forward. One just enlarge the Fock-space by suitable outer products.

Bibliography

[1] T. Ito and S. Okazaki, Pushing the limits of lithography, Nature **406**, 1027–1031 (2000).

[2] A. Aviram and M. A. Ratner, Molecular Rectifiers, Chem. Phys. Lett. **29**, 277–283 (1974).

[3] M. A. Reed, C. Zhou, C. J. Muller, T. P. Burgin, and J. M. Tour, Conductance of a Molecular Junction, Science **278**, 252–254 (1997).

[4] M. A. Reed, Molecular-Scale Electronics, in *Proceedings of the IEEE*, volume 87, pages 652–658, 1999.

[5] D. M. Eigler, C. P. Lutz, and W. E. Rudge, An atomic switch realized with the scanning tunneling microscope, Nature **352**, 600–603 (1991).

[6] S. J. Tans, A. R. M. Verschueren, and C. Dekker, Room-temperature transistor based on a single carbon nanotube, Nature **393**, 49–52 (1998).

[7] S. Kubatkin, A. Danilov, M. Hjort, J. Cornil, J.-L. Brédas, N. Stur-Hansen, P. Hedegård, and T. Bjørnholm, Single-electron transistor of a single organic molecule with acces to several redox states, Nature **425**, 698–701 (2003).

[8] W. Ho, Single-molecule chemistry, J. Chem. Phys. **117**(24), 11033–11061 (2002).

[9] J. I. Pascual, N. Lorente, Z. Song, H. Conrad, and H.-P. Rust, Selectivity in vibrationally mediated single-molecule chemistry, Nature **423**, 525–528 (2003).

[10] P. K. Hansma, Inelastic Electron Tunneling, Physics Reports **30**(2), 145–206 (1977).

[11] R. D. Mattuck, *A Guide to Feynman Diagrams in the Many-Body Problem*, Dover Publications, Inc., Mineola, N. Y., 2nd edition, 1992 (Republication of work from 1976).

[12] B. C. Stripe, M. A. Rezaei, and W. Ho, Single-Molecule Vibrational Spectroscopy and Microscopy, Science **280**, 1732–1735 (1998).

[13] J. Tersoff and D. R. Hamann, Theory and Application for the Scanning Tunneling Microscope, Phys. Rev. Lett. **50**, 1998–2001 (1983).

[14] B. N. J. Persson and A. Baratoff, Inelastic Electron Tunneling from a Metal Tip: The Contribution from Resonant Processes, Phys. Rev. Lett. **59**(3), 339–342 (1987).

[15] J. Gaudioso, L. J. Lauhon, and W. Ho, Vibrationally Mediated Negative Differential Resistance in a Single Molecule, Phys. Rev. Lett. **85**, 1918–1921 (2000).

[16] N. Lorente and M. Persson, Theory of Single Molecule Vibrational Spectroscopy and Microscopy, Phys. Rev. Lett. **85**(14), 2997–3000 (2000).

[17] C. Joachim, J. K. Gimzewski, R. R. Schlittler, and C. Chavy, Electronic Transparence of a Single C_{60} Molecule, Phys. Rev. Lett. **74**, 2102–2105 (1995).

[18] J. Morekin and J. W. Ekin, Electron tunneling experiments using Nb-Sn "break" junctions, J. Appl. Phys. **58**, 3888–3895 (1985).

[19] C. J. Muller, J. M. van Ruitenbeek, and L. J. de Jongh, Conductance and Supercurrent Discontinuities in Atomic-Scale Metallic Constrictions of Variable Width, Phys. Rev. Lett. **69**, 140–143 (1992).

[20] H. Park, A. K. L. Lim, A. P. Alivisatos, J. Park, and P. L. McEuen, Formation of metallic electrodes with nanoscale separation by electromigration, Appl. Phys. Lett. **75**, 301–303 (1999).

[21] H. Park, J. Park, A. K. L. Lim, E. H. Anderson, A. P. Alivisatos, and P. L. McEuen, Nanomechanical oscillations in a single-C_{60} transistor, Nature **407**, 57–60 (2000).

[22] S. Braig and K. Flensberg, Vibrational sidebands and dissipative tunneling in molecular transistors, Phys. Rev. B **68**, 205324 (2003).

[23] T. Novotny, A. Donarini, and A.-P. Jauho, Quantum Shuttle in Phase Space, Phys. Rev. Lett. **90**, 256801 (2003).

[24] R. H. M. Smit, Y. Noat, C. Untiedt, N. D. Lang, M. C. van Hemert, and J. M. van Ruitenbeek, Measurement of the conductance of a hydrogen molecule, Nature **419**, 906–909 (2002).

[25] R. H. M. Smit, *From Quantum Point Contacts to Monatomic Chains: Fabrication and Characterization of the Ultimate Nanowire*, PhD thesis, Leiden University, Leiden Institute of Physics, Kammerlingh Onnes Laboratory, 2003.

[26] R. H. M. Smit, C. Untiedt, A. I. Yanson, and J. M. van Ruitenbeek, Common Origin for Surface Reconstruction and the Formation of Chains of Metal Atoms, Phys. Rev. Lett. **87**(26) (2001).

[27] C. Untiedt, A. I. Yanson, R. Grande, G. Rubio-Bollinger, N. Agraït, S. Vieira, and J. M. van Ruitenbeek, Calibration of the length of a chain of single gold atoms, Phys. Rev. B **66**, 085418 (2002).

[28] N. Agraït, C. Untiedt, G. Rubio-Bollinger, and S. Vieira, Onset of Energy Dissipation in Ballistic Atomic Wires, Phys. Rev. Lett. **88**(21), 216803 (2002).

[29] R. H. M. Smit, C. Untiedt, G. Rubio-Bollinger, R. C. Segers, and J. M. van Ruitenbeek, Observation of a Parity Oscillation in the Conductance of Atomic Wires, Phys. Rev. Lett. **91**(7), 076805 (2003).

[30] M. Büttiker, Four-Terminal Phase-Coherent Conductance, Phys. Rev. Lett. **57**(14), 1761–1764 (1986).

[31] A. D. Stone and A. Szafer, What is measured when you measure a resistance? – The Landauer formula revisited, IBM J. Res. Dev. **32**(3), 384–413 (May 1988).

[32] S. Datta, *Electronic Transport in Mesoscopic Systems*, Cambridge University Press, 1995.

[33] M. Brandbyge, J.-L. Mozos, P. Ordejón, J. Taylor, and K. Stokbro, Density-functional method for nonequilibrium electron transport, Phys. Rev. B **65**, 165401 (2002).

[34] J. L. Mozos, P. Ordejón, M. Brandbyge, J. Taylor, and K. Stokbro, Simulations of quantum transport in nanoscale systems: application to atomic gold and silver wires, Nanotechnology **13**, 346–351 (2002).

[35] `http://www.fysik.dtu.dk/CAMP/hot0003.html`, 2004.

[36] M. J. Montgomery, J. Hoekstra, T. N. Todorov, and A. P. Sutton, Inelastic current-voltage spectroscopy of atomic wires, J. Phys.: Condens. Matter **15**(4), 731–742 (2003).

[37] H. Haug and A.-P. Jauho, *Quantum Kinetics in Transport and Optics of Semiconductors*, Springer, 1996.

[38] H. Bruus and K. Flensberg, *Introduction to Quantum Field Theory in Condensed Matter Physics*, Ørsted Laboratory, Niels Bohr Institute, 2001, Lecture notes.

[39] A. Fetter and J. D. Walecka, *Quantum Theory of Many-Particle Systems*, Dover Publications, Inc., Mineola, N. Y., 2003 (Corrected reprint of original work from 1971).

[40] G. D. Mahan, *Many-Particle Physics*, Plenum Press, New York, 2nd edition, 1990.

[41] J. Rammer and H. Smith, Quantum field-theoretical methods in transport theory of metals, Rev. Mod. Phys. **58**(2), 323–359 (1986).

[42] L. V. Keldysh, Diagram technique for nonequilibrium processes, Zh. Eksp. Teor. Fiz. **47**, 1515 (1964).

[43] L. P. Kadanoff and G. Baym, *Quantum Statistical Mechanics*, Frontiers in Physics, W. A. Benjamin, Inc., 1962.

[44] C. Caroli, R. Combescot, P. Nozieres, and D. Saint-James, Direct calculation of the tunneling current, J. Phys. C. **4**, 916–929 (1971).

[45] C. Caroli, R. Combescot, D. Lederer, P. Nozieres, and D. Saint-James, A direct calculation of the tunnelling current: II. Free electron description, J. Phys. C. **4**, 2598–2610 (1971).

[46] C. Caroli, R. Combescot, P. Nozieres, and D. Saint-James, A direct calculation of the tunnelling current: IV. Electron-Phonon interaction effects, J. Phys. C. **5**, 21–42 (1972).

[47] N. S. Wingreen, K. W. Jacobsen, and J. W. Wilkins, Resonant Tunneling with Electron-Phonon Interaction: An Exactly Solvable Model, Phys. Rev. Lett. **61**(12), 1396–1399 (1988).

[48] N. S. Wingreen, K. W. Jacobsen, and J. W. Wilkins, Inelastic scattering in resonant tunneling, Phys. Rev. B **40**(17), 11834–11850 (1989).

[49] S. Hershfield, J. H. Davies, and J. W. Wilkins, Probing the Kondo Resonance by Resonant Tunneling through an Anderson Impurity, Phys. Rev. Lett. **67**(26), 3720–3723 (1991).

[50] S. Hershfield, J. H. Davies, and J. W. Wilkins, Resonant tunneling through an Anderson impurity. I. Current in the symmetric model, Phys. Rev. B **46**(11), 7046–7060 (1992).

[51] J. H. Davies, S. Hershfield, P. Hyldgaard, and J. W. Wilkins, Current and rate equation for resonant tunneling, Phys. Rev. B **47**(8), 4603–4618 (1993).

[52] P. Hyldgaard, S. Hershfield, J. H. Davies, and J. W. Wilkins, Resonant Tunneling with an Electron-Phonon Interaction, Ann. Phys. **236**, 1–42 (1994).

[53] K. Flensberg, Tunneling broadening of vibrational sidebands in molecular transistors, Phys. Rev. B **68**, 205323 (2003).

[54] J.-X. Zhu and A. V. Balatsky, Theory of current and shot-noise spectroscopy in single-molecular quantum dots with a phonon mode, Phys. Rev. B **67**, 165326 (2003).

[55] A. Mitra, I. Aleiner, and A. J. Millis, Phonon effects in molecular transistors: Quantum and classical treatment, cond-mat/0311503 (November 2003).

[56] V. Aji, J. E. Moore, and C. M. Varma, Electronic-vibrational coupling in single-molecule devices, cond-mat/0302222 (March 2003).

[57] Y. Meir and N. S. Wingreen, Landauer Formula for the Current through an Interacting Electron Region, Phys. Rev. Lett. **68**(16), 2512–2515 (1992).

[58] J. W. Negele and H. Orland, *Quantum Many-Particle Systems (Advanced Book Classics)*, Perseus Publishing, 1998.

[59] A.-P. Jauho, Time-dependent transport in interacting mesoscopic systems, cond-mat/9911282 (1999).

[60] A.-P. Jauho, Nonequilibrium Green function modelling of transport in mesoscopic systems, cond-mat/0208577 (2002).

[61] J. Rammer, Master's thesis, University of Copenhagen, Unpublished.

[62] C. A. Stafford, Nonlinear Conductance in Resonant Tunneling, Phys. Rev. Lett. **77**(13), 2770–2773 (1996).

[63] D. S. Fisher and P. A. Lee, Relation between conductivity and transmission matrix, Phys. Rev. B **23**(12), 6851–6854 (1981).

[64] D. M. Beazley, *Python Essential Reference*, New Riders, Indiana, 2nd edition, 2002.

[65] P. Král, Nonequilibrium linked cluster expansion for steady-state quantum transport, Phys. Rev. B **56**(12), 7293–7303 (1997).

[66] T. Stauber, R. Zimmermann, and H. Castella, Electron-phonon interaction in quantum dots: A solvable model, Phys. Rev. B **62**(11), 7336–7343 (2000).

[67] R. Tsu and L. Esaki, Tunneling in a finite superlattice, Appl. Phys. Lett. **22**(11), 562–564 (1973).

[68] T. C. L. G. Sollner, W. D. Goodhue, P. E. Tannenwald, C. D. Parker, and D. D. Peck, Resonant tunneling through quantum wells at frequencies up to 2.5 THz, Appl. Phys. Lett. **43**(6), 588–590 (1983).

[69] V. J. Goldman, D. C. Tsui, and J. E. Cunningham, Evidence for LO-phonon-emission-assisted tunneling in double-barrier heterostructures, Phys. Rev. B **36**(14), 7635–7637 (1987).

[70] N. Agraït, C. Untiedt, G. Rubio-Bollinger, and S. Vieira, Electron transport and phonons in atomic wires, Chem. Phys. **281**, 231–234 (2002).

[71] W. P. Su, J. R. Schrieffer, and A. J. Heeger, Solitons in Polyacetylene, Phys. Rev. Lett. **42**, 1698–1701 (1979).

[72] E. G. Emberly and G. Kirczenow, Landauer theory, inelastic scattering, and electron transport in molecular wires, Phys. Rev. B **61**(8), 5740–5750 (2000).

[73] H. Ness and A. J. Fisher, Quantum Inelastic Conductance through Molecular Wires, Phys. Rev. Lett. **83**(2), 452–455 (1999).

[74] H. Hess, S. A. Shevlin, and A. J. Fisher, Coherent electron-phonon coupling and polaronlike transport in molecular wires, Phys. Rev. B **63**, 125422 (2001).

[75] S. R. Elliot, *The Physics and Chemistry of Solids*, John Wiley & Sons, Inc., 1998 (Reprinted with corrections 2000).

[76] D. Sánchez-Portal, E. Artacho, J. Junquera, P. Ordejón, A. García, and J. M. Soler, Stiff Monatomic Gold Wires with a Spinning Zigzag Geometry, Phys. Rev. Lett. **83**(19), 3884–3887 (1999).

[77] S. R. Bahn, *Computer Simulations of Nanochains*, PhD thesis, Center for Atomic-Scale Materials Physics, Department of Physics, Technical University of Denmark, 2001.

[78] H. Goldstein, *Classical Mechanics*, Addison-Wesley, 2nd edition, 1980.

[79] `http://physics.nist.gov/PhysRefData/contents.html`, 2004.

[80] A. I. Yanson, G. Rubio-Bollinger, H. E. van den Brom, N. Agraït, and J. M. van Ruitenbeek, Formation and manipulation of a metallic wire of single gold atoms, Nature **395**, 783–785 (1998).

[81] R. G. Parr and W. Yang, *Density-Functional Theory of Atoms and Molecules*, International Series of Monographs on Chemistry, Oxford University Press, 1989.

[82] M. C. Payne, M. P. Teter, D. C. Allan, T. A. Arias, and J. D. Joannopoulos, Iterative minimization techniques for *ab initio* total-energy calculations: molecular dynamics and conjugate gradients, Rev. Mod. Phys. **64**(4), 1045–1097 (1992).

[83] DACAPO is developed and maintained by Center for Atomic-Scale Materials Physics (CAMP), Technical University of Denmark.

[84] W. H. Press, S. A. Teukolsky, W. T. Vetterling, and B. P. Flannery, *Numerical Recipes in C: The Art of Scientific Computing*, Cambridge University Press, 2nd. edition, 1992.

[85] J. A. C. Weideman, Computing the Hilbert Transform on the Real Line, Mathematics of Computation **64**(210), 745–762 (1995).

[86] G. van Rossum and F. L. Drake, *Python Tutorial*, Python Software Foundation (available on-line at `www.python.org`), 2003.

[87] D. Ascher, P. F. Dubois, K. Hinsen, J. Hugunin, and T. Oliphant, *Numerical Python – An Open Source Project*, University of California, Lawrence Livermore National Laboratory, 2001.

[88] D. Bohr, DMRG – My implementations. Internal group note, MIC/DTU, October 2003.